INVESTIGATING THE ROLE OF MYOSIN-GENERATED FORCE IN SHAPING CELL MORPHOLOGY

By

Gillian Nicole Fitz

Dissertation

submitted to the Faculty of the

Graduate School of Vanderbilt University

in partial fulfillment of the requirements

for the degree of

DOCTOR OF PHILOSOPHY

in

Cell and Developmental Biology

December 16th, 2023

Nashville, Tennessee

Approved:

Dr. Matthew J. Tyska, Ph.D., Advisor

Dr. Kathleen Gould, Ph.D., Committee Chair

Dr. Dylan Burnette, Ph.D.

Dr. Alissa Weaver, M.D./Ph.D.

Dr. Matthew Lang, Ph.D.

Für Opa.

Es wird schön.

ACKOWLEDGMENTS

First and foremost, I want to convey my deepest gratitude to my mentor, Dr. Matthew Tyska, an exceptional leader and scientist, whose steadfast support and guidance have been pivotal in completing this work and shaping my academic and personal journey. Matt's profound depth of thought, equitable treatment of anyone who walks into his lab, and unwavering trust in each of us has been a continuous source of inspiration for me. His joy of discovery has been nothing short of infectious, and has countless times reignited my scientific enthusiasm. Thank you for having faith in my potential before I did, for allowing me to embrace both my humanity and my role as a scientist, and for creating a lab that nurtures scientific independence; if I could envision an idea, you would ensure I had the resources to test it. It has been under your mentorship that I have gained a sincere sense of humility, confidence, and an unyielding desire to continue to pursue scientific knowledge. I hope that, as a laboratory, we have celebrated your accomplishments as wholeheartedly as you have always celebrated ours.

These thanks extend to the past and present members of the Tyska lab, whom I have had the privilege to work with: Megan, Leslie, Colbie, Rocio, Angelo, Bella, Julissa, Zach, Suli, Kianna, Jen, Olivia, Caroline, Aaron, Deanna and Leah. Thank you for your sharp advice, friendships, and ability to laugh and find humor when science, inevitably, fails. You have not only made the lab an inviting place, but also enriched my life with your friendships. In the ups and downs of graduate school, our environment has been one of support and unity rather than competition. I am so grateful.

To my friends in Nashville, thank you for making Nashville feel like home. Bella, Adri, Ryan and "The Fitness Girls" (Catie, Nora, Emma, and Dillon), I am grateful that our

diverse life paths converged during this period of my life. Thank you for the long bike rides and weekend getaways, and for telling me to stop working to join in on something fun. There are few people in this world with whom we immediately feel a sense of comfort and understanding, and I am so grateful I found those people here. Nora and Emma, your partnership sets the standard for my own, and you make it all look so easy when I know it is not. Your acute self-awareness, keen emotional intelligence, humor, and ability to bring comfort to any situation is commendable. Catie, you were my first friend in graduate school and now you are nothing short of family. Thank you for bringing excitement to long runs and science talks, and for always meeting me at Folk or the Wilburn when we had a bad day. You were my solstice throughout this period in my life, and I truly could not have gotten through this chapter without you. Thank you for inspiring me scientifically and for being my biggest cheerleader, I have the most fun being yours.

To my friends elsewhere, you are my joy and my sanity. The Girks: Nathalie Sun, Dr. Brie Farley, Dr. Hannah Happ, Isabelle Rivers-McCue, Mary Reagan Harvey, Amelia Piazza, Molly Bostrom, Sarah Walz, Dr. Anna Nisi, Cassandra Iroz, and Clara Kappelman. I hope everyone in their life has as fulfilling and meaningful friendships. Thank you for being the epitome of friendship, for showing up and tapping me on the shoulder when I need to course correct. Twelve years of friendship brings both joy and hardship (marriage, death, birth, new pets, relationships beginning and ending, MD/JD/PhD/DVM/MS graduations, promotions, cancer, moves, trips, dance parties and late night to early morning chats and belly aching laughs), and I am fortunate to have had you all by my side. I cherish each one of you so much.

Last, but not least, I have my family to thank. To my extended family (Oma, Hansi, Pezi, Vinz, Annalisa, Toni, Manuel, Eric, Ann, Ned, Katie, Elise, Jarod, Sarah, Ryan, Kai and Michael), thank you for your constant unconditional love and support. Our family is unapologetically welcoming and loud, and I am so lucky to have been born into it. You have given me the gift of love for people and human connection. Papi, Mom, and Perry you are my refuge and my foundation. Papi, you are the reason I am so optimistic and always rather “try to make it at home”. I do not take for granted how hard it must have been to start over in a foreign country later in your life and am so grateful for the opportunities you and Mom have provided us because of it. It is the reason I have the confidence to venture beyond my comfort zone. Ein Fitz geht nicht unter. Mom, thank you for encouraging my academic and musical pursuits, and a love of exploration over things. Thank you for always meeting my dismay with impeccable sass and wit, and for teaching me to trust my gut. Mom and Dad, not everyone is afforded the privilege of pursuing their passions, thank you for creating a life where I am able to do so. Perry, my Mr. Big Ideas, thank you for constantly reminding me to think about the big picture, to stress less and for always being the first to make me laugh. I am lucky I got you as my brother, but even luckier that we have grown into the best of friends. Life is so much better with you, and it is the greatest joy to get to tell people that I am your sister. Our family brings so much love to my life.

TABLE OF CONTENTS

LIST OF TABLES + FIGURES

TABLE PAGE

FIGURE PAGE

LIST OF ABBREVIATIONS

ADP	adenosine diphosphate
ATP	adenosine triphosphate
Arp2/3	actin-related protein 2/3
BSA	bovine serum albumin
C-terminal	carboxy-terminal
CaM	calmodulin
CO_2	carbon dioxide
Cryo-EM	cryogenic electron microscopy
D-loop	Dnase I binding loop
DMSO	dimethyl sulfate
EGFP	enhanced green fluorescent protein
F-actin	filamentous actin
FBS	fetal bovine serum
FERM	4.1 ezrin, radixin, moesin
FL	full-length
FRAP	fluorescent recovery after photobleaching
G-actin	globular actin
HR	hour
IMAC	intermicrovillar adhesion complex
IRES	internal ribosome entry site
KD	knockdown

kDa	kiladaltons
KO	knockout
MyTH4	myosin tail homology 4-band
MaxIP	Maximum intensity projection
N-terminal	amino-terminal
PBS	phosphate buffered saline
PH	pleckstrin homology
PI	phosphatidylinositol
$PI(3,4,5)P_3$	phosphatidylinositol (3,4,5)-triphosphate
PI(3)P	phosphatidylinositol 3-phosphate
PI(4)P	phosphatidylinositol 4-phosphate
$PI(3,4)P_2$	phosphatidylinositol (3,4)-biphosphate
SD	standard deviation
SD	subdomains
SEM	scanning electron microscopy
SH3	SRC homology 3
SIM	structured illumination microscopy
VASP	vasodilator-stimulated protein

CHAPTER I

INTRODUCTION

“Life’s intricacies are best appreciated through the lens of a microscope.”

– Antoni Van Leeuwenhoek

The actomyosin cytoskeleton describes the dynamic network of proteins found in eukaryotes that is comprised of actin filaments and the superfamily of myosin motor proteins. On the micron-scale, these two protein families are primarily responsible for maintaining cell morphology, and on the macro-scale can help stabilize entire tissues. Further, as the actomyosin cytoskeleton is also contractile, it is responsible for the physical principles that govern both cell migration and muscle contraction. Hundreds of years before the discovery of the actomyosin cytoskeleton, early fascinations with the inner workings of muscle contraction date back to the Roman Empire (Galen., 1968). Our current understanding of its structure and function was not grounded until the invention of the microscope in the 17th century. It was then that the power of visual science- to observe and present objects smaller than the human eye can see- was realized. As microscopic resolution improved over the course of the next four centuries, our understanding of the actomyosin cytoskeleton expanded from the conceptual idea that flesh is comprised of “filaments” to resolving individual water molecules within a single actin monomer. This introduction aims to walk through the discovery of the intimately linked superfamily of myosin motors and the actin cytoskeleton, and their vital role in cell morphology.

INITIAL OBSERVATIONS OF CELLULAR FEATURES

During the 2nd century AD, Galen hypothesized that living matter must consist of miniscule fibers while observing the composition of flesh with his naked eye. However, this idea was not conceptualized until the microscope was developed, much later, in the 17th century. With this invention, our understanding of the microscopic world began. When examining cow muscles, the microscope inventor, Antoni van Leeuwenhoek, noted the presence of "small transparent globules" (Leeuwenhoek, 1674), which he later termed 'filaments', when microscopic resolution improved (**Fig 1-1,** left**)**. At a similar time, Robert Hooke, the inventor of the compound microscope, coined the term 'cell' when imaging cork from *Quercus suber,* to describe what we now know to be the basic biological unit of life (**Fig 1-1**, right). Equipped with being able to visualize individual cells, and fascinated by muscle contraction, these two scientists' findings jumpstarted the actomyosin cytoskeleton field. However, at this time, the field diverged into studying either muscle (myosin-centric) or non-muscle (cytoskeleton-centric) cells, and it wasn't until the 20th century that these two fields converged.

THE DISCOVERY OF MYOSIN

With the ability to see beyond what the human eye can see, scientists moved away from imaging samples fresh to preparing them to try to expose the material within the tissue. This approach was pursued by Giorgio Baglivi, who observed vast networks of fibers after boiling and grinding up his samples. This observation led him to propose that the vast fibrous networks he visualized were the basic structural units of all organic

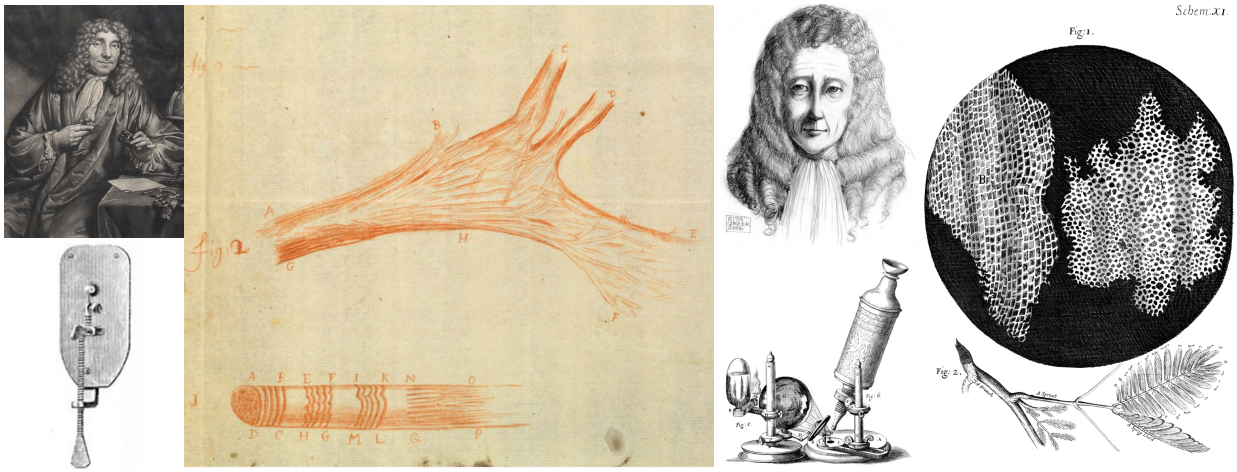

Figure 1-1: 17th century advances in the actomyosin cytoskeleton. Antoni van Leeuwenhoek (Holland, 1632-1723) (left) (© The Royal Society) with his microscope and illustrations of muscle fibers of fish. Robert Hooke (England, 1635-1703) (Wintrebert, 1931) (right) with his compound microscope and illustration of cork (Hooke, 1665) which termed the single, biological unit of life, “cell”.

material- the theory of fibers was born (Baglivi and Pascoli, 1700; Frixione, 2000; Hurst et al., 2002). At the time, this was in direct opposition with the traditional view of the four humors (that the human body is comprised of fluids). In support of the role of solids in organ function, both Jan Swammerdam (1664, 1667) and Dane Niels Stenson (1667) provided more evidence that fluids may not be responsible for muscle contraction. Swammerdam induced muscle contraction in isolated frog muscle by mechanical stimulation and showed that muscle volume did not increase when contracted. This suggested that there is no influx of fluid to cause muscles to contract (Cobb, 2002; Swammerdam, 1679; Swammerdam, 1758) (**Fig 1-2**, left). Additionally, Stenson observed that individual fibers could move independently of one another (Frixione, 2000; Stensen, 1667) further pushing the field into understanding the crucial role of these solids in muscle (**Fig 1-2**, right). Both Baglivi and Stenson observed that these muscle fibers moved towards the middle and shortened, but what caused this remained unknown.

As fluid infusion no longer fit with experimental results, scientists continued to search for the mechanism to explain how muscles fibers slid relative to one another during contraction. By the mid-18th century two conflicting ideas behind muscle contraction emerged. Albrecht von Haller introduced his novel theory of muscle contraction that the simple fibers were connected by a “glutinous muscus”, which was able to pull these fibers together (von Haller, 1732) (1753). However, this idea was rejected by Robert Whytt as the extracted “glutinous muscus” appeared inert, and Whytt hypothesized, instead, that muscle contraction was somehow due to the rings seen in striated muscle. Interestingly, at this point in time, there was enough data to support a sliding filament mechanism (Squire, 2016), an idea that would independently come into full fruition 200 years later.

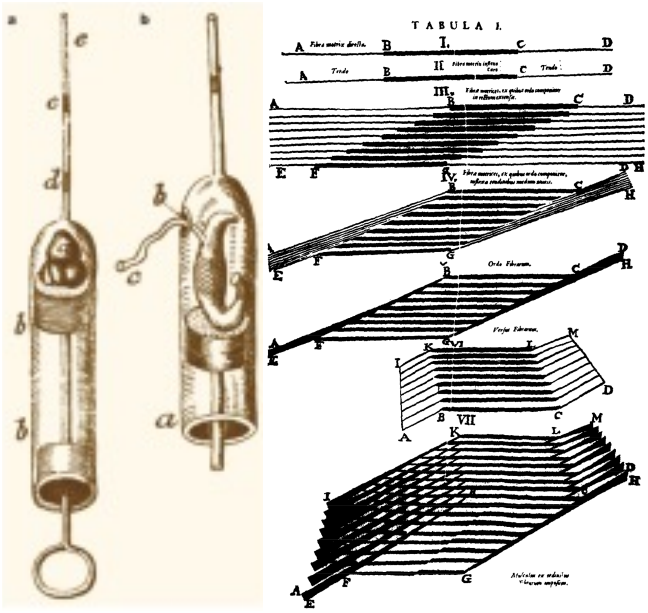

Figure 1-2: 18th century muscle contraction advances. Jan Swammerdam's (Amsterdam, 1637-1680) (left) experimental set up to measure the change in volume upon contraction. Niels Stensen's (Denmark, 1638-1686) (right) illustrations of three-dimensional structures of muscle fibers (Kardel, 1990).

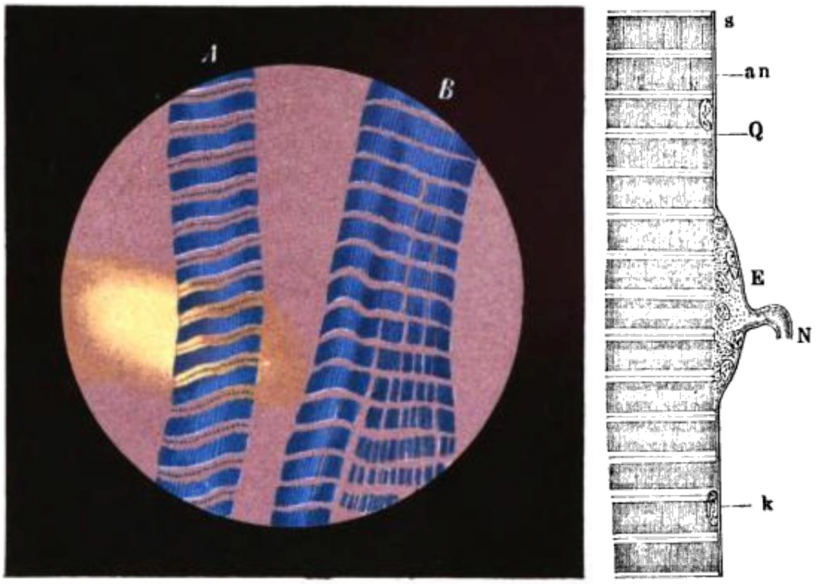

Figure 1-3: 18th century polarized microscopy observations of muscle. Ernst von Brücke's (Germany, 1819-1892) (left) image of muscle fibers from *Hydrophilus piceus* (von Brücke, 1858). Wilhelm Krause's (Germany, 1833-1910) (right) illustration of the dark bands in muscle fibers, which we now know to be the I-band (light band, "Q") and A-band (dark band, "an")(Krause, 1869).

After this Haller-Whytt debate, the introduction of the polarized light microscope continued to place more emphasis on the dark bands on muscle filaments that were now more visible. However, when Ernst von Brücke (**Fig 1-3**, left) (1858) and Krause (**Fig 1-3**, right) (1869) noted that these darker bands maintained a nearly constant size, Haller's idea reemerged that there must be some submicroscopic particle able to slide and contract the muscle filaments together.

This period of uncertainty ended in 1864, when Wilhelm Kühne finally extracted "myosin" (from myo- meaning relating to muscle) from muscle, which he held responsible for keeping a state of tension (Kühne, 1864). However, it would be another ~70 years until we understood the molecular mechanism of muscle contraction, and how myosin and the actin cytoskeleton, the origins of which will be discussed next, were responsible.

THE DISCOVERY OF THE CYTOSKELETON

By the time myosin was identified, the first known images of the cytoskeleton emerged, when Robert Remark, a Polish scientist, illustrated the presence of fine fibrils in the neurons of crayfish (1840s) (**Fig 1-4,** left) (Remak, 1844). While Remark's illustrations were the first to suggest that a cell's interior contained a solid component, in addition to viscous fluid, the idea that these fibrils, now known to be the cytoskeleton, could drive cell morphology wasn't postulated until much later. In 1905, Nikolai Koltsov (Koltzoff) pioneered the idea of a "cell-skeleton" while studying decapod sperm. Koltzoff was specifically interested in understanding why the shape of decapod sperm was so different from other sperm in the animal kingdom, and hypothesized that there must be a

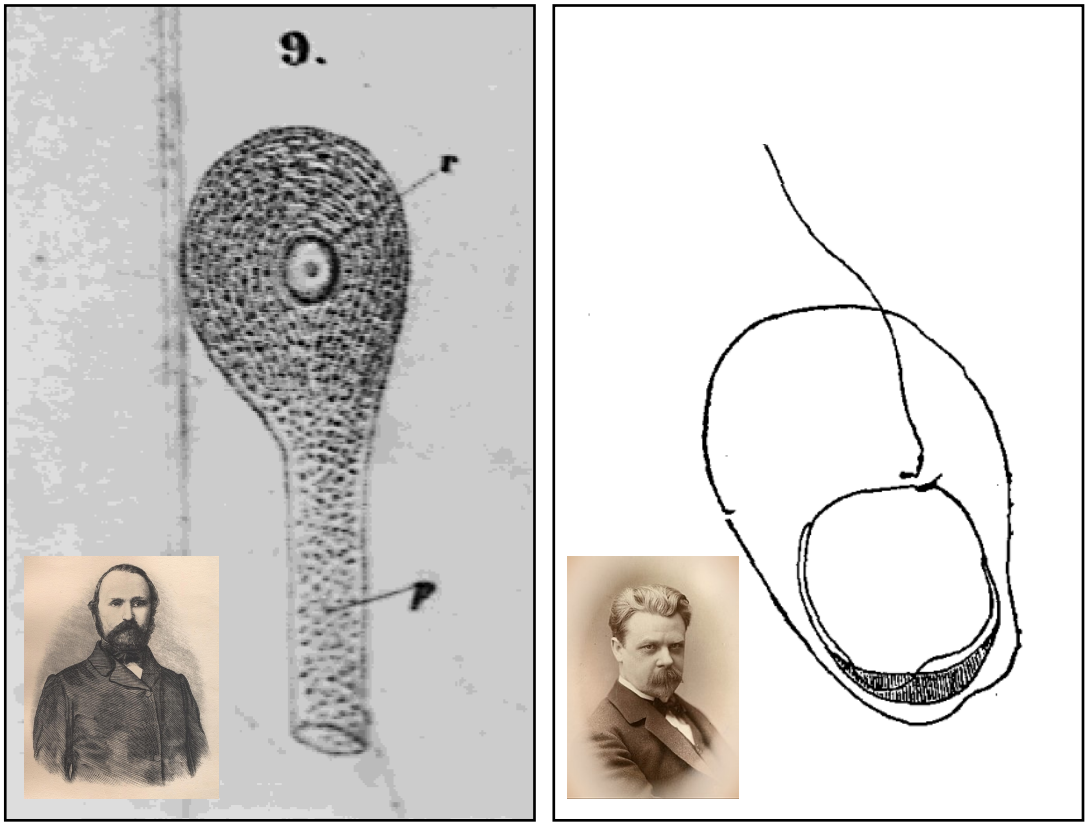

Figure 1-4: 19th and 20th century illustrations of the cytoskeleton. Robert Remark's (Poland, 1815-1865) (left) illustration of the fibrils in the nerve cells of crayfish(Grzybowski and Pietrzak, 2013; Remak, 1844). Nikolai Koltsov's (Russia, 1872-1940) illustration of crayfish sperm (Koltzoff, 1905).

"mechanische Erklarung der ausseren Form der Spermien" [a mechanical explanation of the external form of the sperm] (Koltzoff, 1905) (**Fig 1-4**, right). At a time when the cytoskeleton was barely visible under light microscopy, Koltzoff postulated that a hard protoplasmic skeleton must determine the external form of the cell (Koltzoff, 1924). Further, the idea that a cell's interior consisted of free-flowing granules in a liquid conflicted with the complexities of the time's research findings in a similar way that it conflicted with the studies in muscle cells. By the 1930s, the term "cytosquelette" was coined to describe a cell's physical necessity to maintain its shape and organization (Wintrebert, 1931). This term lingered until the development of the electron microscope, when individual filaments of cilia were finally visualized. It was now that the myosin and actin cytoskeleton fields converged in a laboratory in Hungary.

ACTOMYOSIN CYTOSKELETON IN MUSCLE CONTRACTION

"It is evident… that we need to understand myosin if we want to understand contraction"

– Albert Szent-Györgyi (Banga and Szent-Györgyi, 1942)

A major contributing scientific feat to muscle contraction came in 1929, when Karl Lohmann discovered ATP after isolating it from muscle and liver extract (Lohmann, 1929), and suggested that this was likely the energy source behind muscle contraction (ATP + H_20 → ADP + P_i + H^+ + energy (7.3 kcal/mol)) (Lohmann, 1934). Ten years later, Engelhardt and Lyubimova provided data that myosin had ATPase activity. At the same time, Albert Szent-Györgyi's research group discovered that muscle contraction depends on the interaction between three components: actin, myosin and ATP. Szent-Györgyi's group serendipitously discovered actin when he noticed that the relative viscosity of an

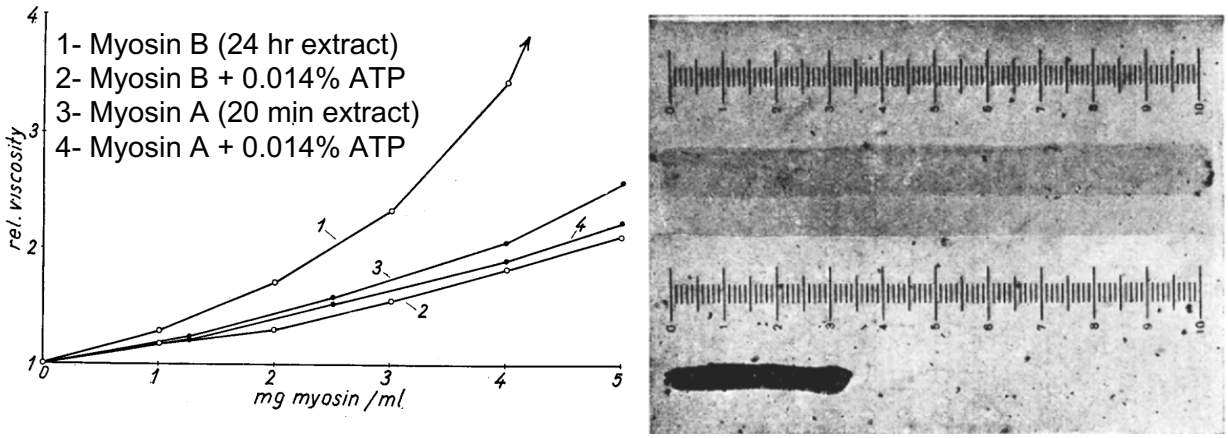

Figure 1-5: Actin, myosin and ATP drive muscle contraction. Szent-Györgyi (Hungary, 1893-1986). contribution to muscle contraction. Viscosity measurements of 24 hr or 20 min myosin actin preps with or without the addition of ATP(Banga and Szent-Györgyi, 1942) (left, adapted). Myosin B (24 hr myosin extract) threads (elongated pieces of myosin gels) treated with water-extract of muscle (bottom) or without (top) demonstrating the contraction of the fiber (Banga and Szent-Györgyi,

extracted myosin prep was much higher after a 24 hr incubation (myosin B) compared to a 20 min (myosin A) incubated myosin prep. Szent-Györgyi also found that the addition of ATP to myosin B could reverse its viscosity whereas the addition of ATP to myosin A had no effect (Banga and Szent-Györgyi, 1942) (**Fig 1-5**, left). Based on these findings, he proposed that myosin B was a combination of myosin A and an additional compound, which he named “actin” as this compound was able to influence the “activity” of myosin (Banga and Szent-Györgyi, 1942). Further, his studies also revealed that the addition of the water-extract from muscle, which we now know to contain ATP, was able to cause extracted muscle fibers to contract (**Fig 1-5**, right). The fascination behind what caused the segment in muscle to contract, first visualized by Leeuwenhoek, could now be replicated in the laboratory. This work put forward the concept of “actomyosin” to describe “a mixture of compound of actin and myosin” (Szent-Györgyi, 1942). The same group later went on to isolate actin, and discovered that it existed in two forms: an inactive, globular actin (G-actin) and an active, fibrous actin (F-actin)(Szent-Györgyi, 1944).

Within two years, Szent-Györgyi’s research group was able to put to rest centuries of uncertainty about what proteins caused muscle contraction. This marked the onset of our deeper understanding of the actomyosin cytoskeleton through the 21st century. A current understanding of actin and myosin will be described, in detail, next.

ACTIN

Actin is a 42 kD protein that exists as a water-soluble monomer, globular (G-actin), which can be polymerized into a filament, filamentous actin (F-actin). Homologs of actin exist across the animal kingdom and its sequence is 95% conserved from yeast to

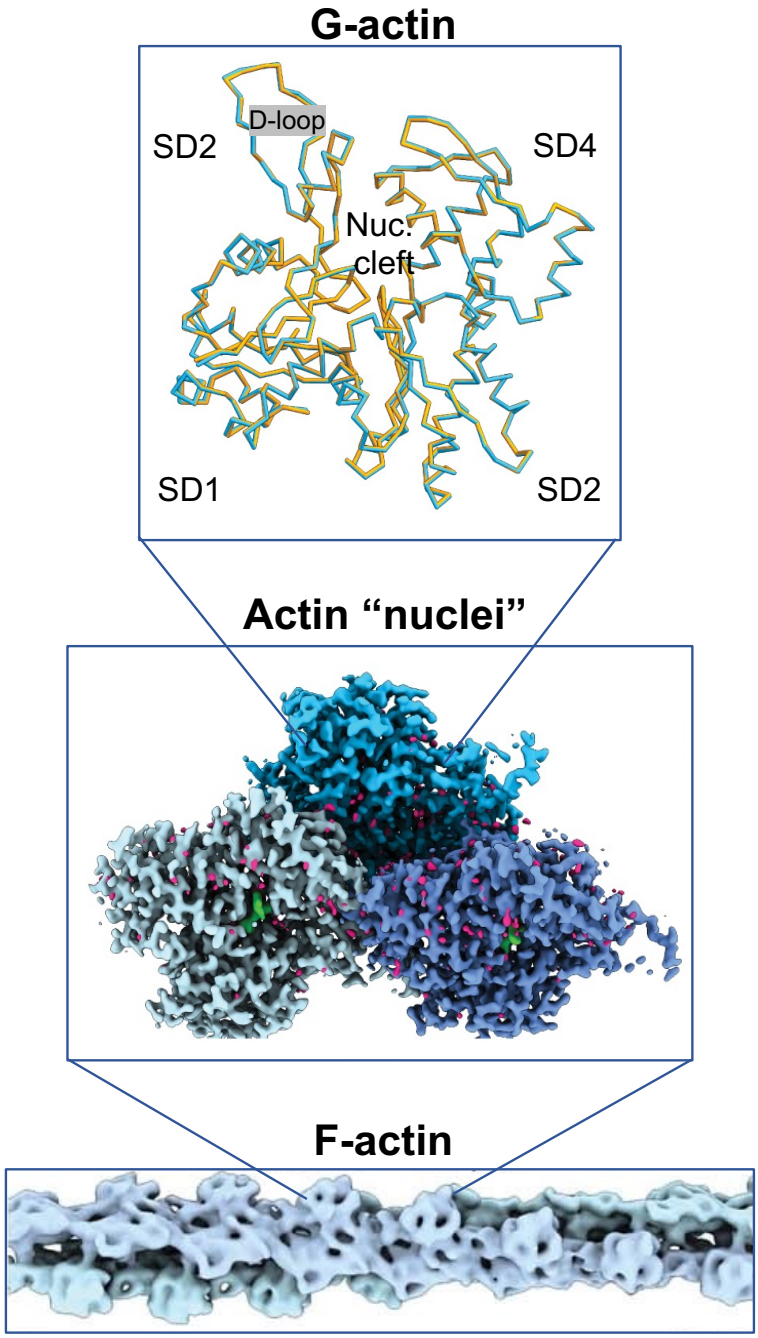

Figure 1-6: Structural conformation of G- and F-actin. From top to bottom: Cα representation of an actin monomer highlighting the four subdomains (SD1, SD2, SD3 and SD3), nucleotide binding cleft (nuc. cleft) and D-loop; Cryo-EM map of three monomers polymerized together under an ADP (green)-bound state (water molecules, magenta); cryoDRGN reconstruction of an ADP-bound F-actin filament; cartoon schematic of the off and on rate of ATP or ADP bound G-actin into F-actin. All images oriented with the pointed end on the left, and barbed end on the right; images from (Reynolds et al., 2022).

humans. In eukaryotic cells, actin accounts for ~10% of the total protein (100-200 μM) and is critical for life(Bunnell et al., 2011; Korn et al., 1987).

A single actin monomer is comprised of four subdomains (SDs), with a larger cleft between SD2 and SD4 for nucleotide binding, and a smaller cleft between SD1 and SD3 which mediates the interaction with actin binding proteins (Dominguez, 2004; Dominguez, 2007) (**Fig 1-6**, top). SD2 also contains the DNase I binding loop (D-loop), which undergoes conformational changes during the ATP to ADP transition. These G-actin monomers then polymerize to form F-actin (**Fig 1-6,** bottom) through a "nuclei" intermediate, a trimer of actin monomers (**Fig 1-6**, middle).

The process of generating F-actin from individual actin monomers is a complex process that involves the formation of an unstable actin trimer, "nuclei", intermediate (dissociation constants in the range of 0.1 to 1M (Pollard and Cooper, 1986)) that serves as a template for the further polymerization into F-actin. Overcoming the rate-limiting step is critical for elongation (lag phase; **Fig 1-7**), and once this step is complete, polymerization occurs primarily from the barbed, or growing, end of F-actin before reaching a steady-state (log phase; **Fig 1-7**). At this point, treadmilling can begin, a process in which new monomers continue to be incorporated into the barbed ends and monomers are removed from the pointed ends (steady-state; **Fig 1-7**).

The polarity of F-actin was originally determined by labeling F-actin with myosin subfragment-1 (S1), revealing an arrowhead like pattern from which the nomenclature of pointed (for the arrowhead point) and barbed end originated (**Fig 1-8,** top) (Hirokawa and Heuser, 1981; Hirokawa et al., 1982). A classic study determined the dissociation (k_{off} (s^{-1}) and association (k_{on} ($\mu M^{-1}s^{-1}$) rate constants of either ATP or ADP bound G-actin

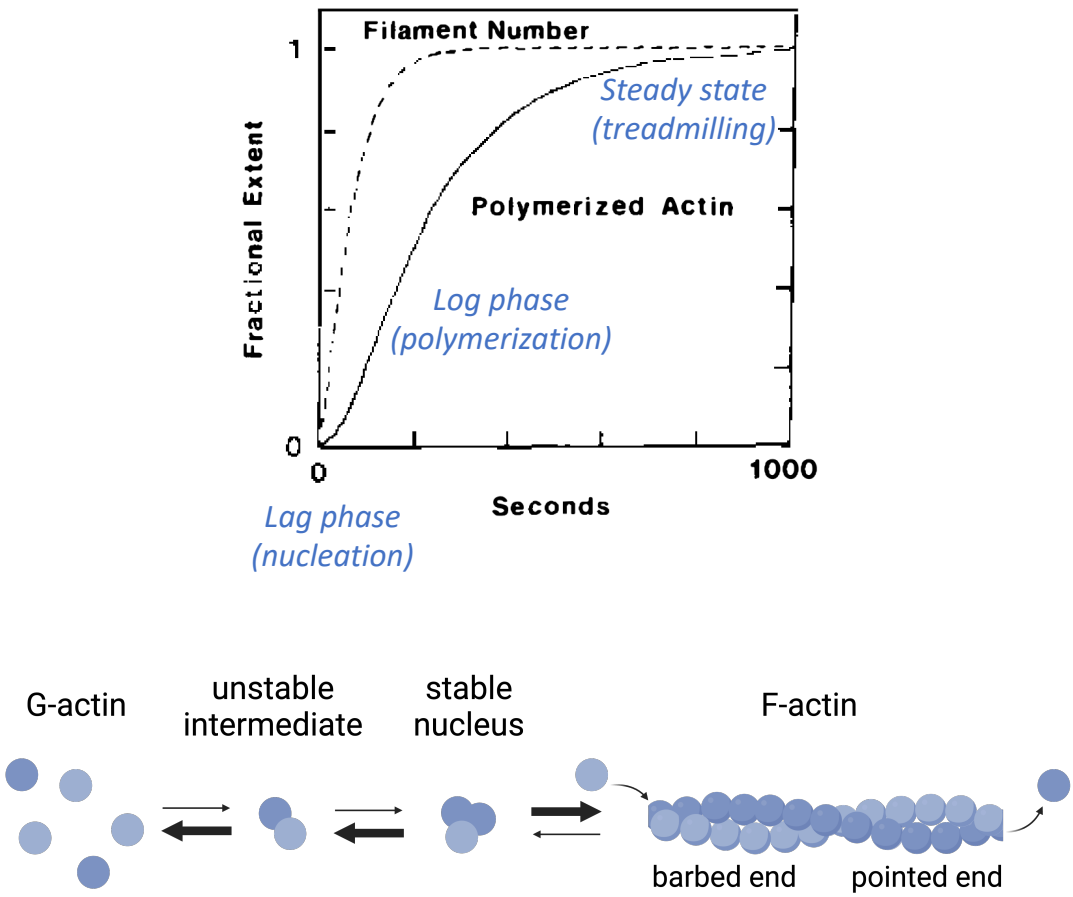

Figure 1-7: Actin polymerization. From top to bottom: Time course of nucleation and polymerization of actin(Pollard and Cooper, 1986) and the nucleation of actin monomers into F-actin. Bottom cartoon schematic demonstrates the unfavorable product that forms prior to the stable nuclei intermediate. Right arrows indicate association rate and left arrows indicate disassociation rates (Adapted from (Pollard, 2016)).

monomers for both the barbed and pointed ends (**Fig 1-8,** bottom) (Pollard, 1986). Using electron microscopy, Pollard estimated the on/off rate constants at both ends by measuring the length of actin filaments grown from *Limulus* acrosomal nuclei at different time points with varying concentrations of actin. From these rate constants, the equilibrium constant (K), also referred to as the "critical concentration", or the concentration of monomer needed for polymerization, can be determined.

From this single filament, dynamic and vast arrays of actin are arranged and rearranged broadly into two types of actin: branched and linear (**Fig 1-9**). Branched actin networks are primarily found at the leading edge of cells and are built via the Arp2/3 complex. Arp2/3 is a seven-domain protein that was first characterized when studying the branched actin, lamellipodium, structure (**Fig 1-9**, middle). Arp2/3 is the only known protein able to nucleate branched actin networks, and after being activating by nucleating promoting factors (NPFs), Arp2/3 generates "daughter" filaments off of "mother" filaments at a ~70° angle (Mullins et al., 1998). This generates the meshwork of actin filaments seen in lamellipodia at the leading edge of migrating cells.

Linear actin networks are made up of mostly parallel bundled F-actin. In eukaryotic cells, the three primary type of actin-based linear networks are the cell surface protrusions: microvilli, stereocilia and filopodia (**Fig 1-9**). Microvilli are ~1 μm cell extensions off the apical surface of the proximal tubule epithelium of the kidney and on the main absorptive cell of the gut, enterocytes. Functionally, in the intestine, microvilli are primarily responsible for nutrient absorption and are the primary physical barrier for pathogen defense (Hirokawa et al., 1982; Mooseker and Tilney, 1975). Stereocilia

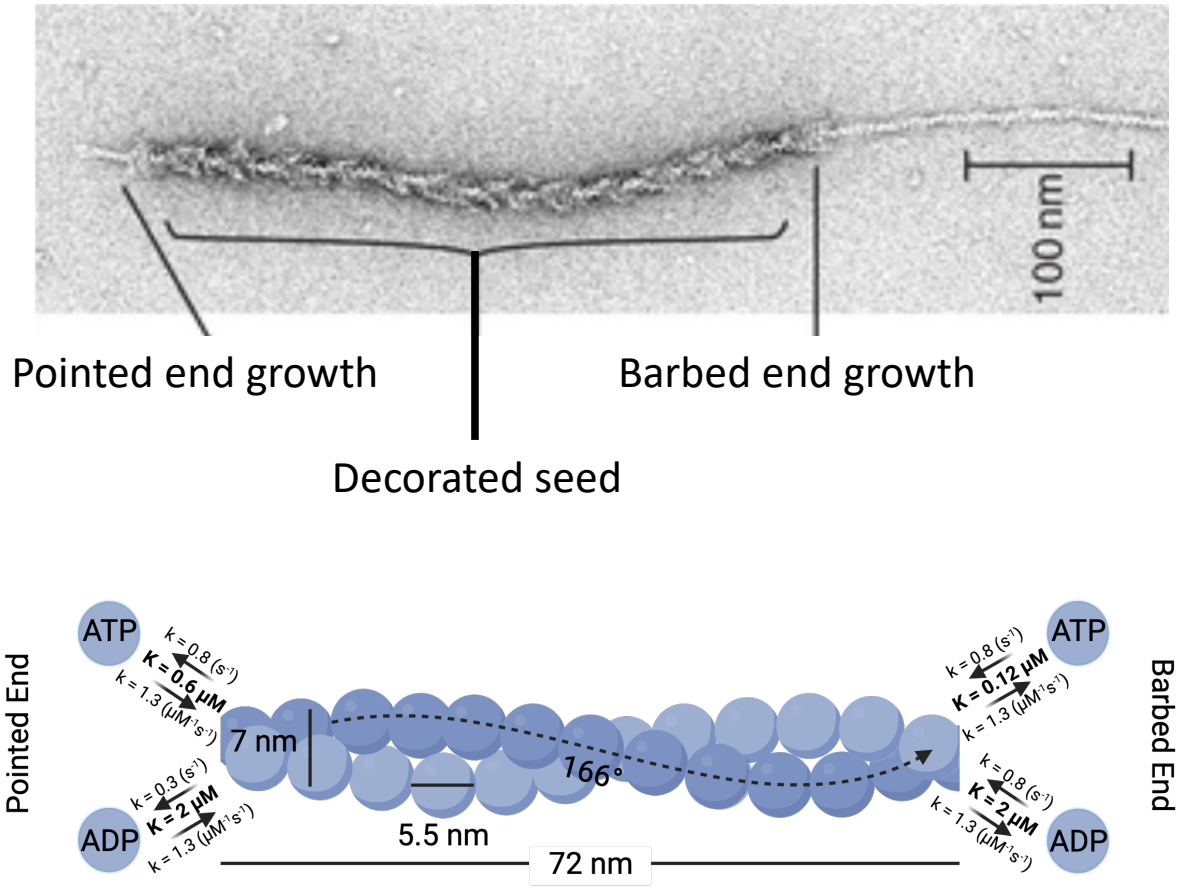

Figure 1-8: Actin polarity and critical concentrations for polymerization. From top to bottom: actin filament decorated with heavy meromyosin (myosin subfragment-1 and its associated light chains) (Adapted from (Woodrum et al., 1975)); cartoon schematic of the off and on rates of ATP or ADP bound monomers with the critical concentrations (Adapted from (Pollard, 2016)).

represent a more exaggerated actin-based protrusion found in the inner ear cells and are responsible for hearing and balance via their ability to mechanically sense external cues (Prost et al., 2007). Filopodia represent a more generalized class of actin-based protrusion found in many motile cells with a much more versatile functionality: at the leading edge of migrating cells they sense external cues (Mattila and Lappalainen, 2008) and can assist in cell-cell adhesion (Millard and Martin, 2008), in neurons have been shown to be important in the development of dendritic spines (Sekino et al., 2007), and are upregulated in many cancers likely assisting enhancing cell invasion (Vignjevic et al., 2007). Interestingly, while myosins were originally characterized in muscle, myosins are also abundant residents in these cellular protrusions, and the details of this force-generating protein will be discussed in detail next.

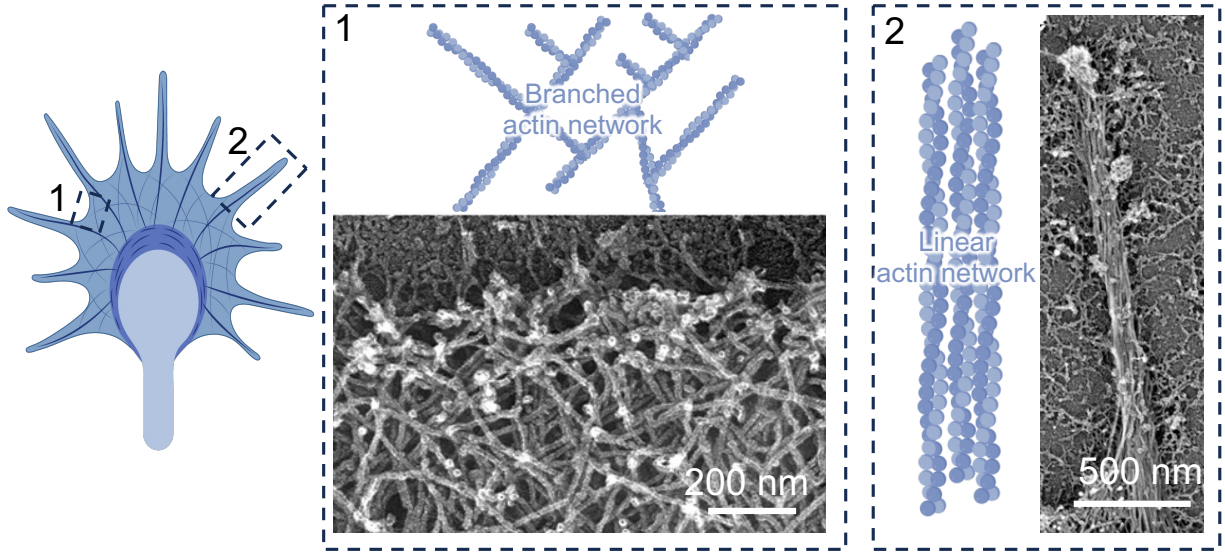

Figure 1-9: Branched and linear actin networks. Cartoon schematic (far left) of a growth cone (the actin-supporting extension of a neurite), highlighting branched (1) and linear (2) actin structures. Platinum replica electron microscopy images highlight the ultrastructure of branched and linear actin arrays. Here, the branched network is a lamellipodium and the linear network a single filopodium. (Adapted from (Alexandrova et al., 2020; Svitkina et al., 1997)).

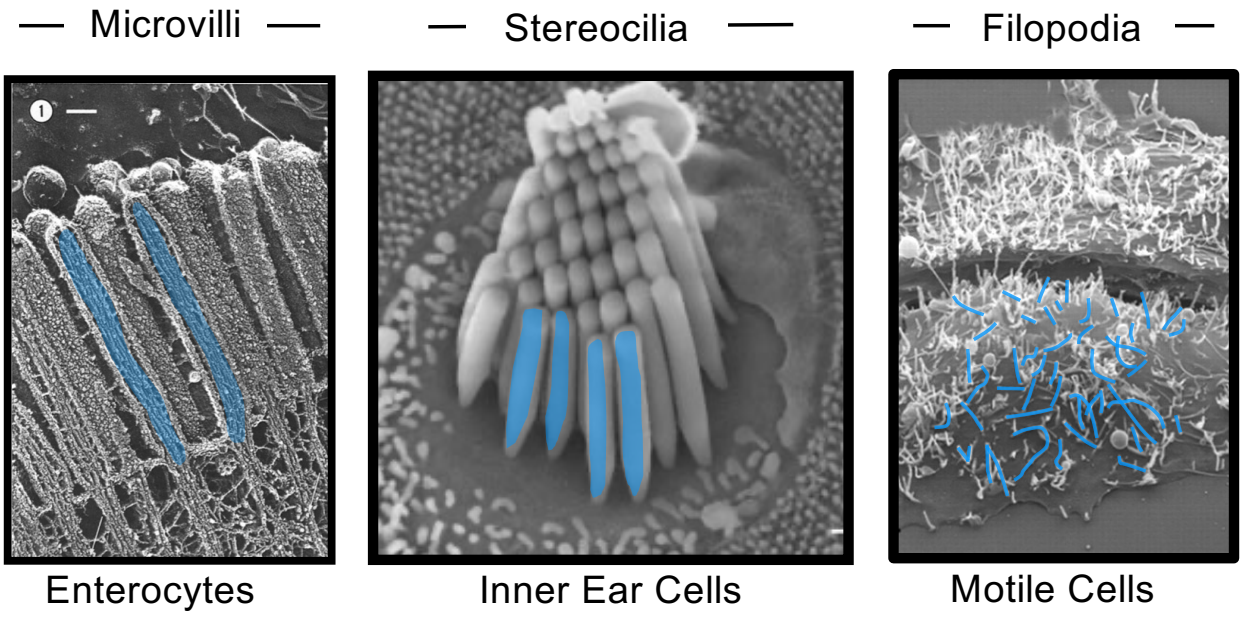

Figure 1-10: Examples of linear actin-based cell surface protrusions. From left to right: microvilli found on the apical surface of enterocytes; stereocilia found on the apical surface of inner ear cells; filopodia found on many types of motile cells. (From (Bohil et al., 2006; Hirokawa et al., 1982)

Parallel bundled actin-based protrusion properties

Protrusion type:	Height:	Width:	# of actin filaments:	Actin bundlers:
Microvilli	~1 μm	90 nm	20-30	Villin, espin, fimbrin, misp
Stereocilia	10-50 μm	250 nm (tip) 100 nm (base)	50-100	Fimbrin, espin, fascin
Filopodia	5-35 μm (up 70 μm)	100 - 300 nm	10-30	Fascin

Table 1-1: Properties of microvilli, stereocilia and filopodia.

MYOSIN

Myosins are found in all tissue types, including in all the aforementioned types of actin-based protrusions. All myosins have three domains: a highly conserved N-terminal motor domain, or head, that binds actin and hydrolyzes ATP, a neck or lever arm region that transduces the force production during the power stroke (Purcell et al., 2002; Sakamoto et al., 2005; Sun and Goldman, 2011; Uyeda et al., 1996; Warshaw et al., 2000), and a unique C-terminal tail (Sellers, 2000) (**Fig 1-11**).

The motor domain (**Fig 1-12**) hydrolyzes ATP leading to conformational changes to produce force (Robert-Paganin et al., 2020). The motor domain is comprised of four subdomains: the upper and lower 50-kDa subdomains, the N-terminal domain, which contains the ATP nucleotide binding pocket, and the converter domain, which transduces force to the neck region. The upper and lower 50-kDa subdomains bind actin and are separated by a large cleft which closes upon ATP or actin binding (Houdusse et al., 1999). The N-terminal domains contains the ATP nucleotide binding pocket, and the converter domain transduces the chemical energy of ATP hydrolysis to mechanical energy to the neck domain. The neck or lever arm domain is made up of IQ motifs [IQXXXRGXXR], which contain multiple basic residues that serve as binding sites for calmodulin (CaM) and calmodulin-like proteins (Cheney and Mooseker, 1992; Homma et al., 2001; Rogers and Strehler, 2001). The C-terminal tails of myosins are the most diverse domains, thereby specifying function, and frequently mediate cargo binding, contain functional motifs, such as SH3, FERM and PH domains, and interact with the membrane (Sellers, 2000).

Since the discovery of skeletal muscle myosin in 1864, 31 myosin subclasses have

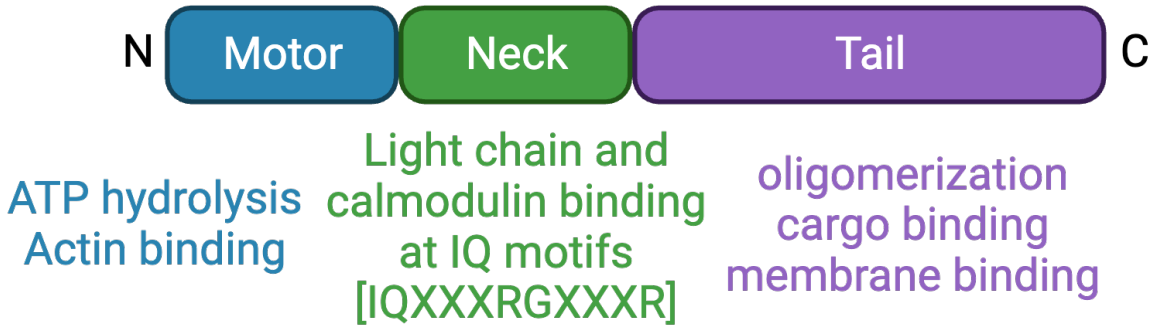

Figure 1-11: Cartoon schematic of the conserved three domain structure myosin. Motor domain (blue), neck domain (green), tail domain (purple).

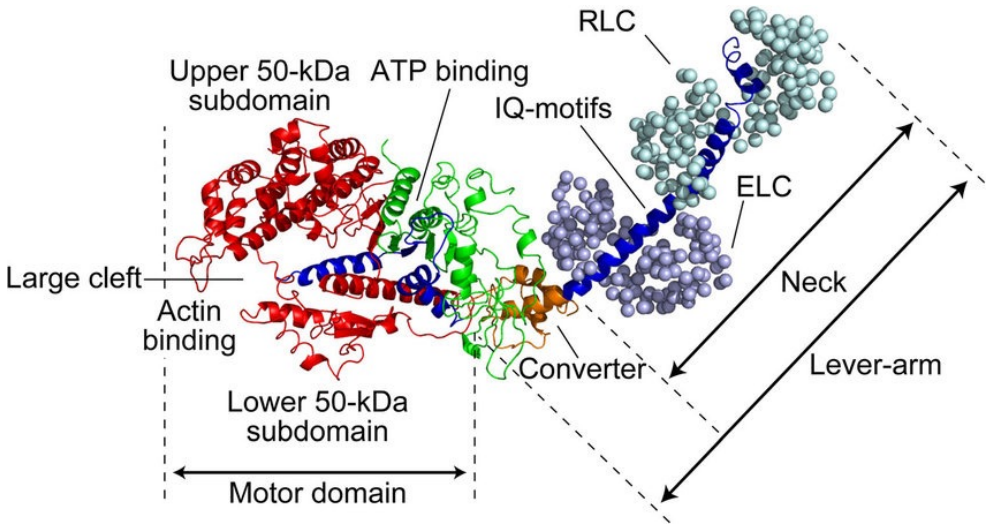

Figure 1-12: Ribbon diagram of the highly conserved motor domain with the neck domain. Motor domain from the skeletal muscle myosin-2 of *Gallus gallus*. and represents the motor domain of myosin-2. Motor domain highlights four main domains: (From (Kodera and Ando, 2014)).

been defined across eukaryotic species (Sebe-Pedros et al., 2014). These 31 subclasses can be divided into two groups: conventional and unconventional (**Fig 1-13**). Conventional myosins represent the class of myosins historically identified in muscle contraction. Generally, these motors organize into dimers which are then further organized into bipolar filaments via their C-terminal tail. Unconventional myosins represent myosins that do not form bipolar filaments and can exist as either a monomer or dimer. Using the chemical energy derived from ATP hydrolysis, myosin generates a pulling force by binding and unbinding actin in an ATP-dependent manner. This process is known as the crossbridge cycle (**Fig 1-14**), a cycle first described by Andrew Huxley in 1957 when characterizing a mechanism for muscle force contraction generation (Huxley, 1957). This model continued to evolve through the 1970s as new evidence emerged describing the strong and weak myosin motor-actin binding states, defining the kinetic mechanism of the actomyosin crossbridge cycle (Lymn and Taylor, 1971). Through this cycle, myosins can exert force on anchored filaments (the conventional myosins in muscle) or move in a processive manner along actin filaments (unconventional myosins). Just as the myosin tail is unique to each myosin, so are the kinetic properties of each myosin. One such kinetic property, intimately tied to the crossbridge cycle, is a myosin's duty ratio, *r*, defined as the fraction of time a myosin motor spends attached to actin (t_{on} / (t_{total})) (O'Connell et al., 2007). Differences in this ratio account for why some motors can process ($r \geq 0.5$) along actin while others cannot. In addition to duty ratio, myosins have a large range of other kinetic properties. These kinetic properties help account for the amount of force myosins are able to generate through the equation $F_{avg} = r*F_{uni}*N$, where the average force is a multiple of the duty ratio (*r*), unitary force (F_{uni}) and the number of motors (N) (VanBuren et al., 1995).

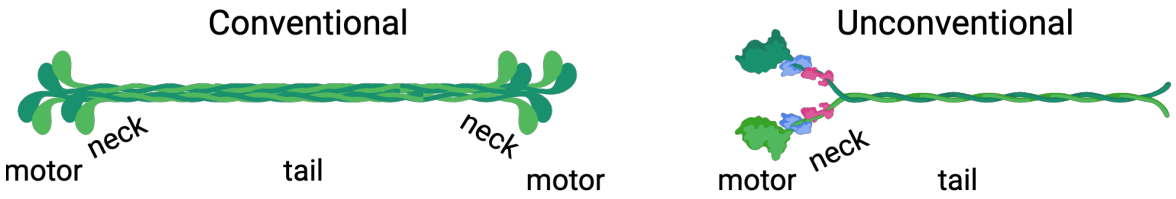

Figure 1-13: Cartoon schematic of the two branches of the myosin super-family. Conventional myosins (left) and unconventional myosins (right).

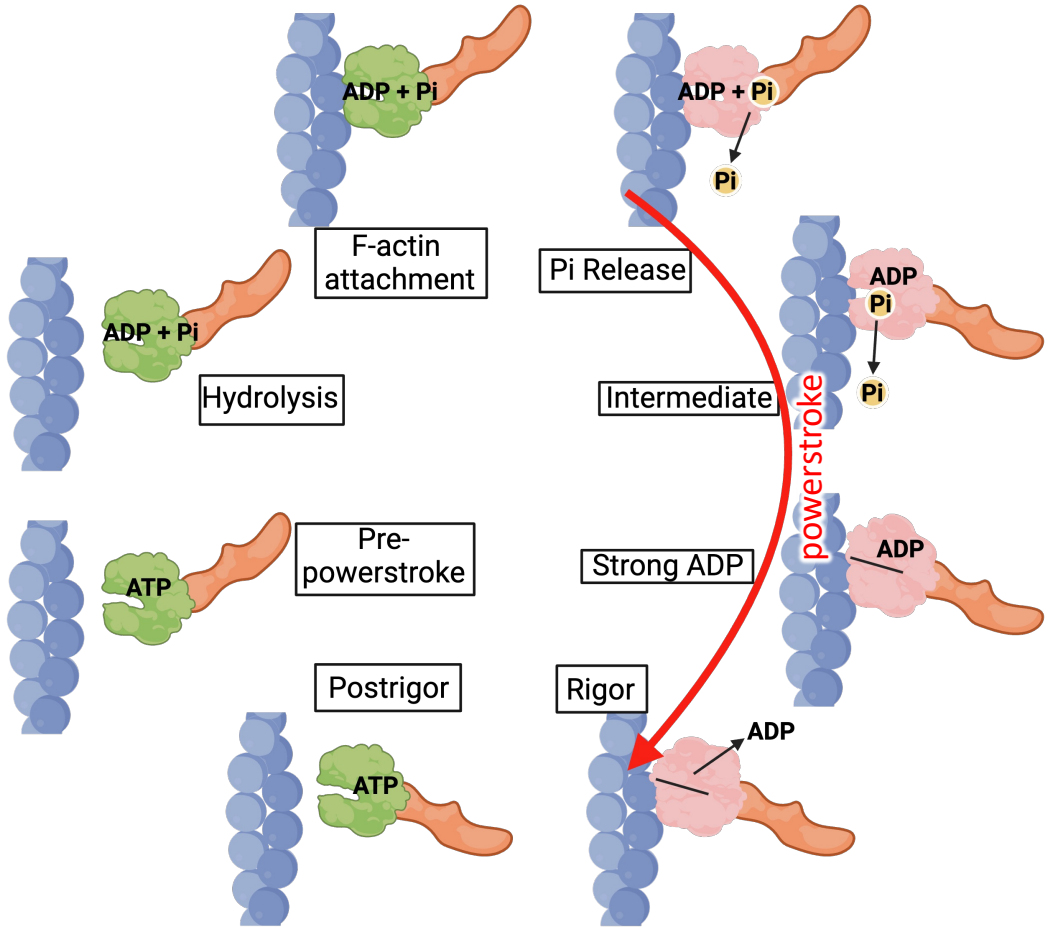

Figure 1-14: Myosin crossbridge cycle. Motor domains and their interaction in either an ATP (green) or ADP (pink) state. Red arrow denotes the powerstroke. Adapted from (Houdusse and Sweeney, 2016).

The diversity of myosins (31 subclasses) and their respective kinetic properties elps account for how specific myosins have adapted for their specific roles in the tissues in which they reside. However, actomyosin cytoskeletal force is not restricted to motor proteins; actin is also able to generate force through the incorporation of actin monomers.

ACTIN FORCE GENERATION

Current theories on how actin filaments generate force are based on the Brownian motion that is inherent to all subcellular components. By applying the Feynman ratchet model to Brownian motion, the Brownian-ratchet model suggests that protrusion elongation is driven by mechanical force. This mechanical force is induced by thermal fluctuations of the ends of growing actin filaments (F-actin) as well as the plasma membrane, if this is acting as the barrier (Peskin et al., 1993; Smoluchowski, 1927). Here, the addition of new G-actin monomers at filament barbed ends (the preferred site for incorporation) prevents the displacement of the membrane, or barrier, back to its original position and gives rise to a pushing force that drives the barrier forward (Theriot, 2000) (**Fig 1-15**). A classic study completed by Footer et al., was the first to determine the amount of force polymerizing actin filaments, with free barbed ends, can generate and determined that individual actin filaments can generate ~1 pN of force (Footer et al., 2007b), with $F_{max} = (k_bT/\delta)\ln(C/C_{crit})$ (k_b = Boltzmann's constant; T = absolute temperature; elongation distance of a single subunit, *C* is the concentration of monomers in solution and *C*crit is the critical concentration). In these studies, Footer et al., used an optical trap to hold a polystyrene bead attached to a filamentous growing acrosomal bundle in place while a microfabricated wall, which served as a rigid barrier, was brought into contact

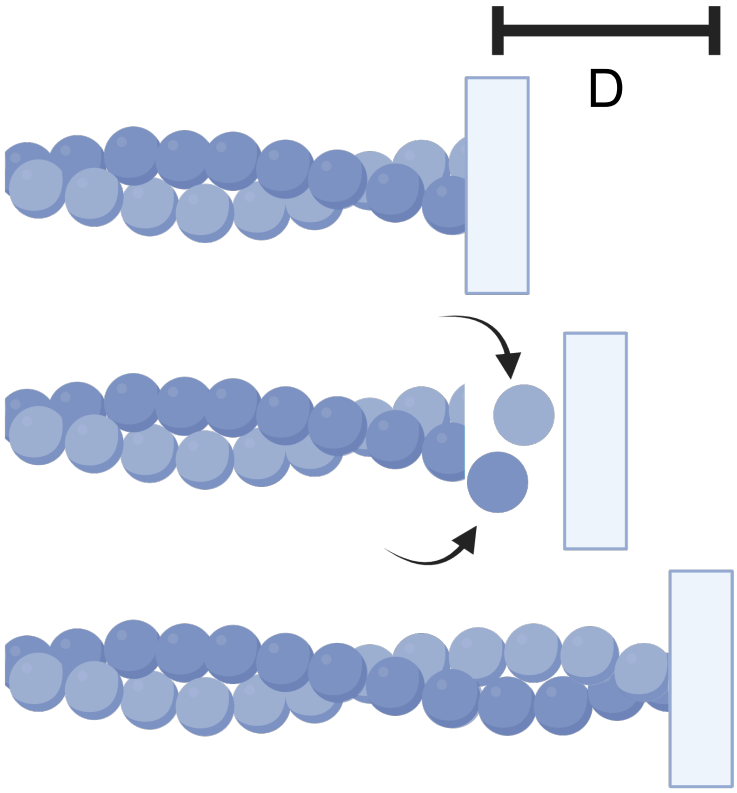

Figure 1-15: Cartoon schematic of the actin polymerization motor. Incorporation of free actin monomers become incorporated at the barbed-end when openings between the barrier and the end of the filament emerge. This pushes the barrier forward. This schematic represents actin when it is anchored at the pointed end. Here, the force is directly proportional to the distance moved (D). Adapted from(Theriot, 2000).

with the end of the filament bundle. In this way, the forces generated from polymerizing actin filaments could be measured as a function of both the length of the bead displacement and trap stiffness.

SUMMARY

While the primary structures of the actomyosin cytoskeleton were first seen by eye in muscle, decades of technological advancements have offered mechanistic insights into the roles of myosin and actin in driving muscle contraction. Decades later, we now associate the actomyosin cytoskeleton with a wide array of functions in cell biology, particularly in cases requiring cell tension or material transport. For example, studies have shown that myosins are localized to most organelles and membrane compartments (Hartman and Spudich, 2012) - the nucleus (Woolner and Bement, 2009), mitochondria (Quintero et al., 2009), the golgi (Buss et al., 1998), endosomes (Raposo et al., 1999), lysosomes (Cabukusta and Neefjes, 2018), vesicles (Titus, 2018), and phagosomes (Barger et al., 2020). While this introduction provides an overview into the aspects of both conventional and unconventional myosins, the remaining work will dive deeper into how the force-generating function of unconventional myosins assist in the growth of actin-based protrusions (**Fig 1-16**).

In protrusions, myosins are localized along the entire length of all three types of mammalian actin-based protrusions: microvilli, stereocilia and filopodia, with a subset of myosins enriched at their apical tips. In microvilli, these tip-enriched myosins are myosin-7b, in stereocilia these are myosin-15a, -7a, -3a, and in filopodia this is myosin-10 (Houdusse and Titus, 2021). For the most part, these myosins can be grouped into

MYTH4-FERM domain myosins named for their shared motif (Petersen et al., 2016), and are processive, allowing them to partake in cargo transport. Indeed, in microvilli, myosin-7b aids in the transport of the IMAC complex (Weck et al., 2016), in stereocilia, myosin-15a, -3a and -7a aid in the transport the stereocilia tip link complex (cadherin-23, protocadherin-15, sans, and harmonin) (Boeda et al., 2002; Zheng et al., 2010) and in filopodia myosin-10 assists in the transport of VASP and β-integrins, to name two (Titus, 2018; Tokuo and Ikebe, 2004a). An important aspect in comprehending the function of these protrusions is unraveling how these protrusions are formed. However, both stereocilia and microvilli are situated in anatomically challenging places (the inner ear, intestine, and kidney), and no ideal cell culture models exist to study their native onset. In this regard, filopodia are a feasible model of actin-based protrusions. Most motile cells form filopodia, offering a diverse range of cell culture models for their study, and filopodia grow in an X-Y orientation (in contrast to the Z orientation seen in microvillar cell culture models) allowing for readily accessibility for microscopy. Additionally, unlike the static nature of mature microvilli and stereocilia, mature filopodia exhibit dynamic growth, retraction, and collapse, making them a valuable model to study actin-based protrusion initiation and growth. In this work we accomplish this by employing filopodia to investigate the onset of actin-based protrusions, and the involvement of force-generating, unconventional myosins in this process.

In ***Chapter III***, we experimentally determine that unconventional myosins do, in fact, contribute growth promoting forces to elongate protrusions, a process dependent on both the availability of plasma membrane and actin. In this chapter we also introduce an innovative in-cell assay designed to regulate the temporal onset of filopodia, offering a

valuable tool for future studies wanting to investigate actin-based protrusion initiation. In ***Chapter IV***, we expand this system to experimentally determine the amount of myosin motors at the tips of elongated filopodia through a molecular counting technique in live-cells. From this study, we deteremined the average amount of of force myosins contribute to elongating cell surface protrusions. In ***Chapter V***, we will conclude by discussing how these two findings expand and situate within the current models of protrusion initiation.

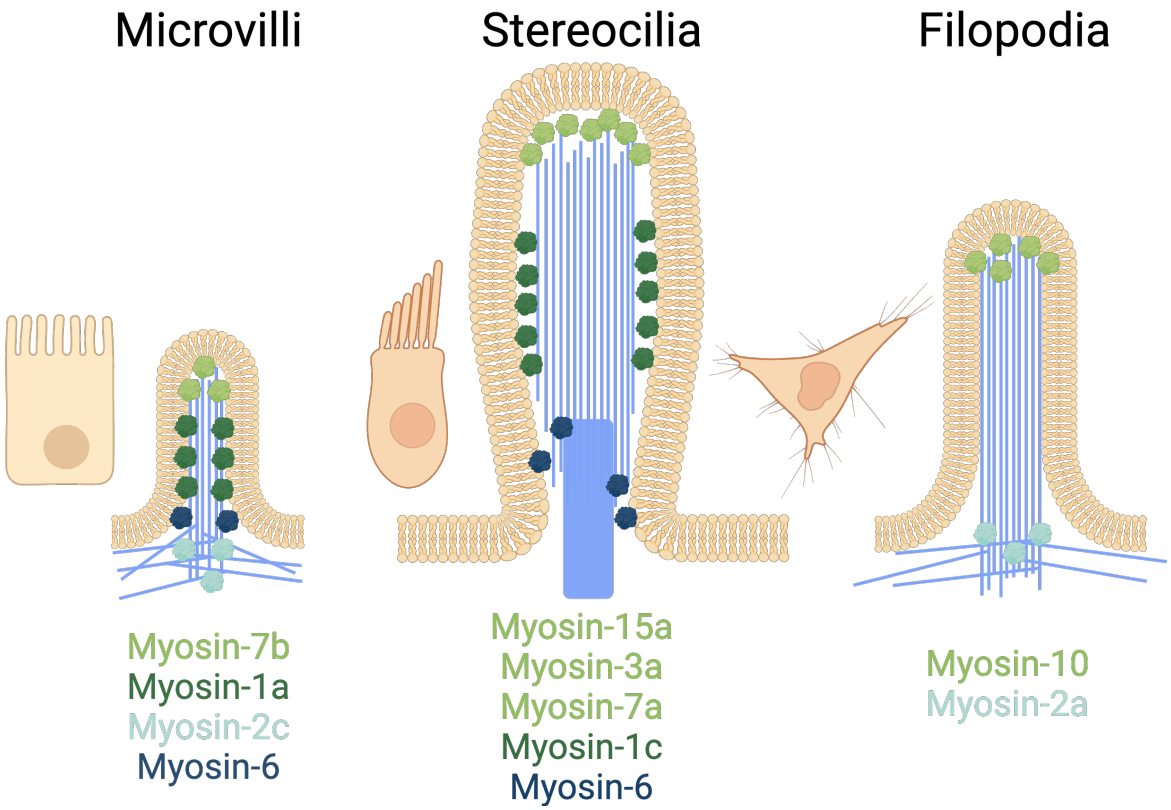

Figure 1-16: Myosins and their localization in actin-based protrusions. From left to right: microvilli (enterocytes), stereocilia (hair cells), and filopodia (motile cells) with residing myosins in green (light green: tip enriched, green: actin-membrane linking, dark green: barbed end directed myosin, teal: non-muscle myosin-2). Adapted from (Houdusse and Titus, 2021).

CHAPTER II

MATERIALS AND METHODS

Cell culture

HeLa cells were cultured at 37ºC and 5% CO_2 in Dulbecco's modified Eagle's medium (DMEM) (Corning #10-013-CV) with high glucose and 2 mM L-Glutamine supplemented with 10% fetal bovine serum (FBS). For ATP depletion experiments, transfected cells were imaged in glucose-free DMEM (Corning #11-966-025).

Cloning and constructs

All PCR amplification was completed using Q5 High-Fidelity DNA Polymerase (NEB #M0491S) for all PCR amplifications including site-directed mutagenesis for the scFV construct. For all other site-directed mutagenesis, PfuUltra High-Fidelity DNA Polymerase (in Agilent #200523 kit) was used.

Membrane interacting motifs: To generate the membrane binding motif constructs, we first generated a (1) mCherry-FKBP-myc plasmid by inserting mCherry (a.a. 1329-1564) from CDHR2-mCherry-FKBP-myc using the primers 5'-taagcagaattccatggtgagcaagggcga-3' and 5'-taagcagcggccgccactgtg-3' to amplify a PCR product of mCherry flanked by the restriction digest sites for EcoRI (NEB #R3101) and NotI (NEB #R3189). The gel purified mCherry PCR product and pcDNA3.1 Zeo+FKBP-myc (Addgene plasmid #20211) were digested with EcoRI and NotI, gel purified (Macherey-Nagel #740609.50), and ligated together (NEB M2200S). (3) CDHR2TM-

mCherry-FKBP-myc was made by amplifying the single-spanning transmembrane domain of a previously generated full-length CDHR2-mCherry-FKBP-myc plasmid. The transmembrane portion of the protein (a.a. 1-185) was amplified using the primers 5'-taagcagctagcaccatggcccagctatgg-3' and 5'-taagcacttaagcaggtccgtggtgtccagg-3' to generate a PCR product flanked by the restriction sites NheI (NEB #R0131) and AflII (NEB #R0520). Using traditional cloning, this fragment was then inserted into the mCherry-FKBP-myc plasmid. To generate the (2) mCherry-BTK-PH-FKBP-myc $PI(3,4,5)P_3$ membrane binding motif plasmid, we amplified the BTK-PH domain of *hs* Bruton tyrosine kinase (NM_000061.2) from the Addgene plasmid #51463 (a.a. 1-177) using the primers 5'-tgcttagaattcggttttaagcttccattcctgttctcca-3' and 5'-taagcaggtaccaccatggccgcagtgattctggag-3' to generate a PCR product containing BTK-PH flanked by the restriction digest sites KpnI and EcoRI. The mCherry-FKBP-myc plasmid and gel purified BTK-PH PCR product were both digested with KpnI (NEB #R3142) and EcoRI, gel purified and ligated together. To generate the (3) FKBP-myc-mCherry-TH1 electrostatic membrane binding motif plasmid, Gibson assembly (NEB #E2621) was used to assemble three fragments into pcDNA3.1 Zeo+FKBP-myc: Fragment 1: FKBP-myc (a.a. 1-117) from pcDNA3.1 Zeo FKBP-myc; Fragment 2: mCherry (a.a. 1-236) from the previously generated full length CDHR2-mcherry-FKBP-myc ; Fragment 3: TH1 domain (a.a. 772-1043) of *hs* unconventional myosin-1a (GeneBank™ AF009961) was amplified using the primers 5'-ggcggccgctcgagtctagagccctcaccttggcaga-3' and 5'-gaaggcacagtcgaggctgatcagcgggtttaaacgggcctcactgcacagtcacctccaag-3'.

Myosin motor domains: We first generated the (1) EGFP-Myo10MD-FRB-myc construct by inserting the motor domain of *Hs* myosin-10 (a.a. 1-855) into the pcDNA3.1 Zeo+FRB-myc (Addgene plasmid #20228) plasmid by Gibson assembly. The motor domain was amplified was using the primers 5'-tatagggagacccaagctgggccaccatggtgagcaag-3' and 5'-actgtgctggatatctgcagcctgcttcctccgttgggc-3' and the FRB-myc plasmid was linearized by restriction enzyme incubation with NheI and EcoRI. For the additional motor domain constructs, we generated an (2) EGFP-FRB-myc plasmid to insert various motor domains into by amplifying EGFP (a.a. 1-239) from EGFP-Myo10MD-FRB using the primers 5'-taagcaaagcttaccatggtgagcaagggcg-3' and 5'-taagcagaattcagatctgagtccggacttgtacagc-3' to generate a PCR product containing EGFP flanked by HindIII and EcoRI. The FRB-myc plasmid and gel purified EGFP PCR product were both digested with HindIII (NEB #R3104) and EcoRI, gel purified and ligated together. To generate the two motor domain dead constructs (G437A , switch II and R220A, switch I) we utilized site-directed mutagenesis (Agilent #200523) of EGFP-Myo10MD-FRB to induce the two, separate amino acid changes using the primers 5'-cacctcaaagttttcaaatgcaaagatgtccaagatgcc-3' and 5'-ggcatcttggacatctttgcatttgaaaactttgaggtg-3' for (3) EGFP-Myo10MDxG437A-FRB-myc and 5'-ctgaacaaacttcccgaaggcactggagttattgttgtac-3' and 5'-gtacaacaataactccagtgccttcgggaagtttgttcag-3' for (4) EGFP-Myo10MDxR220A-FRB-myc. To generate the (5) EGFP-Myo6MD-FRB-myc plasmid, Gibson assembly was used to assemble three fragments of *hs* unconventional myosin-6 (GenBank #NM_001300899.2) to replace the Myo10MD in EGFP-Myo10MD-FRB-myc: Fragment 1: a.a. 1-294 was amplified using the primers 5'-agatctcgaatcacaagtttgtacaaaaaagcaggctccgaaatggaggatggaaagcccgt-3' and 5'-

cggttctgtaaaatctgtttgtcagtttcttt-3'; Fragment 2: a.a. 295-576 was amplified using the primers 5'-ttgctaacaaagaaactgacaaacagattttacag-3' and 5'-gccttcgtcgtctctgatattcctatgaactg-3'; Fragment 3: a.a. 577-844 was amplified using the primers 5'-taagctggcagttcataggaatatcagagacg-3' and 5'-cagaggattctagactcgagcggccgccactgtgctggattgcccaccttaaccagacca-3'. The backbone (EGFP-Myo10MD-FRB-myc) was linearized by restriction digest via EcoRV (NEB #R3195) and EcoRI. The myosin-3a lacking the N-terminal kinase (ΔK) plasmid was kindly gifted to us by Dr. Christopher Yengo. (6) EGFP-Myo3aΔK-FRB-myc was generated using Gibson assembly to insert the Myo3aΔKMD (a.a. 407-1432) into the EGFP-FRB-myc plasmid. The Myo3aΔMD was amplified using the primers 5'-cacagtggcggccgctcgaggtagatgatttagcaaccctagaagttttgga-3' and 5'-cacatctcatgccagaggataaaagaagacatcttgtccttcctcaact-3', and the EGFP-FRB-myc plasmid was linearized using the primers 5'-aggacaagatgtcttcttttatcctctggcatgagatgtgg-3' and 5'-agggttgctaaatcatctacctcgagcggccgcc-3'. The *Mm* myosin-15a (NM_182698) plasmid was kindly gifted to us by Dr. Uri Manor. The (7) EGFP-Myo15aMD-FRB-myc plasmid was generated using Gibson assembly to insert the motor domain of myo15a (a.a. 1-750) into EGFP-FRB-myc. The Myo15aMD was amplified using the primers 5'-cacagtggcggccgctcgagatgcactccatacgcaacctgcc-3' and 5'-atctcatgccagaggattctcagcagactctgcctcatct-3', and the EGFP-FRB-myc backbone was linearized by PCR using the primers 5'-agatgaggcagagtctgctgagaatcctctggcatgagatgtggc-3' and 5'-aggttgcgtatggagtgcatctcgagcggccgcc-3'. The (8) EGFP-Myo7bMD-FRB-myc plasmid was generated using Gibson assembly to insert EGFP and the motor domain (a.a. 1 -

968) of *Hs* myosin-7b (NM001393586.1) into FRB-myc. EGFP and the myosin-7b motor domain were amplified by PCR using the primers 5'-tatagggagacccaagctgggccaccatggtgagcaag-3' and 5'-actgtgctggatatctgcagcccaggccatccacatcctc-3' and the FRB-myc backbone was linearized by restriction digest with the enzymes NheI and EcoRI. The *Hs* myosin-5b plasmid was kindly gifted to us by Dr. James R. Goldenring. The (9) EGFP-Myo5bMD-FRB-myc plasmid was generated using Gibson assembly to insert the motor domain of myosin-5b (a.a. 1-910) into EGFP-FRB-myc. The myosin-5b motor domain fragment was amplified using the primers 5'-acaagtccggactcagatctatgagcgtgggcgagc-3' and 5'-aggattctagactcgagcggggcctcgattctcagggc-3', and the EGFP-FRB-myc plasmid was linearized by PCR using the primers 5'-aagccctgagaatcgaggccccgctcgagtctagaatcctctgg-3' and 5'-tacagctcgcccacgctcatagatctgagtccggacttgtacag-3'. The (10) EGFP-Myo5bΔ3IQ-FRB-myc was generated by amplifying a fragment containing the motor domain and first three IQ motifs (a.a. 1-831) from EGFP-Myo5b-FRB-myc, flanked by EcoRI sites using the primers 5'-taagcagaattctccggactcagatctatgagcgtgg-3' and 5'-taagcagaattcggcctgtctggcccg-3'. Using traditional cloning, this fragment was then inserted into EGFP-FRB-myc. The (11) EGFP-Myo1aMD-FRB-myc plasmid was generated by amplifying the motor domain (a.a. 1-771) of *Hs* myosin-1a (NM001256041.2) using the primers 5'-agtccggactcagatctgaaatgcctctcctggaaggt-3' and 5'-attctagactcgagcggccgagcctctgaccggaaatatttgc-3'. Using Gibson assembly, this fragment was then inserted into a PCR linearized EGFP-FRB-myc backbone using the primers 5'-aatatttccggtcagaggctcggccgctcgagtctaga-3' and 5'gaaccttccaggagaggcatttcagatctgagtccggacttgtaca-3'. For all plasmids, colonies were

first screen by restriction digest to confirm the correct digested band pattern and then verified by sequencing (GENEWIZ, South Plainfield, NJ or Plasmidsaurus, Eugene, OR).

Myosin-10 Motor Domain GCN4 Linkers: To generate the GCN4 linkers (4x-, 8x-, 12x-, 16x-, 18x-, 20x-, 24x-) tagged to Myo10MD-FRB, we replaced the EGFP from the previously generated EGFP-Myo10MD-FRB (above) with GCN4 repeats from pHRdSV40-K560-24xGCN4_v4 (addgene #72229) via Gibson assembly (NEB #E2621S) using the following primer sets: (24x) 5'-acccaagctgggccaccatggaagaacttttgagcaagaattatcatcttgagaacgaagtg-3' and 5'-attcgagatctgagtccggacttttttaagtcgggctacttcattctcgaga-3', (20x) 5'-acccaagctgggccaccatggaagaacttttg-3' and 5'-

- attcgagatctgagtccggacttctttagtcgagccacctcgttctcg -3', (18x) 5'-acccaagctgggccaccatggaagaacttttgagcaagaattatcatcttgagaacgaagtg-3' and 5'-attcgagatctgagtccggatttcttcaagcgggcgact -3' , (16x) 5'-acccaagctgggccaccatggaagaacttttgagcaagaattatcatcttgagaacgaagtg -3' and 5'-attcgagatctgagtccggatttttttgagcctggcgacttca -3', (14x) 5'-acccaagctgggccaccatggaagaacttttgagcaagaattatcatcttgagaacgaagtg -3' and 5'-attcgagatctgagtccggatttcttcaatctcgcgacctcattc -3', (12x) 5'-acccaagctgggccaccatggaagaacttttgagcaagaattatcatcttgagaacgaagtg -3' and 5'-attcgagatctgagtccggatttctttaagcgcgcgacttcgttctctaaatgatag -3', (8x) 5'-acccaagctgggccaccatggaagaacttttgagcaagaattatcatcttgagaacgaagtg-3' and 5'-attcgagatctgagtccggatttctttaatcgagctacttcgttttcgagg -3', (4x) 5'-

acccaagctgggccaccatggaagaacttttgagcaagaattatcatcttgagaacgaagtg -3' and 5'-attcgagatctgagtccggacttttttagccgagccacttcgttt -3'.

Myosin-10 Full Length 18x GCN4 Linker: To generate the full length myosin-10 18x GCN4 construct, we replaced EGFP from EGFP-Myo10FL (used above) with 18xGCN4 using Gibson assembly with the following primers: 5'- tccggccggactcaga-3' and 5'-ggtggcgaccggtagc-3' (EGFP-Myo10FL) and 5' tagtgaaccgtcagatccgctagcgctaccggtcgccaccATGgaagaactgctt-3' and 5'-cggggaagaagttgtccattgagatctgagtccggccggaGATTCGAGATCTGAGTCCGGAtttcttcaag-3' (18xGCN4-Myo10MD construct).

scFV-GFP: We generated scFV-GFP by removing the nuclear localization sequence via an early stop codon from pHR-scFv-GCN4-sfGFP-GB1-NLS-dWPRE (Addgene #60906) with the following primers: 5'- tggtagctgaggtggtactagtcccaagaagaagc-3' and 5'-ccacctcagctaccaccaccttcggttacc-3'. The reaction was then digested with DpnI (NEB #R0176S).

Transfections

Rapalog-inducible system experiments:

Transfections were performed using Lipofectamine 2000 (Thermo Fischer #11668019) according to the manufacturer's protocol. Cells were incubated in Lipofectamine for 4-6 hrs, after which they were replated onto 35mm glass-bottom dishes (Cellvis #D35-20-1.5-N) and/or coverslips coated with 25 ug/mL laminin (Corning #354232) and allowed to adhere and recover overnight before live imaging or fixing/staining. For DIAPH1 (mDia1)

knock down (KD) experiments, HeLa cells were transfected twice with either 10 μM of Accell human DIAPH1 siRNA SMARTPool (Horizon Discovery #E-010347-00-0005) or Accell non-targeting control pool (Horizon Discovery #D-001910-10-05). Cells were allowed to recover overnight before being transfected a second time with their respective siRNA pools. On the third day, HeLa cells were transfected with the EGFP-Myo10MD-FRB and CDHR2TM-mCherry-FKBP constructs and replated as described above.

18x-GCN4 experiments:

Transfections were performed using Lipofectamine 2000 (Thermo Fischer #11668019) according to the manufacturer's protocol. 2.5 x 10^5 HeLa cells were resuspended and incubated in Lipofectamine for 16 hrs in 35mm glass-bottom dishes (Cellvis #D35-20-1.5-N) before being rinsed once in 1X PBS and replaced with media and live imaged.

Drug treatments

To oligomerize FRB and FKBP constructs, transfected cells were treated with 500 nM of A/C Heterodimerizer (Takara #635057) at the onset of live imagining. To deplete ATP for the ATP depletion experiments, transfected HeLa cells were switched to glucose free DMEM (Fischer #11-966-025) supplemented with 2 mM L-glutamine and 10% FBS. Before the onset of live cell imaging, 35mM were spiked with 0.05% sodium azide (Fischer #UN1687) and 10 mM 2-deoxy-d-glucose (Sigma #D3179). For live-cell imaging of individual filopodia, 0.5% methylcellulose diluted in DMEM with high glucose and 2 mM L-Glutamine supplemented with 10% FBS was added prior to imaging.

Light microscopy and image processing

Laser scanning confocal imaging was conducted using a Nikon A1 Microscope equipped with 405, 488, 561, and 645 nm LASERs, Plan Apo 60X/1.4NA, and Plan Apo 25X/ 1.05 NA silicon (SIL) immersion objectives. Live-cell imaging was performed on a Nikon Ti2 inverted light microscope equipped with a Yokogawa CSU-X1 spinning disk head, equipped with 488 nm, 561 nm, and 647 nm excitation LASERs, a 405 nm photo-stimulation LASER directed by a Bruker mini-scanner to enable targeted photobleaching, a 100X Apo TIRF 100x/1.45 NA objective, and either a Hamamatsu Fusion BT or Photometrics Prime 95B sCMOS camera. Cells were maintained in a stage top incubator at 37ºC with 5% CO2 (Tokai Hit). For imaging in all microscope modalities, imaging acquisition parameters were matched between samples during image acquisition. For imaging of individual puncta, a single z-stack acquisition was taken for 5 sec at 0.05-0.06 ms/frame prior to depleting ATP. ATP depletion media was then added and 15 min later, the same cells were imaged for 5 s at 0.05-0.05 ms/frame. For imaging the tips of filopodia that had elongated, a 0.5 μm z-stack was acquired, rapalog was added to induce filopodia elongation, and after 30 m the same cell was imaged using a 3.0 μm z-stack to acquire 3D volume tip information. For imaging to quantify the dynamic properties of filopodial elongation based on motor number, transfected cells were imaged every 15 sec for 30 m using a 0.5 μm z-stack, and at the end of 30 m a single, 3.0 μm z-stack was taken. All images were denoised and deconvolved in Nikon Elements. As filopodia are thin structures, LUTs were optimized to facilitate visualization in figures.

Quantification and statistical analysis

All images were processed and analyzed using Nikon Elements software or FIJI software (https://fiji.sc/).

Analysis of individual Myo10MD puncta after ATP depletion. Fiji's TrackMate was used to quantify the sum intensity of individual puncta. TrackMate was run under the following parameters: all 82 frames were included, DoG detector, 0.5 μm diameter with a 0.75 quality threshold, no initial thresholding restrictions, LAP tracker, 1.0 μm max distance frame linking, allow gap closing with a max distance of 0.5 μm with a max gap frame of 2. Puncta were removed if seen in the intial image prior to ATP depletion, and puncta were only included if they remained in frame for 15 or more frames. An average sum intensity was then taken of the sum intensity of each punctum over the 15 or more frames it appeared. For background puncta, the same sized ROI from TrackMate was used to measure 100 points background sum intensity from each of the 4 separate imaging days. The intensity of a single Myo10MD punctum was then measured as the average of all Myo10MD puncta measured minus the average background intensity.

Analysis of the number of motors at the tips of filopodia. Prior to inducing filopodial elongation, we generated a single image with low z-resolution (0.5 μm) of transfected HeLa cells. Transfected HeLa cells were then induced to elongate filopodia, and after 30 min a single image with high z-resolution (3 μm) was captured. A 2 x 2 μm crop of filopodial tips was then taken from any filopodial that had emerged compared to the initial low z-resolution image. This cropped tip was then threshold in using the green, Myo10MD,

channel in Nikon Elements to capture the sum intensity of the tip. Using the background pixel intensity from our single puncta analysis, we then quantified the number of voxels (3D pixel) were captured in the 3D tip and subtracted the number of voxels multiplied by the background intensity from the 3D tip. This value was then divided by the background subtracted individual puncta to identify the number of Myo10MDs in each individual filopodial tip.

Measuring the dynamics of induced filopodia. Lengths, tracks, and persistence of elongating filopodia were analyzed using "tracking" in Nikon Elements using the Myo10MD tip intensity. Lengths were measured with line length (length of a straight line from the track origin to the current point), radial tracks were normalized to set the origin to (0,0), and persistence was measured as the line length divided by the path length (sum of the segment distances from the first frame to the current frame) of each individual track. Rate was calculated as the slope of the line fit via simple linear regression to the length over time; each individual track was analyzed to include the start of elongation and stopped when a length plateau was reached.

Statistical analysis. For the purpose of generating SuperPlots(Lord et al., 2020) we considered the number of individual cells equivalent to the number of biological replicates; this approach allowed us to build plots that communicate the variability between cells *and* between individual punctum. All experiments were completed at least in triplicate and the number of biological replicates (n) in each case is defined in each figure legend. Statistical significance was performed using the unpaired Student's t-test for comparisons and the

paired Student's t-test for comparisons of the sum intensities of punctum without and with ATP depletion. All statistical analysis were computed using PRISM v.10.0.2 (GraphPad).

CHAPTER III

PROTRUSION GROWTH DRIVEN BY MYOSIN-GENERATED FORCE

This chapter is adapted from Protrusion growth driven by myosin-generated force originally published in Developmental Cell (Fitz et al., 2023) and has been reproduced with the permission of the publisher and my co-authors Weck ML, Bodnya C, Perkins OL, and Tyska MJ.

ABSTRACT

Actin-based protrusions are found on the surface of all eukaryotic cells, where they support diverse biological activities essential for life. Models of protrusion growth hypothesize that actin filament assembly provides the mechanical force for bending the plasma membrane outward. However, membrane-associated myosin motors are also abundant in protrusions, though their potential for contributing growth-promoting force remains unexplored. Using a novel inducible system that docks myosin motor domains to membrane binding modules with temporal control, we found that the application of myosin-generated force to the plasma membrane is sufficient for driving robust elongation of protrusions. Protrusion growth scaled with motor accumulation, required active, barbed end-directed force, and was independent of cargo delivery or the recruitment of canonical barbed end elongation factors. Application of growth-promoting force was also supported by structurally distinct myosin motor domains and membrane binding modules. We

conclude that myosin-generated force can drive protrusion growth and this mechanism is likely active in diverse biological contexts.

INTRODUCTION

Actin-based membrane protrusions are ancient cell surface features that have evolved to perform a vast array of biological roles needed for cell function and survival. Microvilli, stereocilia, and filopodia represent a group of structurally related protrusions supported by a core bundle of actin-filaments (Mooseker and Tilney, 1975; Small, 1988; Tilney et al., 1980). Despite a common morphology, these structures serve distinct physiological functions: microvilli drive nutrient absorption in the gut, stereocilia regulate hearing and balance in the ear, and filopodia contribute to a range of functions including cell migration, cell-cell adhesion, and neurite outgrowth (Houdusse and Titus, 2021). While the function, structure and composition of actin-based protrusions have been studied extensively for decades, the physical mechanisms that control their assembly are still emerging.

A key step in protrusion growth is deformation of the plasma membrane. Previous theoretical and experimental work suggested that positive (i.e. outward) membrane curvature is driven by the mechanical force generated during actin monomer incorporation at the membrane-proximal barbed ends of growing filaments (Footer et al., 2007b; Hill and Kirschner, 1982a; Hill and Kirschner, 1982b; Kovar and Pollard, 2004b; Mogilner and Oster, 1996a; Mogilner and Oster, 1996b; Mogilner and Rubinstein, 2005; Peskin et al., 1993; Theriot, 2000). Elongation factors such as formin family proteins and enabled/vasodilator-stimulated phosphoprotein (Ena/VASP) have also been implicated in

accelerating protrusion elongation, potentially by promoting rapid and processive incorporation of monomers at the membrane interface (Bear et al., 2002; Higashida et al., 2004; Kovar and Pollard, 2004b). However, a recent study found that protrusion length is not tightly coupled to the levels of these canonical elongation factors (Dobramysl et al., 2021b), highlighting the ambiguity of mechanisms that drive growth.

Although actin filament polymerization can drive protrusion growth, the potential for other force generators to contribute to this process has remained unclear. Indeed, myosin superfamily members are some of the most abundant residents of actin-based protrusions (Jacquemet et al., 2019; Krey et al., 2017; McConnell et al., 2011) and may hold the potential to generate significant growth-promoting force. All myosins consist of three structural domains: a conserved N-terminal motor domain that binds actin and hydrolyzes ATP, a central neck that serves as a lever arm to amplify motion produced during the power stroke (Rayment et al., 1993; Uyeda et al., 1996; Warshaw et al., 2000), and a class-specific C-terminal tail domain (Sellers, 2000). Myosin tail domains mediate cargo binding and association with the plasma membrane (either directly or indirectly). Of all myosin classes, protrusions contain primarily barbed end directed-myosins: microvilli contain myosin-1a, -1d, and -7b (Benesh et al., 2010; Chen et al., 2001; Conzelman and Mooseker, 1987), stereocilia contain myosin-7a, -3a, and -15a (Belyantseva et al., 2003; Hasson et al., 1995; Schneider et al., 2006), and filopodia contain myosin-7 (Petersen et al., 2016) and myosin-10 (Berg et al., 2000). Several of these motors accumulate in the distal tip compartment, which presumably reflects their robust barbed end-directed movement in these systems. Consistent with this view, previous studies implicate myosins in the delivery of critical regulatory and structural cargoes to the distal tips, suggesting

that these motors are important regulators of growth (Houdusse and Titus, 2021). Indeed, loss-of-function studies with tip-targeting myosins generally result in a loss of distal tip components and shorter protrusions in all three systems (Belyantseva et al., 2003; Bohil et al., 2006; Weck et al., 2016).

Beyond interacting directly with cargo proteins, the tail domains of myosins also interact with the plasma membrane, either directly or indirectly. Some myosins bind directly to the inner leaflet of the membrane through non-specific electrostatic interaction mediated by their highly basic C-terminal tail (Feeser et al., 2010; Mazerik and Tyska, 2012). Others interact with the plasma membrane using motifs that bind to specific membrane lipid head groups (Hokanson and Ostap, 2006; Plantard et al., 2010), or through interactions with membrane-associated peripheral or transmembrane proteins (Crawley et al., 2014; Yu et al., 2017; Zhang et al., 2004b). From this perspective, myosin motors are well-positioned to exert significant force on the membrane, and consequently, impact the kinetics of protrusion growth. However, this hypothesis remains untested due to the technical challenge of uncoupling the contributions of tipward cargo transport from myosin tail membrane interactions.

To address this challenge and determine if membrane-bound myosin-generated force promotes protrusion growth, we developed a synthetic cell-based system that allows for temporally controlled docking of myosin motor domains (lacking cargo binding motifs) to the membrane. Our studies initially leverage the motor domain from the well-studied filopodia resident motor, myosin-10 (Myo10). Myo10 walks towards the barbed ends of polarized actin filament bundles, enriches at the distal tips of filopodia, and is sufficient for the initiation of filopodia formation and subsequent elongation (Berg and Cheney,

2002). Moreover, the Myo10 tail binds to cargoes (Tokuo and Ikebe, 2004a) that are critical for filopodial function, but also interacts with the plasma membrane using a several distinct mechanisms (Plantard et al., 2010; Zhang et al., 2004b). We found that membrane-bound Myo10 motor domains drive robust cell surface protrusion elongation independently of cargo binding and delivery activities. Live-cell and super-resolution imaging studies indicate that while the induced protrusions share many common features with canonical filopodia, they elongate independent of the formin, mammalian diaphanous-related formin 1 (mDia1), and VASP, suggesting myosin-generated force circumnavigates the usual requirement for these factors. Motor domain-driven filopodial elongation was also supported by a variety of membrane binding motifs, although integral membrane motifs produced the most robust response. Elongation activity was not specifically dependent on the mechanical properties of Myo10, as the motor domains from stereocilia motors, myosin-15a and -3a, also promoted filopodia growth. These data reveal that the application of myosin-generated force to the plasma membrane can directly drive protrusion growth.

RESULTS

Membrane-bound Myo10 motor domains drive robust protrusion elongation, independent of cargo binding.

To investigate the role of myosin-generated force in protrusion growth, we used a rapalog inducible system that offers switchable control over the oligomerization of proteins tagged with FRB and FKBP (Banaszynski et al., 2005; Inobe and Nukina, 2016). These modules were used to engineer constructs that enabled us to rapidly induce

interaction between myosin motor domains (tagged with FRB) and plasma membrane binding motifs (tagged with FKBP) upon the addition of rapalog (**Fig 3-1A**). We first examined the effect of docking the motor domain from the filopodial motor, Myo10, to the plasma membrane in live HeLa cells. To eliminate cargo binding and specifically probe how the application of force to the membrane affects protrusion growth, we replaced the entire C-terminal tail of Myo10 with FRB (a.a. 1-855, EGFP-Myo10MD-FRB, herein referred to as Myo10MD) (**Fig 3-1B**). For a membrane-binding motif, we used the transmembrane domain (TM; a.a. 1155-1310) from cadherin related family member 2 (CDHR2), a single-spanning membrane protein not endogenously found in HeLa cells (CDHR2TM-mCherry-FKBP, herein referred to as CDHR2TM) (**Fig 3-1B**). Using live-cell spinning-disc confocal (SDC) microscopy, we visualized cells expressing both Myo10MD and CDHR2TM, imaging every 5 minutes before and after the addition of rapalog (**Fig 3-1C**). Upon rapalog treatment, we noticed clear relocalization of the Myo10MD signal from the cytoplasm to the cell periphery, as expected based on the plasma membrane localization of CDHR2TM. Strikingly, cells displayed a robust elongation of finger-like protrusions within 10 minutes of rapalog treatment compared to untreated control cells (**Fig 3-1D, 3-1E - compare Fig 3-1Dii to 3-1Eii- Fig 3-1F**). Additionally, cells expressing the Myo10MD construct alone (in the absence of the membrane binding construct) failed to elongate filopodia in response to rapalog treatment (**Supp Fig 3-1**). While we were able to directly visualize *de novo* protrusion growth events in our time-lapse data, and the number of protrusions did trend upward, this increase was not significant (**Fig 3-1G**). However, protrusion length increased significantly when Myo10MD was docked to the

membrane (**Fig 3-1H, 3-1I**), suggesting that myosin-generated forces contribute primarily to elongating existing structures rather than initiating new ones.

To determine if protrusion growth induced by membrane-bound Myo10MD was unique to HeLa cells, we co-expressed our system components in B16F1 *Mus musculus* melanoma cells, which also form fascin-bundled filopodia, and LLC-PK1-CL4 (CL4) *Sus scrofa* kidney cells, which form microvilli on their apical surface. Induction of Myo10MD membrane binding in both cell lines drove robust protrusion elongation. Thus, the application of myosin-generated force to the plasma membrane is sufficient for driving protrusion growth in distinct cell types derived from a range of tissues (**Supp Fig 3-1**).

Protrusions induced by membrane-bound Myo10MD exhibit features of filopodia.

We next sought to determine if the protrusions induced by membrane-bound Myo10MD represent canonical filopodia. To this end, HeLa cells were fixed 25 minutes after the addition of rapalog, and then stained for F-actin (phalloidin)(Vandekerckhove et al., 1985) and the filopodia-specific parallel filament bundler, fascin (Vignjevic et al., 2006b). Super-resolution structured illumination microscopy (SIM) of these samples revealed that protrusions induced by membrane-bound Myo10MD contained both F-actin and fascin (**Fig 3-2A, 3-2B, Supp Fig 3-2)**. We also analyzed SDC time-lapse data and determined that individual protrusions induced by membrane bound Myo10MD elongated at a similar rate to canonical filopodia. Individal protrusions induced by membrane-bound Myo10MD elongated at 2.16 μm/min, a rate similar to that reported for filopodia in previous studies (~2.2 μm/min)(Schäfer et al., 2011)(**Fig 3-2C, 3-2Ci zoom, 3-2D**). Based

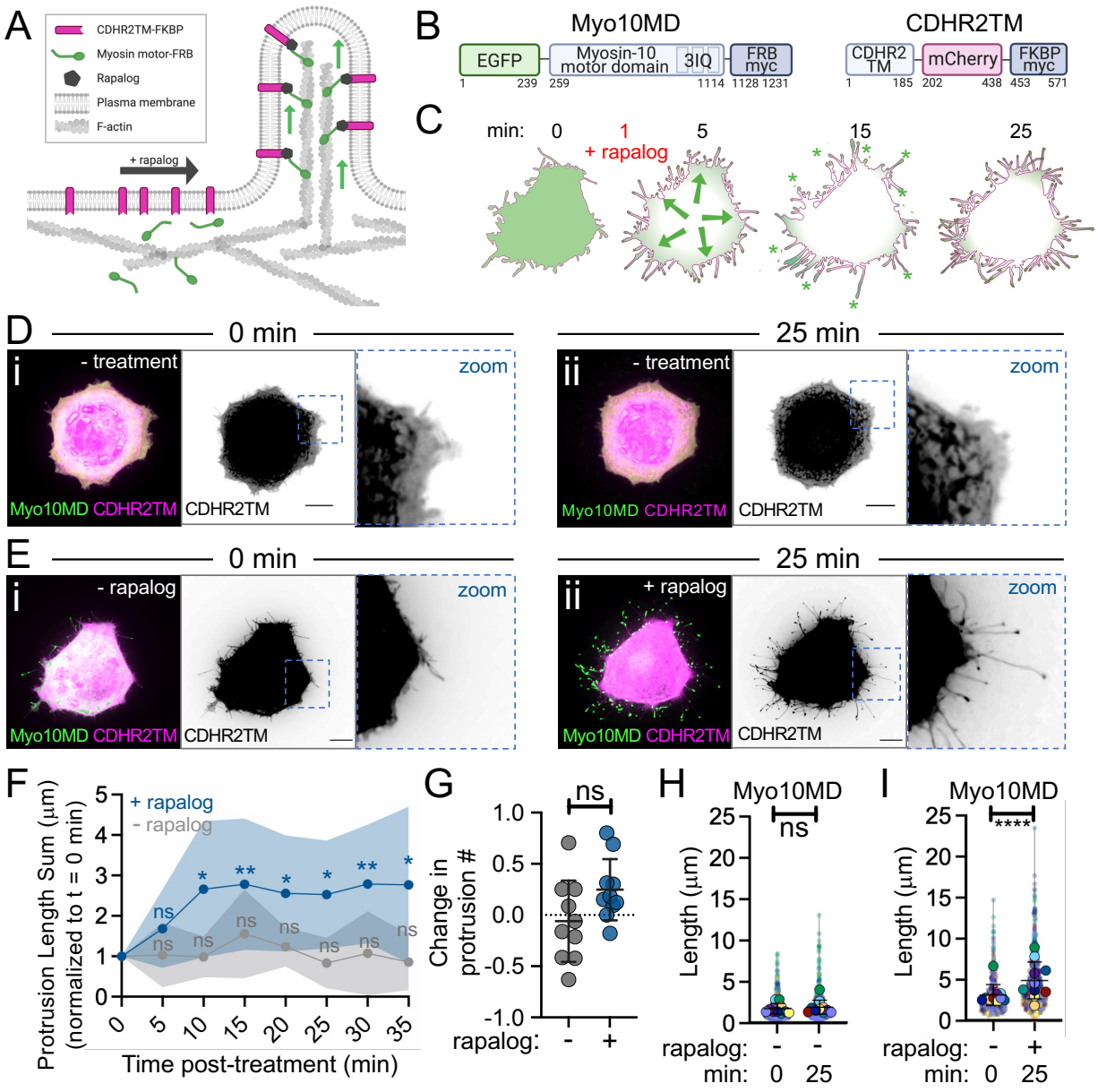

Figure 3-1: Membrane bound myosin-10 motor domains drive protrusion elongation. (**A**) Cartoon of the rapalog inducible system used to dock the myosin motor domains onto the plasma membrane. (**B**) Cartoons depicting the CDHR2TM and Myo10MD constructs for these experiments; numbers represent amino acids. (**C**) Cartoon depicting the timeline of rapalog addition and the resultant relocalization of the Myo10MD (green) construct to the CDHR2TM-labeled plasma membrane (magenta). Green asterisks mark Myo10MD enrichment at the tips of protrusions. (**D**) Confocal maximum intensity projection images of control HeLa cells expressing Myo10MD (green) and CDHR2TM (magenta) at 0 min (**i**) and 25 min (**ii**) with no rapalog treatment. (**E**) Confocal maximum intensity projection of HeLa cells expressing Myo10MD (green) and CDHR2TM (magenta) at 0 min (**i**) and 25 min after (**ii**) rapalog treatment. (**F**) Length sum of protrusions over time in untreated (gray) or rapalog treated (blue) HeLa cells expressing Myo10MD and CDHR2TM; *n* = 10 individual cells

for each treatment. (**G**) Fractional change in protrusion number from 0 min to 25 min in untreated (gray) or rapalog treated (blue) HeLa cells expressing Myo10MD and CDHR2TM; *n* = 10 individual cells for each condition. (**H**) Length of individual protrusions measured at 0 min and 25 min in untreated HeLa cells expressing Myo10MD and CDHR2TM; *n* = 10 individual cells, *n* = > 650 individual protrusions. (**I**) Length of individual protrusions measured at 0 min and 25 min post rapalog treatment in HeLa cells expressing Myo10MD and CDHR2TM*; n* = 10 individual cells, *n* = > 550 individual protrusions. Data in **(H**) and (**I**) are represented as a SuperPlot, where transparent circles represent the length of individual protrusions, opaque circles represent the average length of protrusions of individual cells, violin plots show the distribution of the data, and all color matched circles represent measurements from the same cell. All graph error bars represent the mean ± SD; ns, p-value > 0.05, * p-value ≤ 0.05, **** p-value ≤ 0.0001. Scale bars = 10 μm.

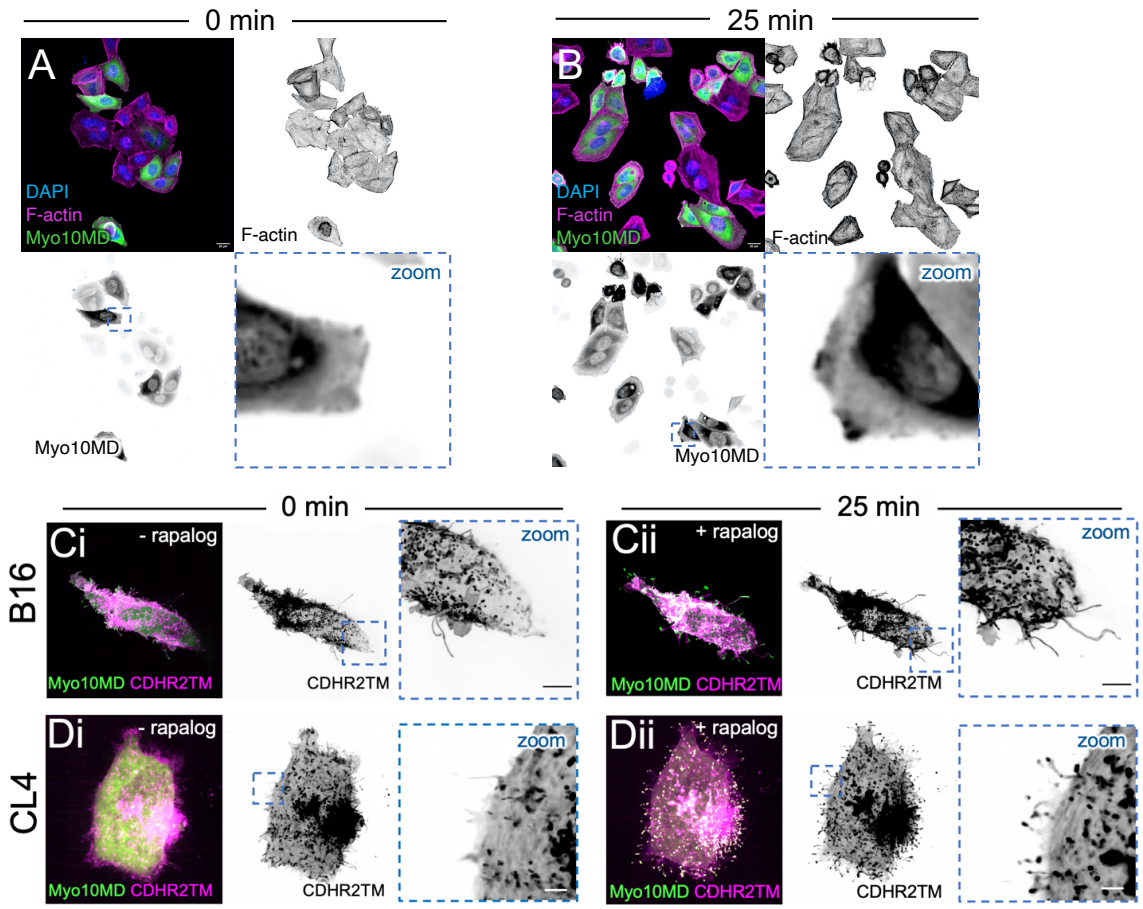

Supp Figure 3-1, related to Figure 3-1: Myo10MD cannot elongate filopodia without the membrane attachment motif, and membrane bound Myo10MD can elongate filopodia in distinct cell types. Merged confocal maximum intensity projection of HeLa cells expressing only the Myo10MD (green) constructs treated without (**A**) or 25 min after (**B**) rapalog treatment. Inverted single channel image of F-actin to the right of merged images and inverted single channel image of Myo10MD and a zoom below. Scale bars = 20 μm. (**C**) Merged confocal maximum intensity projection of B16 cells expressing Myo10MD (green) and CDHR2TM (magenta) at 0 min (**Ci**) and 25 min after (**Cii**) rapalog treatment. (**D**) Merged confocal maximum intensity projection of CL4 cells expressing the Myo10MD (green) and CDHR2TM (magenta) at 0 min (**Di**) and 25 min after (**Dii**) rapalog treatment. Scale bars = 10 μm.

on current models of filopodial growth, we also expected that protrusion growth induced by membrane-bound Myo10MD would require actin polymerization. Indeed, HeLa cells treated with the actin poisons cytochalasin D (caps filament barbed ends) and latrunculin A (sequesters actin monomers), exhibited significantly reduced protrusion elongation in response to rapalog induction (**Supp Fig 3-2C, 3-2D**). Thus, protrusions induced by membrane-bound Myo10MD are similar to canonical filopodia in that they are supported by parallel, fascin-bundled actin filaments, and require both uncapped barbed ends and a pool of free actin monomers to elongate.

Membrane-bound Myo10MD promotes filopodial growth independent of barbed end elongation factors.

Previous studies identified barbed end elongation factors as proteins that enrich at the distal ends of filopodia and in turn promote their growth. Ena/VASP and formin family proteins are well-studied examples (Bear et al., 2002; Higashida et al., 2004) and we sought to determine if membrane-bound Myo10MD promoted filopodial growth by recruiting these factors. We first examined HeLa cells for the enrichment of Ena/VASP at the tips of induced filopodia. Ena/VASP is a tetrameric protein that promotes actin monomer incorporation into filaments and protects barbed ends from capping protein, which would otherwise stall core bundle elongation. VASP binds to full-length Myo10 and may be transported to the distal ends of filopodia via this interaction (Tokuo and Ikebe, 2004a), although the possibility of such direct transport is eliminated in our experimental system as Myo10MD constructs lack the C-terminal tail. Using SIM, we visualized cells transfected with either full-length Myo10 or the combination of Myo10MD and CDHR2TM that drives filopodial induction. As expected, filopodia generated by over-expressing full

length Myo10 displayed prominent VASP enrichment at their distal tips (**Fig 3-2E, 3-2F**). Remarkably, VASP was undetectable at the tips of filopodia induced by membrane-bound Myo10MD (**Fig 3-2G, 3-2H**). We also asked if formin family proteins were involved in the rapalog-induced response. Based on RNAseq data (Uhlen et al., 2015), mDia1 is the most highly expressed formin in HeLa cells. Moreover, previous studies implicate mDia1 as a processive elongator of actin filaments in filopodial core bundles (Higashida et al., 2004). To examine potential involvement of mDia1, we knocked down its expression in HeLa cells using siRNA (**Supp Fig 3-2E**), transfected cells with Myo10MD and CDHR2TM, and induced filopodial growth with rapalog treatment. Interestingly, we observed no change in the fraction of cells that were able to elongate filopodia in mDia1 KD cells relative to controls, and no change in filopodial length (**Fig 3-2I, 3-2J, Supp Fig 3-2F**). Although these results do not rule out the possibility that Myo10MD cooperates with some actin regulatory machinery to drive filopodial elongation, this activity appears to be independent of the canonical barbed end elongation factors VASP and mDia1.

Filopodial elongation temporally correlates with Myo10MD accumulation at the distal tips.

We next sought to determine how membrane-bound Myo10MD elongates filopodia in the absence of barbed end elongation factors. One possibility is that mechanical force applied by Myo10MD directly to the plasma membrane promotes growth by reducing the physical barrier to protrusion elongation. A testable prediction that emerges from this hypothesis is that active, barbed end-directed force generation by membrane-bound Myo10MD is required to induce filopodial growth in response to rapalog treatment. To test this, we first sought to determine if higher levels of Myo10MD, and therefore, higher levels

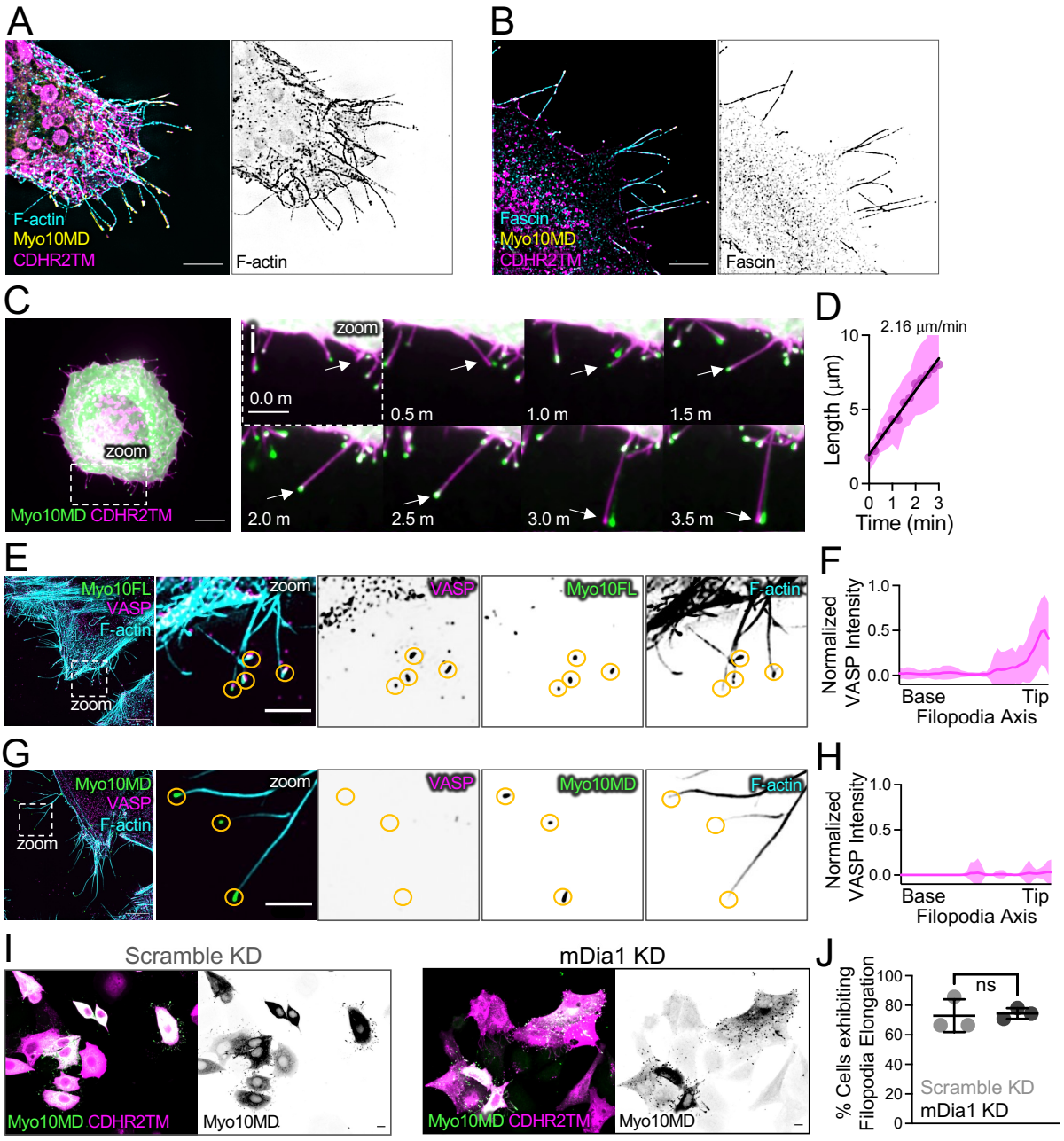

Figure 3-2: Protrusions induced by membrane bound Myo10MD exhibit features of filopodia. (**A**) SIM maximum intensity projection image of a HeLa cell expressing Myo10MD (yellow) and CDHR2TM (magenta) and stained for F-actin with phalloidin (cyan). Panel to the right shows inverted single channel image of F-actin (phalloidin). Scale bar = 5 μm. (**B**) SIM maximum intensity projection image of HeLa cells expressing Myo10MD (yellow) and CDHR2TM (magenta) and stained for endogenous fascin (cyan). Panel to the right shows inverted single channel image of fascin. Scale bar = 5 μm. (**C**) Confocal maximum intensity projection of HeLa cell expressing Myo10MD (green) and CDHR2TM (magenta) 2 min after rapalog addition. Scale bar = 10 μm. (**Ci**) Montage of zoomed in region (**C**) highlighting the growth of a single

filopodium (white arrow). (**D**) Elongation rate of single filopodium induced by rapalog treatment. Rate was calculated via the slope using a simple linear regression; *n* = 14 individual filopodia from *n* = 3 separate cells. (**E**) SIM maximum intensity projection image of a HeLa cell expressing full-length Myosin-10 (green) and stained for endogenous VASP (magenta) and F-actin with phalloidin (cyan). Zoom images to the right show merge and inverted single channel images. Yellow circles denote the tips of individual filopodia. (**F**) Line scans parallel to the filopodial axis show the intensity distribution of VASP in filopodia generated from over-expressing EGFP-myosin-10 full length; *n* = 30 protrusions, line represents the average intensity. (**G**) SIM maximum intensity projection image of a HeLa cell expressing Myo10MD (green) and CDHR2TM (not shown) 25 min after rapalog treatment and stained for endogenous VASP (magenta) and F-actin (cyan). Zoom images to the right show merge and inverted single channel images. Yellow circles denote the tips of individual filopodia. For **E** and **G**, scale bar = 5 μm, zoom scale bar = 2 μm. (**H**) Line scans parallel to the filopodial axis show the intensity distribution of VASP in filopodia; *n* = 39 filopodia, line represents the average intensity. (**I**) Confocal maximum intensity projection of HeLa cells transfected with either non-targeting siRNA (scramble KD) or siRNA targeting mDia1 (mDia1 KD) and expressing Myo10MD (green) and CDHR2TM (magenta), imaged 25 min after rapalog treatment. Scale bars = 10 μm. (**J**) Percent of cells displaying filopodial elongation with or without KD of mDia1; *n* = 3 replicates with 87-93% knockdown efficiency. Double transfected cells/condition scramble KD (*n* = 184) and mDia1 KD (*n* = 63). Ns, p-value > 0.05 calculated using the unpaired Student's t-test; all graph error bars represent the mean ± SD.

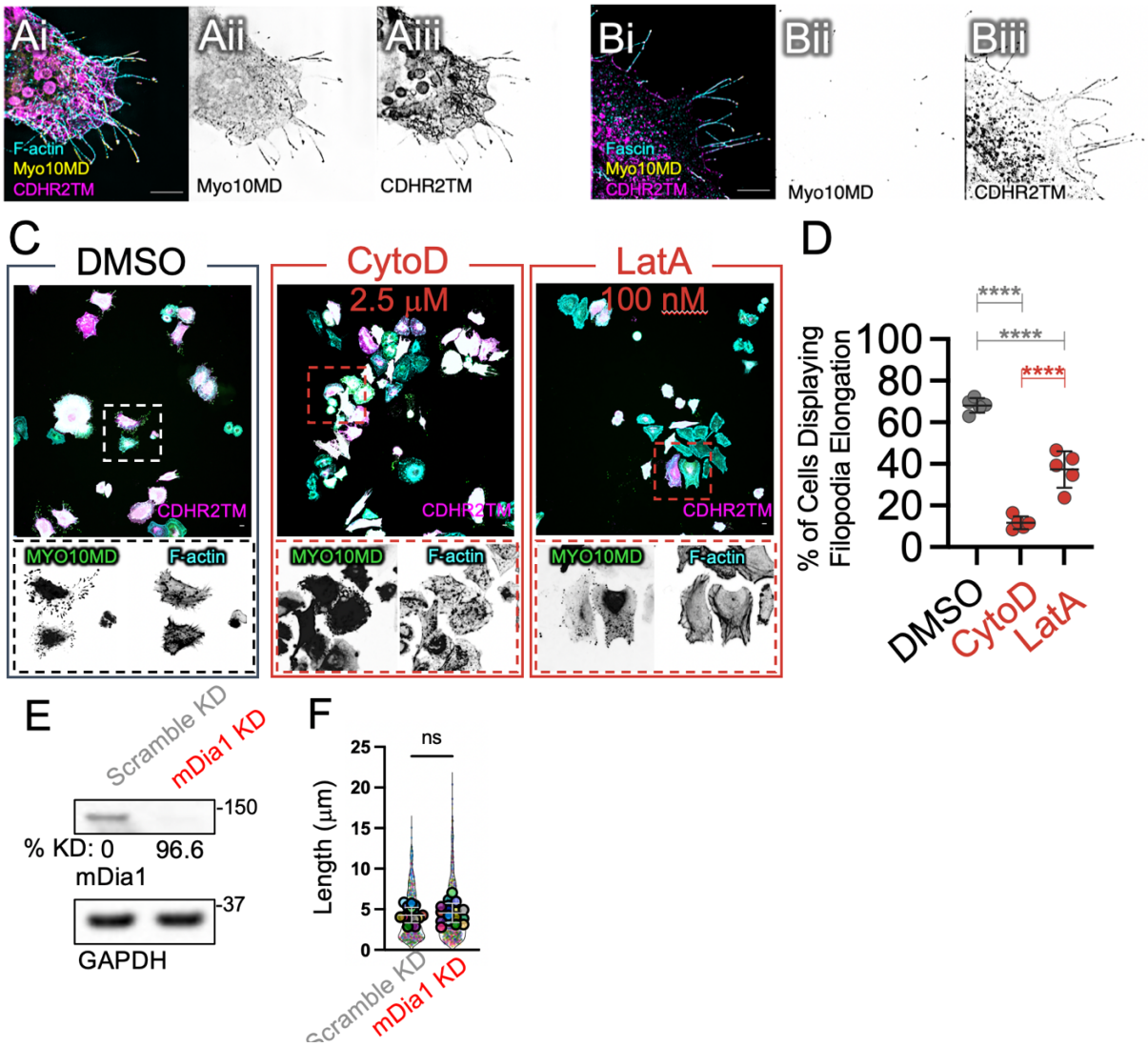

Supp Figure 3-2, related to Figure 3-2: Filopodia induced by membrane bound Myo10MD requires polymerizing actin, and are not impacted by DIAPH1 (mDia1) KD. Inverted single channel SIM image of Myo10MD (Aii and Bii) and CDHR2TM (Aiii and Biii) to confirm expression of these constructs shown in Fig 2A and 2B. Scale bar = 5 μm. (**C**) Merged confocal maximum intensity projection of HeLa cells expressing the Myo10MD (green) and CDHR2TM (magenta) constructs 25 min after rapalog treatment and either DMSO (control), 2.5 μM Cytochalasin D (CytoD), or 100 nM Latrunculin A (LatA). Scale bar = 10 μm. (**D**) Quantification of the percentage of cells displaying filopodia elongation after treatment with rapalog and either DMSO, CytoD, or LatA; n = > 370 cells for each treatment; error bars represent the mean ± SD; ****p-value ≤ 0.0001 was calculated using an Ordinary one-way ANOVA followed by Tukey's multiple comparisons test to compare treatments with each other. (**E**) Representative western blot analysis of expression levels of mDia1 in lysates from HeLa cells siRNA scramble control (Scramble KD) and siRNA mDia1 KD (mDia1 KD). GAPDH was used as a loading control. Percent KD below mDia1 expression blot based on densitometry measurements normalized to GAPDH.

of force, might drive faster elongation rates and/or longer protrusions. While the absolute amount of force generated by Myo10MD in cells is experimentally inaccessible, we reasoned that we could obtain a relative measure of force by monitoring the EGFP intensity from the Myo10MD construct; this signal is proportional to the number of Myo10MD motors and thus local force-generating potential. Using live-cell SDC imaging, we monitored Myo10MD tip intensity during individual filopodial growth events after inducing HeLa cells with rapalog. Because filopodia generated in these experiments are highly dynamic and poorly anchored to the coverslip substrate, culture media was supplemented with 0.5% methylcellulose; this prevented lateral waving of protrusions and improved our ability to monitor the details of elongation with high temporal resolution. Importantly, the addition of methylcellulose did not alter the growth rates of filopodia induced by membrane-bound Myo10MD (**Supp Fig 3-3**). Using this approach, we measured the distal tip intensity of Myo10MD in parallel with filopodial length from time-lapse data collected at 2 sec intervals (**Fig 3-3A**). This analysis revealed a striking and direct temporal correlation between the length of a growing filopodium and the accumulation of Myo10MD at its distal tip (**Fig 3-3B**). Thus, during growth, filopodial length is well correlated to the force-generating potential of tip-enriched myosin motors.

To place these findings into context and determine how the distal tip enrichment of Myo10MD compares to wild type full-length Myo10 (Myo10FL), we repeated these experiments in HeLa cells expressing EGFP-Myo10FL and scored tip intensities and lengths from filopodia. This analysis revealed that the tip intensity vs. length distributions obtained for Myo10MD and Myo10FL largely overlapped (**Fig 3-3C**). Moreover, filopodia generated by both constructs had similar morphology when matched in length and

intensity (**Fig 3-3D - circled data points in 3-3C**). Together these data indicate that, during filopodial elongation, the tip enrichment and thus force-generating potential of membrane-bound Myo10MD is comparable to Myo10FL.

Active, barbed end-directed force is required for filopodial induction.

The observation that filopodial length increases in parallel with distal tip accumulation of membrane-bound Myo10MD is consistent with the proposal that force generated by this motor directly promotes protrusion growth. From this perspective, we next examined whether the mechanical activity of Myo10MD is required for filopodia elongation. We generated two additional Myo10MD constructs containing mutations in switch I (R220A) or switch II (G437A) that are expected to disrupt force generation (Sasaki and Sutoh, 1998). Docking the motor-dead G437A construct (EGFP-Myo10MDx-FRB, herein referred to as Myo10MDx) (**Fig 3-3E**) to the plasma membrane with rapalog treatment failed to elongate filopodia (**Fig 3-3Fi-ii, 3-3H, 3-3I**). A motor-dead R220A Myo10MD mutant also failed to accumulate in filopodia, most likely because of its impaired actin binding (**Supp Fig 3-3**). Based on these data, we conclude that active, force-generating motors are needed to drive filopodial elongation in response to rapalog treatment.

To determine if the induction of filopodial elongation specifically requires the application of barbed end-directed force to the plasma membrane, we generated a construct using the motor domain from myosin-6, the sole pointed end-directed member of the myosin superfamily (a.a. 1-844, EGFP-Myo6MD-FRB, herein referred to as Myo6MD) (**Fig 3-3E**). Membrane-bound Myo6MD also failed to promote filopodial

elongation in response to rapalog treatment (**Fig 3-3Gi-ii, 3-3H, 33-J**). Taken together, these data indicate that the application of barbed end-directed force by membrane-bound motors is needed for robust filopodia elongation.

Filopodial growth induced by membrane-bound Myo10MD is limited by the availability of actin monomers and plasma membrane.

Why the robust filopodial growth induced by membrane-bound Myo10MD stalls at long lengths remains unclear. One possibility is that protrusions become so long that the pool of free actin monomers available for incorporation at the distal barbed ends falls below the level needed to continue elongation. To test this possibility, HeLa cells were subjected to long-term G-actin sequestration with a low concentration of Latrunculin A (Lat A). Based on the reversible nature of Lat A treatment (Spector et al., 1983), our rationale was that washing out Lat A post- rapalog treatment would rapidly and acutely increase the pool of free actin monomers; any “reactivation” of filopodial growth at that point would indicate that the availability of free G-actin normally limits elongation. For these experiments, HeLa cells were incubated in 100 nM Lat A for 7 days, to allow for long-term adaption prior to transfection with Myo10MD and CDHR2TM (**Fig 3-4A**). When we examined how individual cells responded to Lat A washout, we noted a significant increase in filopodia length sum following rapalog treatment (**Fig 3-4B-D, compare blue and gray lines at 75 min**). These results suggest that the actin monomer pool does become limiting, and that the sustained elongation of protrusions induced by membrane-bound Myo10MD may be at least partially dependent on available monomers.

Filopodial growth after rapalog induction might also be limited by the availability of

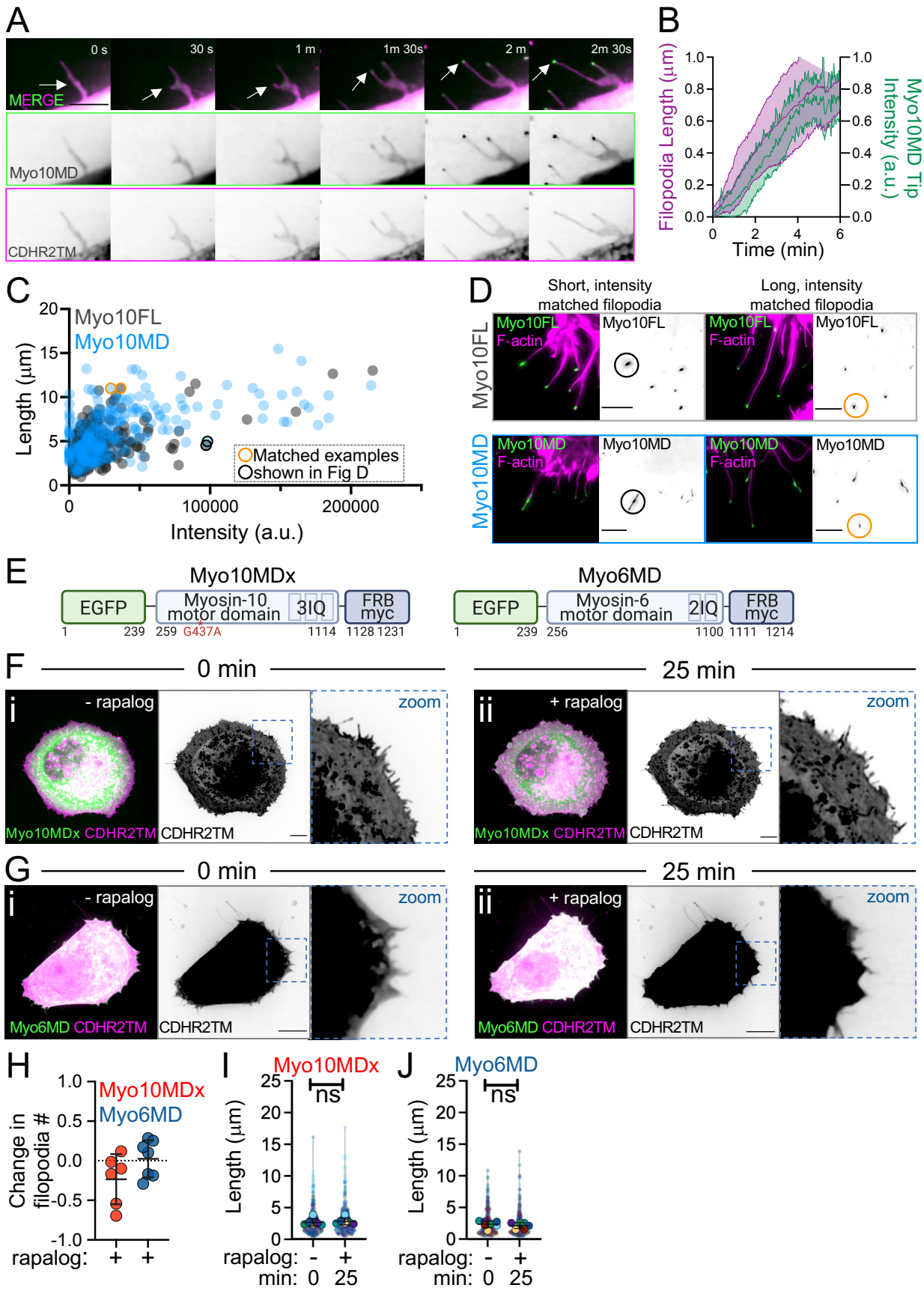
A
0 s
30 s
1 m
1m 30s
2 m
2m 30s
MERGE
Myo10MD
CDHR2TM
B
Filopodia Length (µm)
Myo10MD Tip Intensity (a.u.)
Time (min)
C
Myo10FL
Myo10MD
Length (µm)
Intensity (a.u.)
Matched examples
shown in Fig D
D
Short, intensity matched filopodia
Long, intensity matched filopodia
Myo10FL
Myo10MD
F-actin
E
Myo10MDx
Myo6MD
EGFP
Myosin-10 motor domain
3IQ
FRB myc
Myosin-6 motor domain
2IQ
G437A
F
0 min
25 min
i
ii
- rapalog
+ rapalog
zoom
Myo10MDx CDHR2TM
CDHR2TM
G
Myo6MD CDHR2TM
H
Change in filopodia #
rapalog:
I
J
ns
min:

Figure 3-3*:* Barbed end-directed force is required for filopodial induction by Myo10MD*.* (**A**) Montage of a filopodial growth event from a HeLa cell expressing Myo10MD (green) and CDHR2TM (magenta) imaged in 0.5% methylcellulose. Arrows denote the tip of a single, growing filopodium. Scale bar = 5 μm. (**B**) Normalized length (magenta) and tip intensity (green) vs. time curves for individual filopodia on cells expressing Myo10MD and CDHR2TM; *n* = 10 filopodia. (**C**) Filopodial length and myosin distal tip-intensity from individual protrusions in cells expressing Myo10FL (gray) or Myo10MD (blue); each circle represents an individual filopodium. Orange and black circled data points represent filopodia shown in **D**; *n* = 304 filopodia for Myo10FL and 273 for Myo10MD. (**D**) Confocal maximum intensity projections of length and tip intensity-matched filopodia in cells expressing Myo10FL or Myo10MD (green) and stained for F-actin with phalloidin (magenta); single inverted channel images are shown to the right. Scale bar = 5 μm. (**E**) Cartoons depicting the myosin-10 motor domain dead G437A mutant (Myo10MDx) and pointed end-directed myosin-6 motor domain (Myo6MD) constructs; numbers below represent amino acids. (**F**) Confocal maximum intensity projection of HeLa cells expressing Myo10MDx (green) and CDHR2TM (magenta) before (**i**) and 25 min after (**ii**) rapalog treatment. (**G**) Confocal maximum intensity projection of HeLa cells expressing Myo6MD (green) and CDHR2TM (magenta) before (**i**) and 25 min after (**ii**) rapalog treatment. For **F** and **G**, scale bar = 10 μm. (**H**) Fractional change in filopodia number in HeLa cells expressing CDHR2TM and Myo10MDx (red) or Myo6MD (blue) 0 min and 25 min after rapalog treatment; *n* = 6-7 individual cells for each condition. (**I**) Filopodial length measured at 0 min and 25 min post rapalog treatment in HeLa cells expressing Myo10MDx and CDHR2TM; *n* = 6 individual cells, *n* = > 420 individual protrusions. (**J**) Filopodial length measured at 0 min and 25 min post rapalog treatment in HeLa cells expressing Myo6MD and CDHR2TM; *n* = 7 individual cells, *n* = > 365 individual protrusions. Data in (**I**) and (**J**) are represented as a SuperPlot, where transparent circles represent the length of individual filopodia, opaque circles represent the average length of filopodia from individual cells, violin plots show the distribution of the data, and all color-matched circles represent measurements from the same cell. All graph error bars represent the mean ± SD; ns, p-value > 0.05.

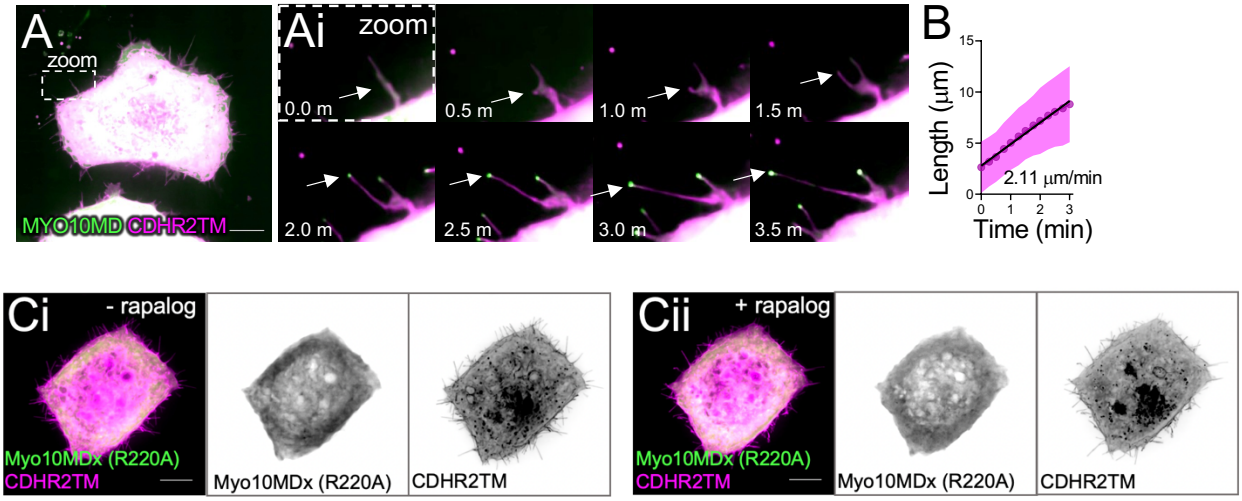

Supp Figure 3-3, related to Figure 3: Methylcellulose does not alter the growth rates of filopodia induced by membrane bound Myo10MD, and the myosin-10 motor domain switch I dead (R220A) construct does not elongate filopodia. (**A**) Merged confocal maximum intensity projection of HeLa cell expressing Myo10MD (green) and CDHR2TM (magenta) after the addition of rapalog. Scale bar = 10 μm. (**Ai**) Montage of zoomed in region (**A**) highlighting the growth of a single filopodium (white arrow). (**B**) Quantification of the elongation rate of single filopodium induced by rapalog treatment in media containing 0.5% methylcellulose. Rate was calculated via the slope using a simple linear regression; *n* = 15 individual filopodia from n = 3 separate cells. Error bars represent the SD. Merged confocal maximum intensity projection of HeLa expressing Myo10MD-R220A (green) and CDHR2TM (magenta) at 0 min (**Ci**) and 25 min after (**Cii**) rapalog treatment. Inverted single channel images shown to the right of the merged. Scale bar = 10 μm.

encapsulating plasma membrane lipids. To test this idea, we added the fluorescent bilayer intercalating compound CellMask-Orange (herein referred to as CellMask) to cells 35 min after filopodial elongation was initiated with rapalog treatment (**Fig 3-4E**). Based on biophysical studies, such compounds are expected to increase membrane surface area while reducing membrane tension (Raucher and Sheetz, 1999a; Raucher and Sheetz, 1999b; Raucher and Sheetz, 2000a). Interestingly, CellMask addition induced a significant second stage of elongation beyond the initial response driven by membrane-bound Myo10MD (**Fig 3-4F and 3-4G, compare magenta and gray lines at 140 min**), which resulted in a significant increase in filopodia length sum (**Fig 3-4H**). Thus, in addition to being limited by the availability of actin monomers, sustained filopodial growth driven by membrane-bound Myo10MD may also be limited by the availability of encapsulating plasma membrane.

Myosin motor domains from structurally diverse superfamily classes also support rapalog-induced filopodial growth.

Myosin superfamily members exhibit a range of mechanochemical properties, which enable these motors to perform specific subcellular tasks that hold unique kinetic requirements (e.g., cargo anchoring vs. transport). Therefore, we next sought to determine if the robust filopodial elongation driven by Myo10MD is unique to this motor, or could instead be supported by other myosins typically found in other actin-based protrusions, such as microvilli and stereocilia. To test this, we generated additional constructs based on protrusion-resident barbed end-directed myosins that exhibit a range of mechanochemical properties including myosin-1a, myosin-5b (lever arm with 6 IQ

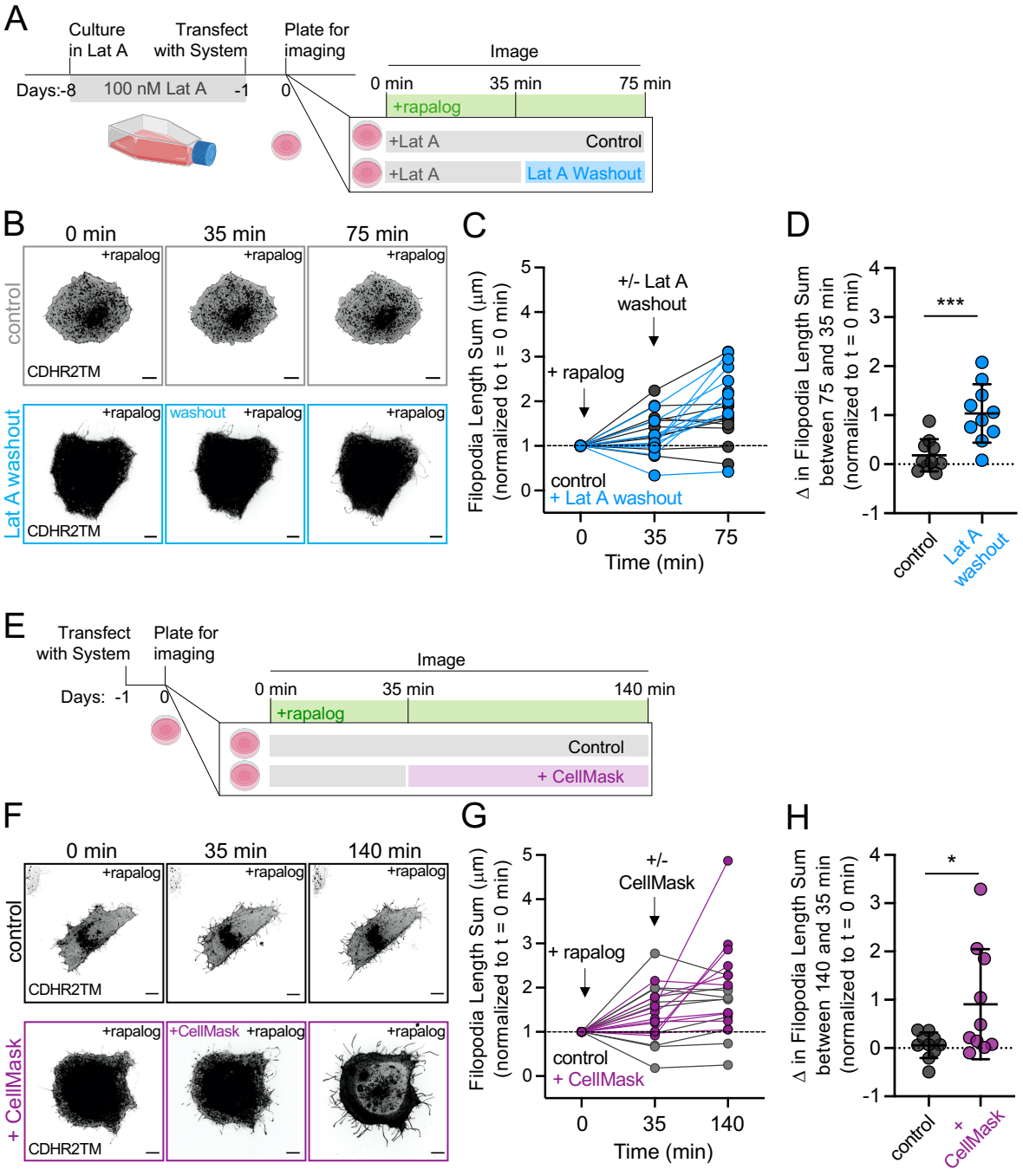

Figure 3-4: Myo10MD induced filopodial growth depends on membrane and G-actin availability.(**A**) Cartoon of the Latrunculin A (Lat A) washout experimental timeline. (**B**) Confocal maximum intensity projection of representative HeLa cells expressing Myo10MD (not shown) and CDHR2TM (gray scale), treated with 100 nM Lat A for one week (top; control) or Lat A for one week followed by washout (bottom). (**C**) Normalized length sum of filopodia generated over time in cells treated with Lat A (gray) or treated with Lat A followed by washout (blue). (**D**) Change in filopodial length sum between the 75 and 35 min time points for cells treated with Lat A (gray)

or treated with Lat A followed by washout (blue). (**E**) Cartoon of membrane expansion experimental timeline. (**F**) Confocal maximum intensity projection of representative HeLa cells expressing Myo10MD (not shown) and CDHR2TM (gray scale). Untreated control cell (top) and cell treated with membrane intercalating CellMask for 35 min (bottom). (**G**) Normalized length sum of filopodia generated over time in control HeLa cells (gray) or cells treated with CellMask (magenta). (**H**) Change in filopodial length sum between the 140 and 35 min time points for cells treated without (gray) or treated with CellMask (magenta). All graph error bars represent the mean ± SD; * p-value ≤ 0.05, **** p-value ≤ 0.0001. P-values were calculated using unpaired Student's t-tests comparing treatments at the indicated time point, *n* = 10 individual cells for each of the four treatments. Scale bars = 10 μm.

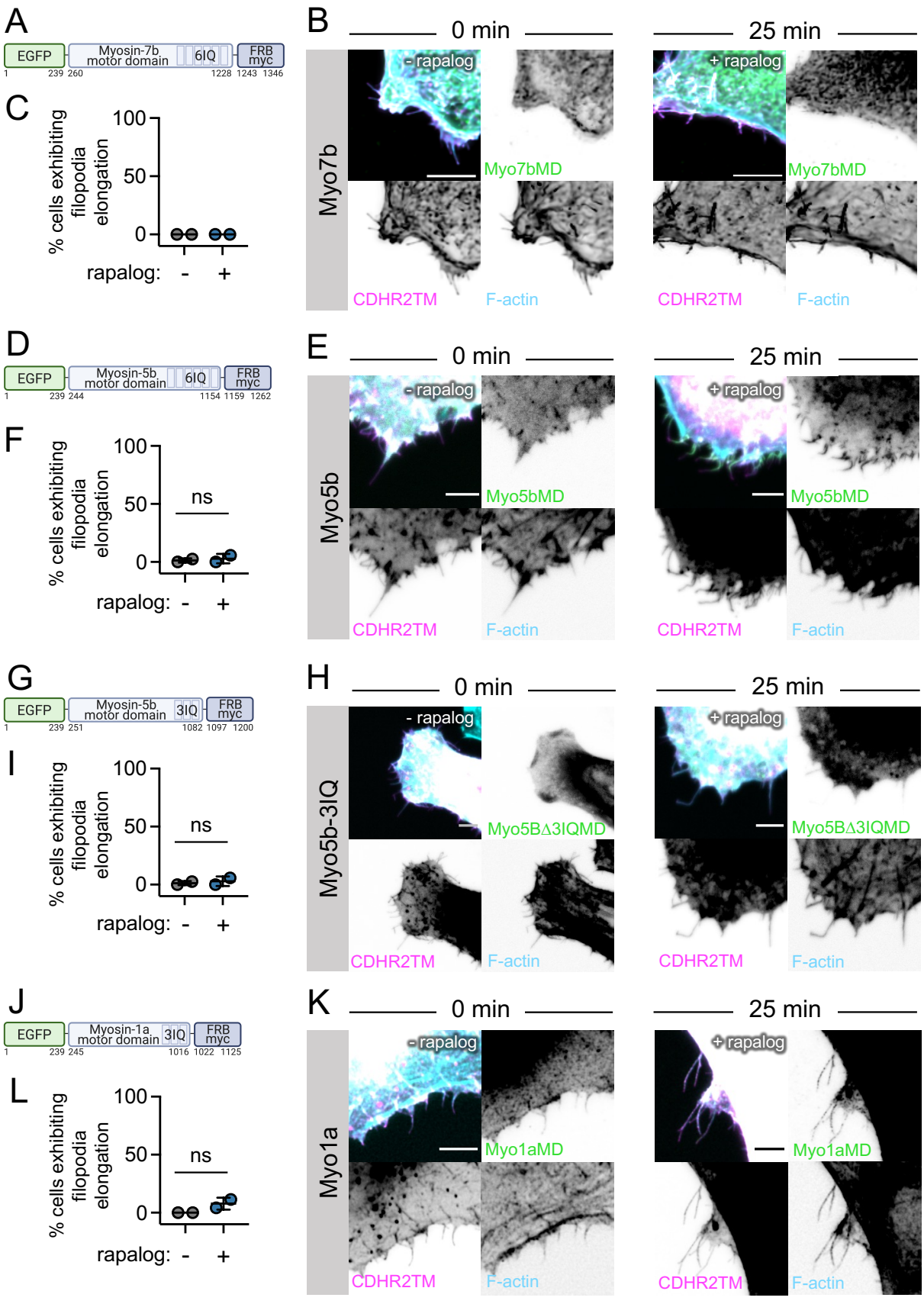
A
EGFP
Myosin-7b motor domain
6IQ
FRB myc
1 239 260 1228 1243 1346
B
0 min
25 min
- rapalog
+ rapalog
Myo7b
Myo7bMD
CDHR2TM
F-actin
C
% cells exhibiting filopodia elongation
100
50
0
rapalog: - +
D
EGFP
Myosin-5b motor domain
6IQ
FRB myc
1 239 244 1154 1159 1262
E
Myo5b
Myo5bMD
F
ns
G
EGFP
Myosin-5b motor domain
3IQ
FRB myc
1 239 251 1082 1097 1200
H
Myo5b-3IQ
Myo5BΔ3IQMD
I
J
EGFP
Myosin-1a motor domain
3IQ
FRB myc
1 239 245 1016 1022 1125
K
Myo1a
Myo1aMD
L

Supp Figure 3-5, related to Figure 5: Myosin-7b, -5b, -5bΔ3IQ and -1a motor domains do not elongate filopodia. (**A**) Cartoon diagram showing the EGFP-Myosin-7b Motor Domain (Myo7bMD)-FRB-myc construct. (**B**) Merged confocal maximum intensity projection of HeLa cells expressing Myo7bMD (green) and CDHR2TM (magenta) at 0 min and 25 min after rapalog treatment. (**C**) Quantification of the percentage of cells displaying filopodia elongation without and after treatment with rapalog. (**D**) Cartoon diagram showing the EGFP-Myosin-5b Motor Domain (Myo5bMD)-FRB-myc construct. (**E**) Merged confocal maximum intensity projection of HeLa cells expressing Myo5bMD (green) and CDHR2TM (magenta) at 0 min and 25 min after rapalog treatment. (**F**) Quantification of the percentage of cells displaying filopodia elongation without and after treatment with rapalog. (**G**) Cartoon diagram showing the EGFP-Myosin-5b Motor Domain with 3 IQ domains deleted (Myo5bdel3IQMD)-FRB-myc construct. (**H**) Merged confocal maximum intensity projection of HeLa cells expressing Myo5bdel3IQMD (green) and CDHR2TM (magenta) at 0 min and 25 min after rapalog treatment. (**I**) Quantification of the percentage of cells displaying filopodia elongation without and after treatment with rapalog. (**J**) Cartoon diagram showing the EGFP-Myosin-1a Motor Domain (Myo1aMD)-FRB-myc construct. (**K**) Merged confocal maximum intensity projection of HeLa cells expressing Myo1aMD (green) and CDHR2TM (magenta) at 0 min and 25 min after rapalog treatment. (**L**) Quantification of the percentage of cells displaying filopodia elongation without and after treatment with rapalog. Inverted single channel images shown to the right and below of the merged. All images were also stained for F-actin (cyan). Scale bar = 5 μm; n = > 57 cells for each treatment from two biological repeats; error bars represent the mean ± SD; ns p-value > 0.05 was calculated using a Student's t-test.

motifs (-wildtype) or 3 IQ motifs (-5b3IQ)), myosin-7b, myosin-3a, and myosin-15a. By surveying fixed and stained samples after induction, we noted that the motor domains of myosin-1a, -5b-wildtype, -5b3IQ, and -7b were unable to elongate filopodia when docked when docked onto the plasma membrane (**Supp Fig 3-4**). In contrast, motor domains from the stereocilia tip-targeting motors, myosin-3a (a.a. 407-1432, EGFP-Myo3aΔKMD-FRB, herein referred to as Myo3aΔKMD; **Fig 3-5A**) and myosin-15a (a.a. 1-750, EGFP-Myo15aMD-FRB, herein referred to as Myo15aMD; **Fig 3-5F**) drove significant elongation following rapalog induction (**Fig 3-5Bi, 3-5Bii, 3-5Gi, 3-5Gii**). Quantification of the length sum of filopodia over time showed that there was a significant increase generated by both motors after 20 and 10 minutes of rapalog treatment, respectively (**Fig 3-5C, 3-5H**). Like the Myo10MD construct, docking either the Myo3aΔKMD or Myo15aMD constructs to the membrane did not significantly change the number of filopodia generated post-rapalog treatment (**Fig 3-5D, 3-5I**), but did increase filopodial length (**Fig 3-5E, 3-5J**). These results indicate that the robust filopodial elongation observed following rapalog induction is not unique to Myo10MD and can also driven by other structurally diverse myosins that reside in distinct protrusion environments.

Myo10MD driven filopodial elongation is supported by diverse membrane binding motifs

Our data show that docking the Myo10MD on the plasma membrane using the single-spanning CDHR2TM leads to robust filopodial elongation. In addition to binding transmembrane proteins, some myosin tail domains interact directly with the plasma

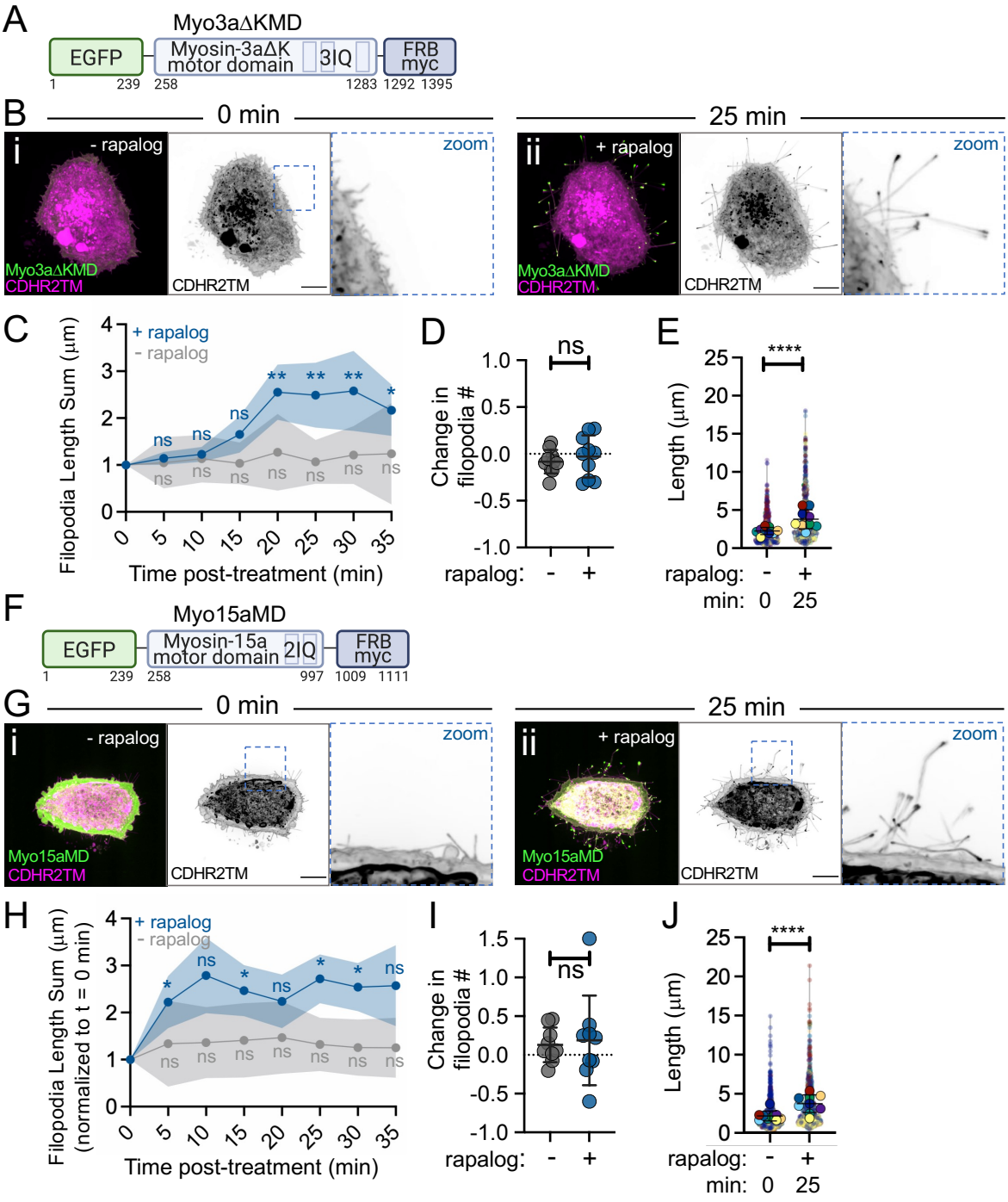

Figure 3-5: Motor domains from Myo3a and Myo15a also promote filopodia growth. (**A**) Cartoon depicting the EGFP-Myo3aΔK motor domain-FRB-myc construct (Myo3aΔKMD); numbers below represent amino acids. (**B**) Confocal maximum intensity projection image of control HeLa cells expressing the Myo3aΔKMD (green) and CDHR2TM (magenta) at 0 min (**i**) and 25 min after (**ii**) rapalog treatment. (**C**) Length sum of filopodia over time in untreated (gray line) or rapalog-treated (blue line) HeLa cells expressing Myo3aΔKMD and CDHR2TM; *n* = 14-16 cells per treatment. (**D**) Fractional change in filopodia number from 0 min to 25

min in untreated (gray) or rapalog treated (blue) HeLa cells expressing Myo3aΔKMD and CDHR2TM; *n* = 10 cells per condition. (**E**) Filopodia length at 0 and 25 min post rapalog treatment in HeLa cells expressing Myo3aΔKMD and CDHR2TM; *n* = 9 cells, *n* = > 670 protrusions. (**F**) Cartoon depicting the EGFP-Myosin-15a motor domain-FRB-myc construct (Myo15aMD); numbers below represent amino acids. (**G**) Confocal maximum intensity projection images of control HeLa cells expressing Myo15aMD (green) and CDHR2TM (magenta) before (**i**) and 25 min after (**ii**) rapalog treatment. (**H**) Length sum of filopodia over time in untreated (gray line) or rapalog treated (blue line) HeLa cells expressing Myo15aMD and CDHR2TM; *n* = 13-16 individual cells per treatment. (**I**) Fractional change in filopodial number from 0 to 25 min in untreated (gray) or rapalog treated (blue) HeLa cells expressing Myo15aMD and CDHR2TM; *n* = 9 cells per condition. (**J**) Filopodia length measured at 0 and 25 min post rapalog treatment in HeLa cells expressing Myo15aMD and CDHR2TM; *n* = 9 individual cells, *n* = > 730 protrusions. Data in (**E**) and (**J**) are represented as a SuperPlot, where transparent circles represent the length of individual filopodia, opaque circles represent the average length of protrusions of individual cells, violin plots show the distribution of the data, and all color matched circles represent measurements from the same cell. All graph error bars represent the mean ± SD; ns p-value > 0.05, * p-value ≤ 0.05, ** p-value ≤ 0.01, **** p-value ≤ 0.0001. Scale bars = 10 μm.

membrane. For example, the second PH domain in the myosin-10 tail interacts with the phosphoinositol species, $PI(3,4,5)P_3$, which is found in the plasma membrane along the filopodia shaft, and the TH1 domain of myosin-1a interacts with the acidic phospholipids found in the inner leaflet of the plasma membrane. To determine if these peripheral modes of membrane binding support filopodial elongation, we generated two additional membrane docking constructs by fusing FKBP to: (1) the PH domain of Bruton's tyrosine kinase (BTK), which binds $PI(3,4,5)P_3$ (Fukuda et al., 1996; Salim et al., 1996) (BTK-PH-mCherry-FKBP, herein referred to as BTK-PH, **Fig 3-6D**), and (2) TH1 domain of myosin-1a, which binds electrostatically to the inner leaflet of the plasma membrane (Mazerik and Tyska, 2012) (FKBP-mCherry-TH1, herein referred to as TH1; **Fig 3-6G**). Both constructs showed membrane enrichment as expected (**Fig 3-6B, 3-6E, 3-6H,** pre-bleach). Fluorescence recovery after photobleaching (FRAP) quantification of the turnover kinetics in each case also revealed distinct immobile fractions (I.F.) for each construct (**Fig 3-6C, 3-6F, 3-6I**). As predicted, the integral, transmembrane CDHR2TM construct (**Fig 3-6A**) had the largest I.F. compared to the two peripheral membrane-interacting constructs (compare 6C to 6F and 6I). To determine if these different membrane binding motifs could support filopodial elongation, we turned to a fixed-cell approach, where HeLa cells were transfected with either of the three membrane constructs and the Myo10MD construct and induced to produce filopodia with the addition of rapalog. This analysis showed that all three modes of membrane interactions were able to support filopodia elongation (**Fig 3-6J, 3-6K, 3-6L**), with the CDHR2TM producing the most robust response (**Fig 3-6M**). These results further suggest that the ability of myosin motor

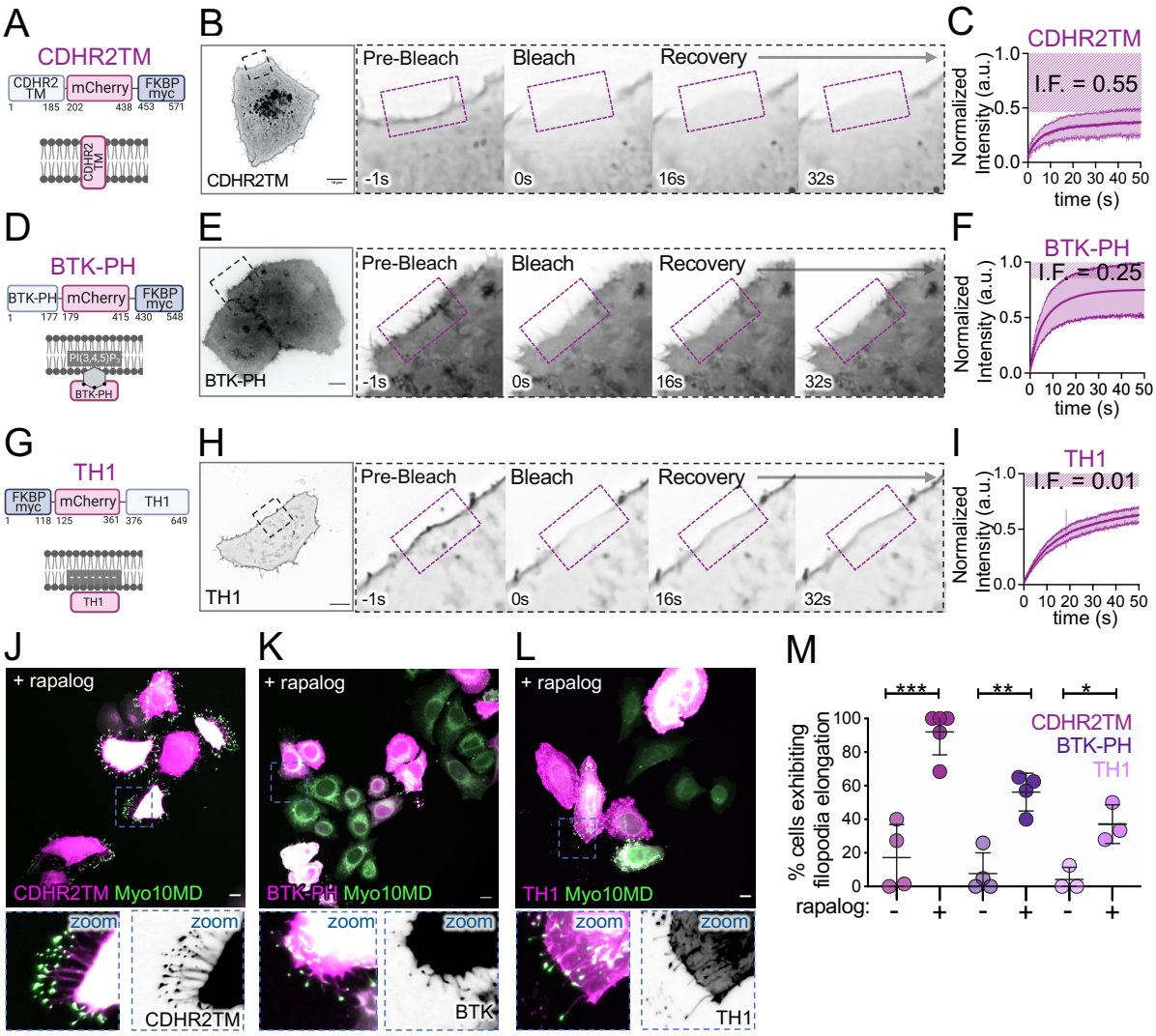

Figure 3-6: Myo10MD driven filopodial elongation is supported by diverse membrane binding motifs. (**A**) Cartoon depicting the integral transmembrane construct CDHR2TM-mCherry-FKBP construct. (**B**) Confocal maximum intensity projection timelapse montage showing fluorescence recovery after photobleaching (FRAP) analysis of a HeLa cell expressing CDHR2TM. (C) FRAP recovery curve; measurements were taken from ROI shown in B; *n* = 6 cells; magenta striped region indicates the immobile fraction. (**D**) Cartoon showing organization of the peripheral membrane binding construct BTK-PH-mCherry-FKBP (BTK-PH). (**E**) Confocal maximum intensity projection timelapse montage showing FRAP analysis of a HeLa cell expressing BTK-PH. (**F**) FRAP recovery curve; measurements were taken from the ROI shown in E; *n* = 9 cells; magenta striped region indicates the immobile fraction. (**G**) Cartoon depicting the peripheral membrane binding construct FKBP-mCherry-TH1 (TH1). (**H**) Confocal maximum intensity projection timelapse montage showing FRAP analysis of a HeLa cell expressing TH1. (I) FRAP recovery curve; measurements were taken from the ROI shown in H; *n* = 8 cells; magenta striped region indicates the immobile fraction. (**J**) Confocal maximum intensity projection image of HeLa cells expressing Myo10MD (green) and CDHR2TM (magenta) 25 min

after rapalog treatment. (**K**) Confocal maximum intensity projection image of HeLa cells expressing Myo10MD (green) and BTK-PH (magenta) 25 min after rapalog treatment. (**L**) Confocal maximum intensity projection image of HeLa cells expressing Myo10MD (green) and TH1 (magenta) 25 min after rapalog treatment. (**M**) Percentage of untreated or rapalog-treated HeLa cells expressing Myo10MD and CDHR2TM, BTK-PH, or TH1 exhibiting filopodia elongation; $n > 170$ cells for CDHR2TM, $n > 140$ cells for BTK-PH, and $n > 220$ cells for TH1. All graph error bars represent the mean ± SD; * p-value ≤ 0.05, ** p-value ≤ 0.01, *** p-value ≤ 0.001. Scale bars = 10 μm.

domains to drive filopodia elongation is independent of the structural details of membrane association.

DISCUSSION

Cell surface protrusions are essential for mediating physical and biochemical interactions with the external environment. Throughout evolution, μm-scale finger-like protrusions have been adapted to fill a range of functional niches, including mechanosensation and solute transport (Revenu et al., 2004). Fundamental to the formation of a surface protrusion is the outward deformation of the fluid plasma membrane. Estimates of the forces a cell must apply to form a protrusion come from optical trap-based measurements of the "tether force": the force required to pull and hold a thin tubule of membrane at a steady-state length (Dai and Sheetz, 1995; Sheetz, 2001). Although tether forces are measured by externally imposed mechanical perturbations, they offer an approximation of the physical challenge that the cytoskeletal machinery faces during protrusion formation and suggest that pN-scale pushing force is needed. A long history of previous theoretical and experimental studies have argued that actin polymerization generates this force during protrusion growth (Condeelis, 1993; Hill and Kirschner, 1982a; Pollard and Borisy, 2003). Indeed, the incorporation of new actin subunits into the growing barbed ends of actin filaments generates force in the required pN-scale range (Kovar and Pollard, 2004b). Because protrusions are supported by 10s to 100s of parallel filament bundles, these structures should be able to generate outward pushing force that exceeds the threshold suggested by tether force estimates. However, the ability of a growing actin filament to generate force also depends on the availability of

free actin monomers (Theriot, 2000). This poses a mechanistic conundrum given the tight confines of the intrafilopodial cytoplasm, where the diffusive availability of new monomers at growing barbed ends could become limiting as a protrusion elongates. From this perspective, we set out to test the hypothesis that myosin motors, which are abundant residents of varying actin-based protrusions, provide an additional source of mechanical force for driving protrusion growth.

Based on their mechanical potential and localization at the interface between polymerizing actin filaments and cellular membranes, myosins are well-positioned to drive membrane deformation in diverse biological contexts. Driving the growth of surface membrane protrusions is a long-standing functional hypothesis proposed for several unconventional members of the myosin superfamily, including motors from classes 1, 3, 5, 7, 10, and 15 (Houdusse and Titus, 2021). Previous cell biological studies have emphasized cargo transport models, which propose that protrusion myosins deliver specific factors to the distal tip compartment, and these in turn promote growth via a range of molecular mechanisms. We now know that myosins in microvilli, filopodia, and stereocilia are critical for the distal tip enrichment of scaffolding proteins (Crawley et al., 2014; Crawley et al., 2016; Grati and Kachar, 2011; Li et al., 2017), adhesion molecules (Weck et al., 2016; Yu et al., 2017), and proteins that directly impact actin dynamics and organization (Arthur et al., 2021; Ebrahim et al., 2016; Manor et al., 2011; Tokuo and Ikebe, 2004a). However, understanding a given myosin's contributions to protrusion growth, in terms of tip-directed cargo delivery vs. more direct mechanical effects, has proved challenging largely because an experimental approach for isolating the impact of motor domain force generation in cells has remained elusive.

In this report, we describe an engineered cell-based system that enabled us to directly test whether myosin generated force contributes to protrusion elongation. Using Myo10 as a model myosin, we found that—independent of any cargo binding potential—Myo10 motor domains drive robust filopodial growth when docked onto the plasma membrane using the rapalog-based system described here. Leveraging this approach to develop further insight into the properties of induced filopodial growth, we learned that elongation requires active motor domains that exert barbed end-directed force. Moreover, the elongation of individual protrusions was paralleled by an accumulation of Myo10 motor domains at filopodial tips, strongly suggesting that the local level of force application to the membrane controls filopodial growth kinetics. Importantly, induced filopodial elongation was supported by structurally distinct myosin motors, and membrane binding modules that associate with the plasma membrane using different mechanisms (transmembrane vs. peripheral). We, therefore, propose that the motor-driven filopodial growth revealed in our studies likely reflects a general activity of different unconventional myosins in diverse actin-based protrusions.

Why does docking myosin motor domains onto the plasma membrane drive such robust filopodial growth? We propose that motor domains impart barbed end-directed force directly onto the membrane that encapsulates a growing filopodium, and this, in turn, reduces the physical barrier to elongation. One possibility is that myosin-generated force “softens” the membrane (i.e. lowers membrane tension) in the distal tip compartment, allowing actin monomers to incorporate into the barbed ends of core bundle filaments more readily (**Fig 3-7**) Consistent with this idea, we found that addition of a lipid intercalating probe, which is expected to expand bilayer surface area and reduce

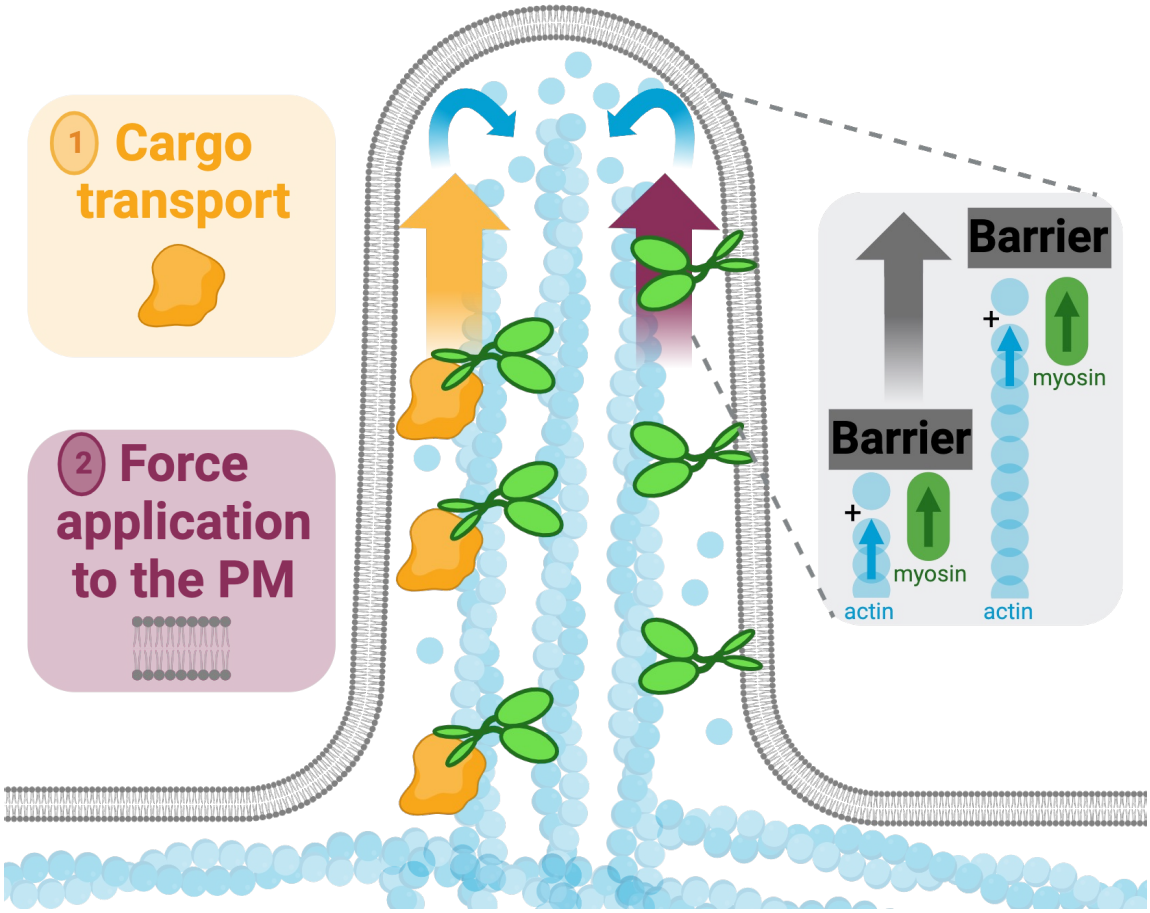

Figure 3-7: Model for the contribution of myosin-generated force in protrusion growth. Our studies reveal that, in addition to (1) delivering cargoes that promote protrusion growth or stability, barbed end directed force exerted by membrane bound myosins can also promote protrusion growth. Force application by myosin likely serves in parallel with force generated by the barbed-ends of elongating core bundle filaments, to displace the physical barrier posed by the plasma membrane.

membrane tension (Raucher and Sheetz, 2000b), immediately led to additional filopodial elongation. This concept is also supported by theoretical work (Orly et al., 2014) and biophysical studies showing that application of external force to the tip of a filopodium accelerates actin incorporation at the distal end (Bornschlogl and Bassereau, 2013). A second possibility is that force generated by membrane-bound motor domains contributes directly to the retrograde displacement of the actin core bundle; this again would be expected to reduce the barrier to actin monomer incorporation at the distal ends.

This latter idea finds support in previous studies on actin treadmilling dynamics in neuronal growth cone filopodia and epithelial microvilli (Chinowsky et al., 2020; Medeiros et al., 2006). A third possibility emerges from recent studies on MYO15A, which revealed a potential for the motor domain to bridge actin monomers and in turn, enhance actin polymerization (Gong et al., 2022; Moreland et al., 2021).

One open question that re-emerges here is whether a myosin motor can impart mechanical force to a fluid lipid bilayer. *In vitro* studies have shown that membrane lipids are generally free to diffuse through the plane of the bilayer, as indicated by relatively high diffusion coefficients (Sanderson, 2012). Based on this, one might expect that mechanical force imparted to proteins in the bilayer (e.g. CDHR2TM) or attached to the surface of the bilayer (e.g. TH1, BTK) would dissipate quickly. However, experimental evidence from more complex lipid mixtures that include cholesterol, indicate much lower rates of diffusion with significant frictional coefficients (Cicuta et al., 2007), leading to the possibility that external force applied by myosin motors may persist for a period of time. To be matched to the kinetics of motor domain attachment to actin, this duration only needs to be in the range of milliseconds (e.g. Myo10 exhibits a strongly bound duration

of ~80 ms)(Takagi et al., 2014). Moreover, filopodia contain 100s to 1000s of Myo10 molecules and because individual motors cycle asynchronously, the population will apply force continuously to the overlying plasma membrane. We, therefore, expect that protrusion resident myosins can exert biologically significant (pN scale) levels of force on the membrane for prolonged periods of time.

Of the numerous unconventional myosin motor domains tested for their ability to support filopodial elongation in this work, only representatives from classes 3, 10, and 15 were able to drive growth. Do these myosins share common features that explain this selectivity? One possible explanation might be linked to the biochemical composition of the core actin filament bundles that support filopodia. Fascin-1 is the dominant bundling protein in these structures and *in vitro* studies have revealed that the filopodial myosin, Myo10, preferentially interacts with and moves processively along actin filaments that are crosslinked in parallel by this bundler (Ropars et al., 2016; Takagi et al., 2014). Interestingly, as residents of stereocilia, Myo3 and Myo15 are adapted for interacting with core bundles organized by fascin-2 in addition to espin and plastin(Krey et al., 2016; Perrin et al., 2013; Sekerkova et al., 2006). Microvilli are structurally distinct from both filopodia and stereocilia in that their filaments are bundled by plastin, villin, espin and MISP (Bartles et al., 1998; Bretscher and Weber, 1979; Bretscher and Weber, 1980; Morales et al., 2022), but not fascin. Thus, a preference for the close filament spacing that is characteristic of fascin bundling might explain the robust filopodial elongation response demonstrated by the

motor domains of Myo3, Myo10, and Myo15, relative to other myosins tested in our assay.

Another possible explanation for why only a subset of myosins can induce filopodial elongation may be related to the natural diversity of kinetic properties exhibited by different motors. Myosins from different superfamily classes exhibit a broad range of actin filament sliding speeds and ATP hydrolysis kinetics (O'Connell et al., 2007). It follows that certain kinetic properties might be needed to support robust filopodial elongation in the assay we describe here. One might expect that, at a minimum, any motor capable of driving filopodial growth would need to demonstrate a barbed end-directed mechanical velocity faster than the actin retrograde flow rate. Velocities measured from sliding filaments assays or direct single-molecule observations indicate speeds for Myo3a, Myo10, and Myo15 in the range of 100s of nm/sec (110 nm/s, 310-660 nm/s, 278-429 nm/s, respectively)(Bird et al., 2014; Komaba et al., 2003; Ropars et al., 2016; Takagi et al., 2014), approximately 10-fold higher than typical retrograde flow rates (Bornschlogl et al., 2013). Thus, at least in the case of these three motors, this requirement appears to be met. Another kinetic property relevant here is the duty ratio: the fraction of the total ATPase cycle time that a motor domain will remain bound to actin. A high duty ratio myosin will be able to exert higher time-average force, which will increase its mechanical impact when present in a multi-motor ensemble (Bird et al., 2014; Dose et al., 2007; Homma and Ikebe, 2005).

Unconventional myosin isoforms have long been recognized as abundant components of actin-based protrusions. Whether these motors contribute growth-promoting force has remained unclear, primarily because of the technical challenges associated with uncoupling the roles of cargo transport from more direct mechanical effects. The data we report here indicates that myosins are also able to contribute

significant growth-promoting force to drive robust protrusion elongation. As one of the main limitations in studying surface protrusions is the stochastic nature of their assembly, we expect that the synthetic, inducible system introduced in this study will prove useful for biologists seeking to uncover a deeper understanding of the biochemical and biophysical nature of protrusion formation.

CHAPTER IV

MOLECULAR COUNTING OF MYOSIN FORCE GENERATORS IN GROWING FILOPODIA

ABSTRACT

Actin-based surface protrusions are defining features of animal cells that support a range of biological activities ranging from cell motility to mechanosensation to solute uptake. Long-standing models of protrusion growth suggest that actin filament assembly provides the primary mechanical force for “pushing” the plasma membrane outward. Expanding on these actin-centric models, our recent studies used a chemically inducible system to establish that plasma membrane-bound myosin motors, which are normally abundant in protrusions, can also power robust filopodial growth. How protrusion resident myosins supplement/coordinate with actin polymerization to drive elongation remains unclear, in part because the number of force generators and thus, the scale of their mechanical contribution remains undefined. To address this gap, we leveraged the SunTag system to count membrane-bound myosin motor domains in actively growing filopodia. Using this approach, we found that the number of myosins was log normally distributed with an average of 12.4 ± 2.20 myosin motors [GeoMean ± GeoSD]. Together with unitary force values derived from biophysical studies on single myosin molecules, and duty ratio estimates for the myosin motors used in these experiments, we calculate that a population of membrane-bound myosin motor domains can generate a time averaged force of 8.7 ± 1.5 pN [calculated with an average duty ratio of 0.7; GeoMean ± GeoSD] to elongate filopodia. Thus, myosin can generate a level of force that is

comparable to actin (~30 filaments per core bundle x ~1 pN per filament = 30 pN maximum force), a point that may constrain future physical models of protrusion growth.

INTRODUCTION

Filopodia are fingerlike, micron scale, membrane-wrapped protrusions that extend from the surface of diverse animal cell types. Structural support for these features is provided by a cytoskeletal core containing 10-30 actin filaments, which are cross-linked by the actin bundling protein, fascin (Svitkina et al., 2003; Vignjevic et al., 2006a) and uniformly oriented with their fast growing barbed-ends against the plasma membrane at the filopodial tip. In humans, filopodia are found in diverse physiological contexts, serving as cellular extensions through which cells can physically and biochemically interact with neighboring cells and their surrounding environment. Key cell functions that critically depend on filopodia include cell migration, cell steering, wound healing, in tissue contexts ranging from mesenchymal cells to neurons (Cavalier-Smith and Chao, 2003; Fierro-Gonzalez et al., 2013; Portera-Cailliau et al., 2003; Sebe-Pedros et al., 2013; Wood et al., 2002). Despite their widespread appearance on the surface of diverse cell types, important questions surrounding the physical basis of filopodial formation remain open.

Historically, filopodial formation models have been actin centric, as many studies have empirically determined the role and amount of force generated from actin polymerization. Further, as the growing, barbed ends of actin filaments are oriented against the membrane, filaments are in an ideal orientation to exert the required force needed to overcome the membrane tension to drive outward deformation of the plasma membrane (Footer et al., 2007a). Given the actin rich nature of filopodia and related structures, it makes biological sense that members of the myosin superfamily of actin-

based motors are abundant residents. Myosins characterized by MyTH4-FERM domains in their cargo binding tails offer specific examples, including myosin-10 (Myo10) in filopodia (Berg and Cheney, 2002), myosin-7B in microvilli (Weck et al., 2016), and myosin-15B in stereocilia (Belyantseva et al., 2003). Previous studies indicate that MyTH4-FERM myosins can use the core actin bundle as a track to drive tip ward transport of cargoes that are needed either for protrusion growth or long-term stability (Robert-Paganin et al., 2020). Myo10 is a highly studied example; as a processive motor that accumulates at filopodial tips, this motor delivers protein and cargoes that play important roles in filopodia formation, stability, and anchoring (Berg and Cheney, 2002; Kerber and Cheney, 2011; Sousa and Cheney, 2005). Early studies proposed that Myo10's ability to extend filopodia originates from its transport of cargo, including actin polymerization machinery, to the tips of these protrusions (Berg and Cheney, 2002; Tokuo and Ikebe, 2004b). However, as many of the cargos are omittable for filipodia formation, myosin may be contributing to filopodial formation through an alternative mechanism (Dobramysl et al., 2021b; Tokuo and Ikebe, 2004b; Zhang et al., 2004a).

In addition to carrying cargo via their C-terminal tail, all protrusion resident myosins interact with the plasma membrane, either directly or indirectly, suggesting the possibility that these motors could impact the force balance that controls protrusion elongation. Our group recently tested this concept using a genetically encoded, chemically inducible system, which enabled precise temporal control of myosin motor domain recruitment to the plasma membrane. Activation of this system led to a striking and robust elongation of large numbers of filopodia(Fitz et al., 2023); this effect was supported by motor domains from structurally distinct MyTH4-FERM domain containing myosins, different membrane

binding motifs, and was also operational in distinct cell types. Thus, beyond powering the tip ward transport of cargoes, myosin motors can also contribute to protrusion growth by applying barbed end directed mechanical force to the overlying plasma membrane and in turn, impacting the force balance that governs protrusion growth dynamics.

The question of how myosin-generated force might promote protrusion growth remains open. One possibility is that applying tip ward force to the plasma membrane somehow reduces the physical barrier encountered by the polymerizing ends of actin filaments in the core bundle. Such an effect could be mediated by driving the tip ward flow of lipids out to the distal tip, which might lower membrane tension. Alternatively, such force might accelerate retrograde flow of the core actin bundle, which could effectively "unload" the barbed ends of core bundle actin filaments, allowing for more rapid polymerization. Although these ideas are intuitive, the mechanistic details of how protrusion resident myosins promote growth remain unclear, primarily because of the lack of quantitative information on the number of force generators that are active in individual growing protrusions. Such information will be critical for building physical models that take into account mechanical contributions from both force generating systems (actin filaments and protrusion resident myosins).

In this work, we combined an inducible filopodial growth system with a live cell single molecule imaging approach, to count the number of myosin motors in individual growing protrusions. While previous studies used theoretical models to approximate the forces needed to overcome the forces of membrane tension (at minimum ~10-20 pN) to allow filopodia to elongate (Mogilner and Rubinstein, 2005). While *in vitro* studies have identified the forces of both polymerizing actin filaments (~1.3 pN/actin filament) and

myosin motors (~1-2 pN/myosin), each filopodium has a range of actin filaments (10-30), although the number of myosin motors needed for protrusion elongation has never been quantified in live cells (Footer et al., 2007a; Tyska et al., 1999).

RESULTS

Developing an approach for counting myosin molecules in growing filopodia

To count myosin force generators in elongating filopodia, we first sought an approach that would enable visualization and tracking of single myosin molecules within individual protrusions. To this end, we took advantage of the SUperNova (SunTag) system, a novel tagging scaffold that recruits up to 24 copies of GFP to enhance the signal of a single protein (Tanenbaum et al., 2014). The SunTag system allows for the amplification of the signal originating from a single molecule through an antibody-peptide interaction, such that conventional imaging methods, including spinning disk confocal microscopy, can be used for image capture. Here, a protein of interest is tagged with a tandem repeat of the GCN4 peptide and co-expressed with a single-chain variable fragment (scFV) fused with superfolder GFP, which tightly binds GCN4 (referred to as scFV-GFP in this report) (**Fig 4-1A**). Tanenbaum et al., originally used a 24 tandem repeat to visualize individual kinesin motors moving along microtubules in live cells, and since then the SunTag system has been used to visualize a plethora of molecules in live-cells (Das et al., 2023; Ershov et al., 2022; Tsirkas et al., 2022).

Our intent in the current study was to combine the high signal/noise ratio offered by the SunTag with the myosin-driven model of filopodial growth described in our previous

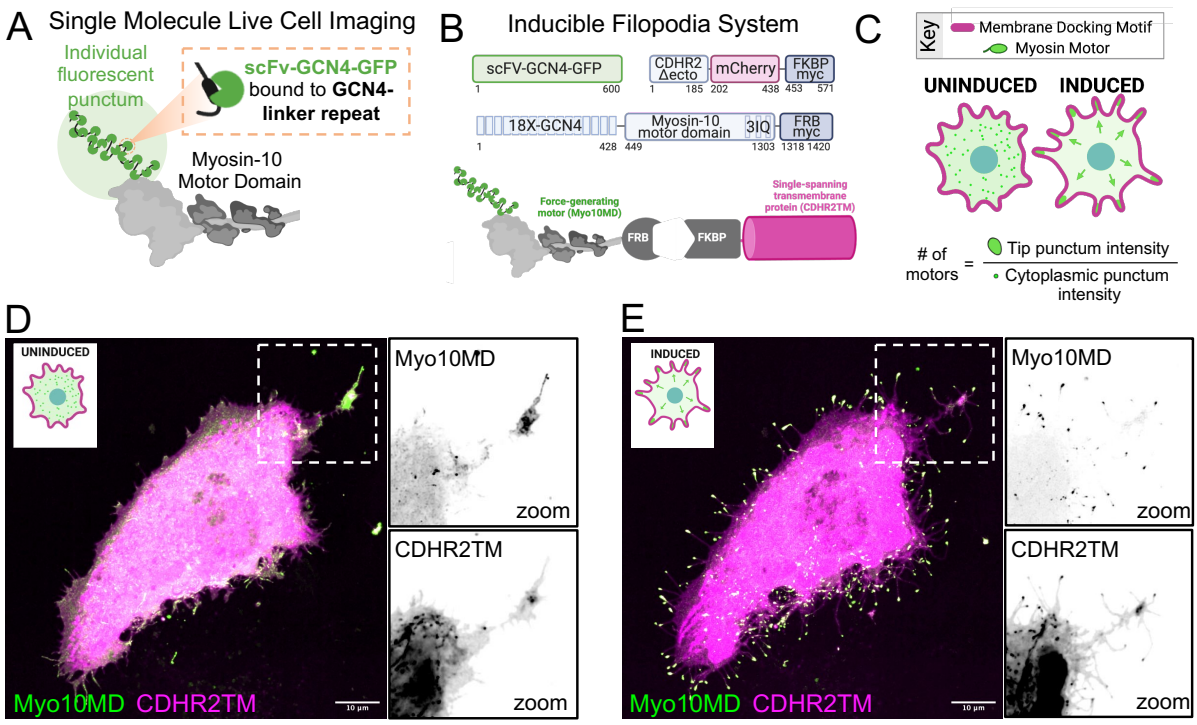

Figure 4-1: Single molecule confocal imaging using the SunTag system. (A) Schematic of the antibody-peptide labeling strategy to amplify the signal of a single protein of interest, the motor domain of myosin-10. **(B)** Cartoons depicting the three constructs transfected into cells to induce filopodia elongation; numbers represent amino acids (top). Cartoon demonstrating the FRB-FKBP domains that dock the motor domain to the membrane upon the addition of rapalog (bottom). **(C)** Graphic of the functional output of these experiments, where the ratio of the signal intensity of induced filopodia tips to the cytoplasmic punctum intensity represent the number of myosin motors needed to induce the growth of individual cellular filopodia. **(D)** Confocal maximum intensity projection image of a HeLa cell expressing the 18xGCN4-linker-Myosin-10 motor domain (Myo10MD) with scFV-GFP (green) and CDHR2TM (magenta) before filopodial induction. **(E)** Confocal maximum intensity projection images of a HeLa cell expressing the 18xGCN4-linker-Myo10MD with scFV-GFP (green) and CDHR2TM (magenta) 30 min after filopodial induction. Scale bar = 10 μm.

work (Fitz et al., 2023). That genetically encoded system takes advantage of the rapalog-inducible heterodimerization of FRB and FKBP to dock force-generating myosin motor domains to the plasma membrane via a range of binding motifs (**Fig 4-1B**). In the minutes that follow activation with rapalog, we observe robust filopodial elongation. We reasoned that combining these tools would allow us to activate filopodial growth and simultaneously monitor the number myosin motors that accumulate in growing protrusions in real time (**Fig 4-1C**).

Our previous experiments established that myosin-driven filopodial growth is supported by motors with diverse biochemical properties, from classes 3, 10, and 15 (Fitz et al., 2023). For the current studies, however, we focused specifically on Myo10 as a model myosin. Because the larger variants of the SunTag (i.e. with many tandem GCN4 repeats) are predicted to be bulky and thus, hold some risk of impairing function, we first set out to determine the shortest SunTag that would still enable single molecule visualization using spinning disk confocal microscopy, while supporting filopodial elongation. Testing a range of constructs composed of increasing numbers of tandem GCN4 repeats (4x, 8x, 12x, 14x, 16x, 18x, 20x and 24x) revealed that the 18xGCN4 tag offered the brightest, visible cytoplasmic puncta that still demonstrated robust accumulation in growing filopodia (compare **Fig. 4-1D** to **Fig. 4-11E; Supp Fig 4-1**).

Defining the signal intensity of puncta representing single Myo10MD molecules

Hela cells transfected with SunTagged Myo10MDs were subject to volume imaging with spinning disk confocal microscopy, which enabled us to capture all filopodia, independent of whether they were substrate-attached. To determine the intensity of individual myosin motors in the cytoplasm prior to filopodia elongation. While we could

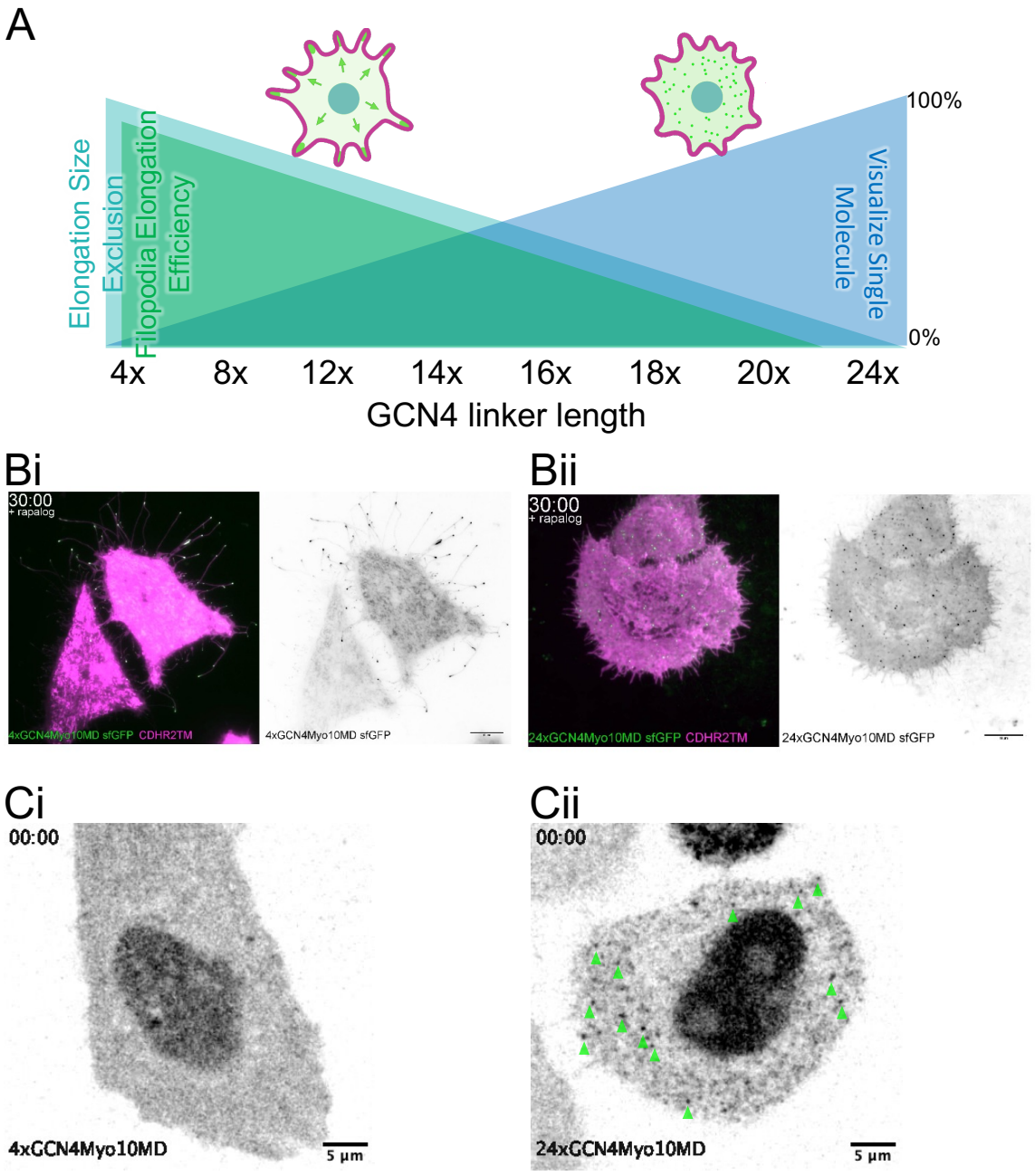

Supp Figure 4-1, related to Figure 4-1: 18X-GCN4 tag provides the brightest, visible cytoplasmic puncta that can still elongate filopodia. (A) Cartoon schematic of the inverse relationship between linker length to elongate filopodia and also be visualized as cytoplasmic puncta. **(B)** SDCM stills of single HeLa cells transfected with CDHR2TM (magenta) and either 4xGCN4- (Bi) or 24xGCN4- (Bii) Myo10MD (green) 30 min after the addition of rapalog. **(C)** TIRF stills of single HeLa cells transfected with CDHR2TM (magenta) and either 4xGCN4- (Ci) or 24xGCN4- (Cii) Myo10MD (green).

visualize these puncta, both diffusion and illumination of a deeper z-range (SDC compared to TIRF) decreased the signal-to-noise ratio and made quantification challenging. To gain an accurate measurement of single molecule intensities, unaffected by diffusion, we depleted cells of ATP to localize soluble myosin motors to the basal actin cytoskeleton of the cell (compare **Fig 4-2A** with **Fig 4-2B**). As most cells have characteristic actin stress fibers on their basal surface, we imaged the ventral surface of cells after adding 0.05% sodium azide and 10 mM 2-deoxy-D-glucose, which gradually depletes cytoplasmic ATP levels (Tyska and Mooseker, 2002). Within 15 minutes of ATP depletion, we could visualize new, bright myosin puncta in our imaging plane (compare **Fig 4-2C** with **Fig 4-2D**). Using TrackMate, we quantified the sum intensities of puncta that came into the frame and remained in frame for at least 0.9 s (Ershov et al., 2022; Tinevez et al., 2017) eliminating any transient puncta, not in frame, and keeping only the brightest puncta for the analysis (**Supp Fig 4-2**). Quantification of the Myo10MD puncta with background intensity subtracted determined that a single Myo10MD puncta had an average intensity of 320, 12-bit gray values (**Fig 4-2E**).

Elongating filopodia contain tens of My10MD molecules

To quantify the number of 18XSunTag-Myo10MD myosin motors that accumulate in growing filopodia, we induced elongation with 30 min of rapalog treatment and identified new filopodia for further analysis. 3D thresholding was used to isolate the SunTag signal enriched at the distal tips of protrusions. Dividing the sum signal derived from these measurements with the single motor calibration unit, defined above, we found that elongated filopodia tips had an average of 12.4 ± 2.2 motors [GeoMean ±

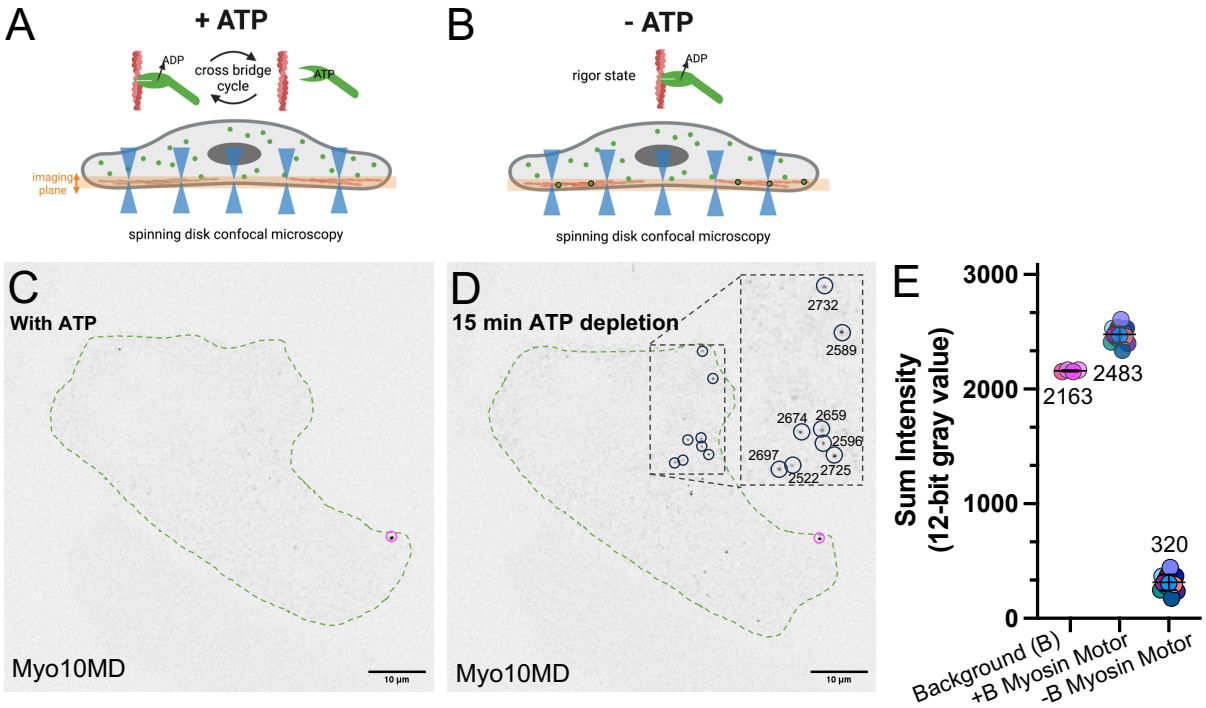

Figure 4-2: Myosin motors in a rigor state optimize the quantification of cytoplasmic motor puncta using confocal imaging. (A and B) Schematic of the ATP depletion experiments. Upon ATP depletion myosin motors become locked in the rigor state, bound to actin, which increases the number of motors in the single z-imaging plane using spinning disc confocal microscopy (compare A and B). **(C)** Still of a confocal microscopy live-cell imaging movie of HeLa cells expressing 18XGCN4-Myo10MD with scFV-GFP (inverted; black) before ATP depletion; cell body outlined in green. **(D)** Still of a confocal microscopy live-cell imaging movie of the same HeLa cells shown in C expressing 18XGCN4-Myo10MD with scFV-GFP (inverted; black) 15 min after ATP depletion; cell body outlined in green; black circled puncta denote single myosin motors in the imaging plane compared to C. Zoom shows eight puncta that were measured with the sum intensity below each puncta. **(E)** Sum intensities of puncta from ATP depleted cells; each dot represents the average sum intensity of all puncta measured per cell. n = 100 puncta from 4 cells (background); n = 292 puncta from 13 cells (myosin motor); Values represent the average intensity of background, myosin motor puncta with background included (+B), and myosin motor puncta with background subtracted (-B), with 320 denoting the average intensity of a single myosin motor. Puncta seen in both pre and post ATP depletion experiments (circled in red in C and D) were excluded from the analysis. Scale bar = 10 µm.

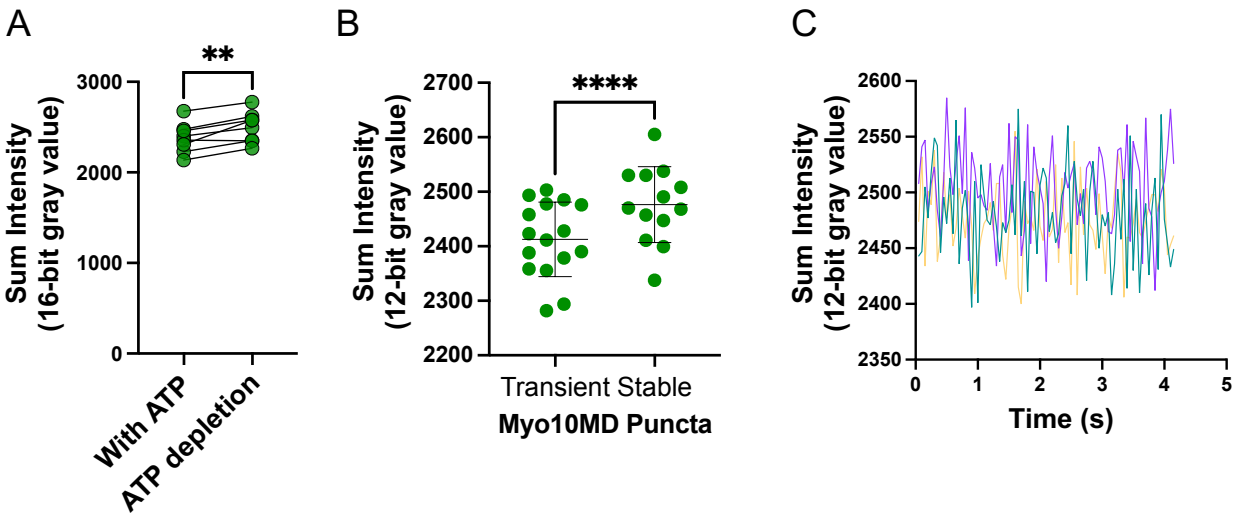

Supp Fig 4-2, related for Figure 4-2: Stable puncta under ATP depletion are brighter. **(A)** Comparison of the average sum intensities of Myo10MD puncta measured in TrackMate before and after ATP depletion using a paired t-test. Each dot represents a single cell average; n = 8 cells with > 11,000 individual puncta. **(B)** Comparison of the average sum intensities of Myo10MD puncta that are transient (in frame for less than 0.9 s) or stable (in frame for more than 0.9 s) using the Student's t-test. Each dot represents a single cells average; n = 13-15 cells with 165-1588 individual puncta. **(C)** Puncta that remained in frame for the duration of the entire acquisition did not undergo photobleaching. n = 3 of the longest capture puncta. Error bars represent the mean ± SD; ** $p \leq 0.01$, ****$p \leq 0.0001$.

GeoSD], ranging from 2-349 (**Fig 4-3A**). To calculate the amount of force the population (F_{avg}) of 14 motors would provide, we multiplied the number of motors by the reported duty ratio of myosin-10 (F_{iso}; 0.7) by the average amount of force one motor produces (F_{uni} ~1 pN) ($F_{avg} = F_{uni} * \#\ of\ motors * F_{iso}$) (Guilford et al., 1997; Homma and Ikebe, 2005; VanBuren et al., 1994). This calculation produced an average force of 8.7 ± 1.5 pN [GeoMean ± GeoSD].

We were curious if the filopodia tips with 100s of motors were accumulating motors after reaching a maximum length. To test this, we generated a full-length myosin-10 construct tagged with the same 18xGCN4 linker repeats. Over-expressing myosin-10 has been shown to be sufficient for the initiation of filopodia formation and subsequent elongation, but due to the nature of transfections, most of the filopodia that are produced in this manner are mature, providing no insight into their lifetime (Berg and Cheney, 2002; Kerber and Cheney, 2011; Sousa and Cheney, 2005). 3D analysis of filopodia tips generated from full-length, 18xGCN4 myosin-10 showed an average number of 8.6 ± 2.60 motors [GeoMean ± GeoSD], ranging from 1-177 motors (**Fig 4-3B**). Interestingly, these values of motors are in the same range of motor required for filopodia elongation using only the motor domains, suggesting a similar number of motors contribute to elongating filopodia with or without the C-terminal tail.

Next, we were next curious if the dynamic properties of elongating filopodia varied dependent on the number of motors at filopodial tips. Using a higher-temporal resolution of 15 s/frame but a low z-resolution (0.5 μm) we could visualize the elongation of individual filopodia (**Fig 4-4A**). After 30 min of imaging, we could then capture entire tips of filopodia that had elongated using a high z-resolution (3 um) (**Fig 4-4A, right**). Because these data

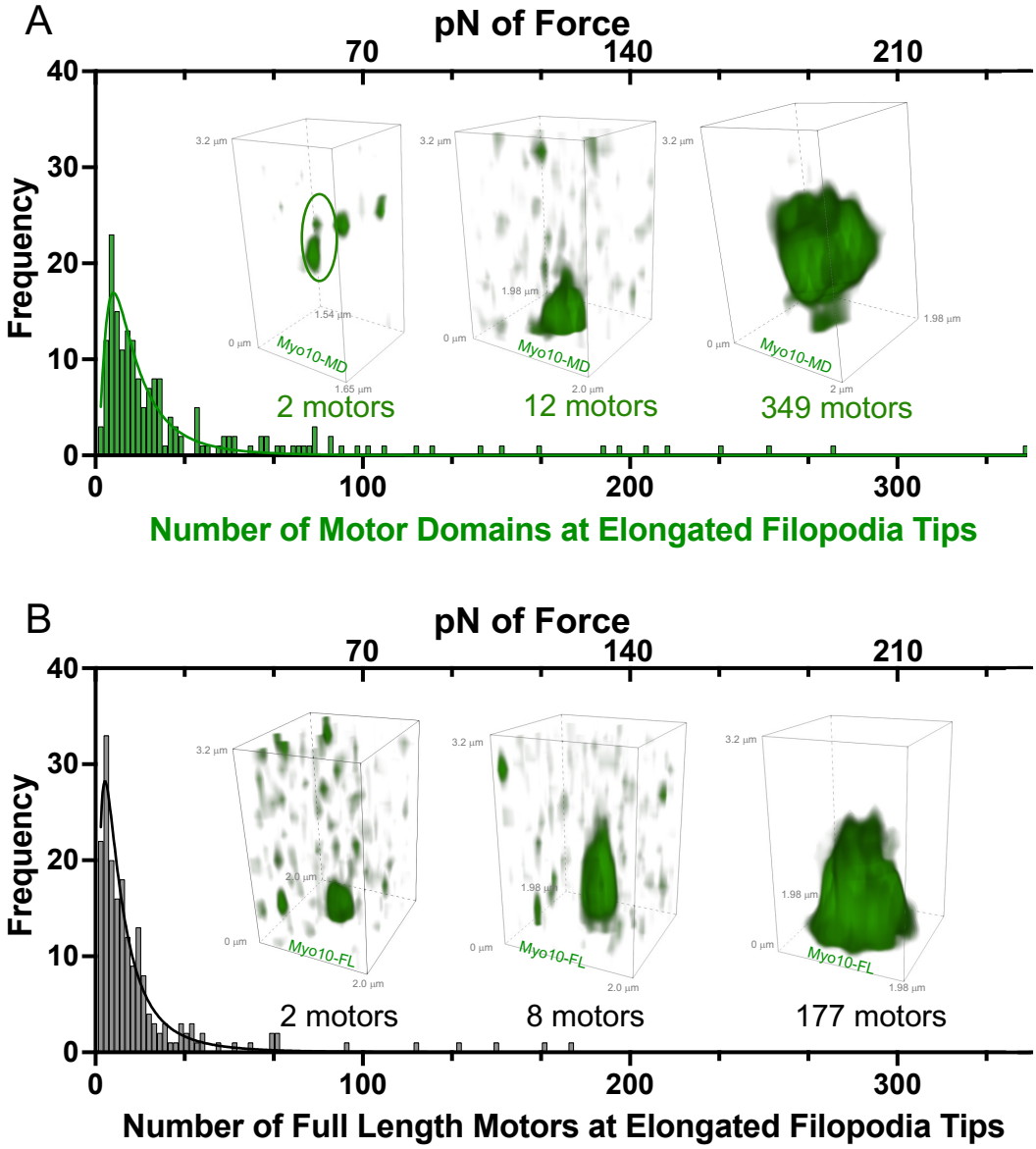

Figure 4-3: Elongated filopodia contain an average of 12 myosin-10 motor domains. (A) Lognormal distribution of the number of myosin-10 motors at the tips of elongated filopodia with an average of 12.4 ± 2.20 motors [GeoMean ± GeoSD]. Images depict 3D deconvolved volume projections of the tips of elongated filopodia showing examples of the smallest (2 motors), largest (349 motors) and average (14 motors) number of motors calculated; n = 14 cells, 182 individual filopodial tips. **(B)** Lognormal distribution of the number of full length myosin-10 molecules at the tips of elongated filopodia with an average of 8.6 ± 2.60 motors [GeoMean ± GeoSD]. Images depict 3D deconvolved volume projections of the tips of elongated filopodia showing examples of the smallest (2 motors), largest (177 motors) and average (8 motors) number of motors calculated N = 18 cells, 189 individual filopodia.

sets were imaged every 15 s for 30 min, we were not as confident in the calculating the number of motor calculations due to the effects of photobleaching. We, therefore, decided to bin the data into filopodia that had elongated either with a “high” (more than 12 motors) or “low” (less than 12 motors) number of motors, using the average number of motors from Fig 3 as a cutoff. Interestingly, the number of motors changed neither the persistence nor velocity of the elongating filopodia (**Supp Fig 4-4**) but did change the length of the filopodia. Filopodia that had more myosin motors had a longer final filopodia length (**Fig 4-2B**), suggesting that a higher number of motors is optimizing actin polymerization to allow filopodia to reach longer final lengths.

DISCUSSION

In this report, we utilize the previously characterized SunTag system to amplify the signal of a single myosin motor domain under spinning-disc confocal microscopy to quantify the number of motors at the tips of newly elongated filopodia. We found that filopodial tips contain an average of 12 motors, but with as few as 2 and as many as 349, which suggests that force generated from myosin-10 motor domains can contribute an average force of 8.4 pN. This value is on the same pN-scale of estimated core bundle pushing forces, suggesting an equal balance of the forces of myosin and actin at filopodial tips. However, if an increased number of motors does not change either the velocity or persistence of elongating filopodia, it begs the questions of how myosin is contributing those forces to regulate filopodia length. One hypothesis is that those forces are assisting to make the barbed ends more accessible to the incorporation of new G-actin monomers by physically displacing the core bundle towards the cell body while also displacing the

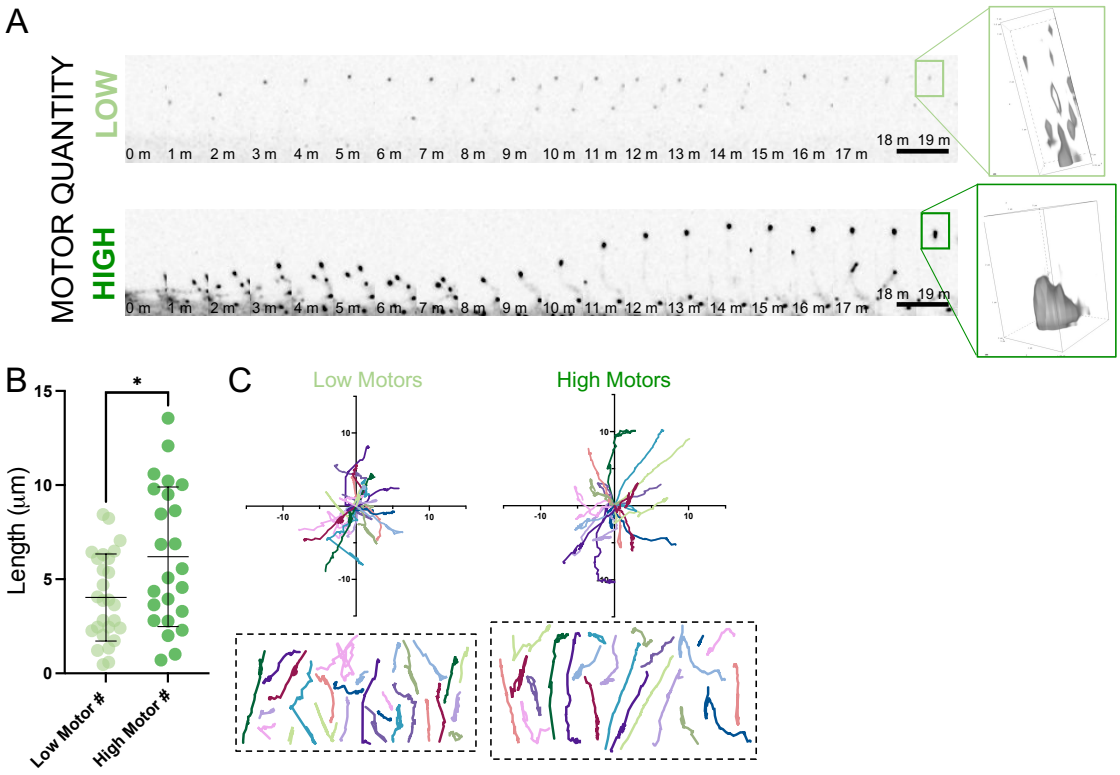

Figure 4-4: Filopodia with 12 or more motors reach higher final lengths. (A) Montage of single filopodia elongating on a HeLa cell expressing 18xGCN4-Myo10MD-FRB with scFV-GFP (green) and CDHR2TM (not shown) containing a low (2; top) or high (47; bottom) number of motors. Right image depicts a 3D deconvolved volume projection of the elongating filopodia tip at the final time point. Scale bar = 5 mm; LUTs matched to high motor montage; still every 1 m. **(B)** Final lengths of filopodia elongated with either a high (more than 14; dark green) or low (less than 14; light green) number of motors. Error bars represent the mean ± SD; *p < 0.05. **(C)** Rose plots of individual trajectories of filopodia containing either a high (more than 12; left) or low (less than 12; right) number of motors. Dashed boxes below depict the individual tracks of filopodia; n = 23 (high) 28 (low) filopodia (B-D). Scale axis = 10 mm as denoted.

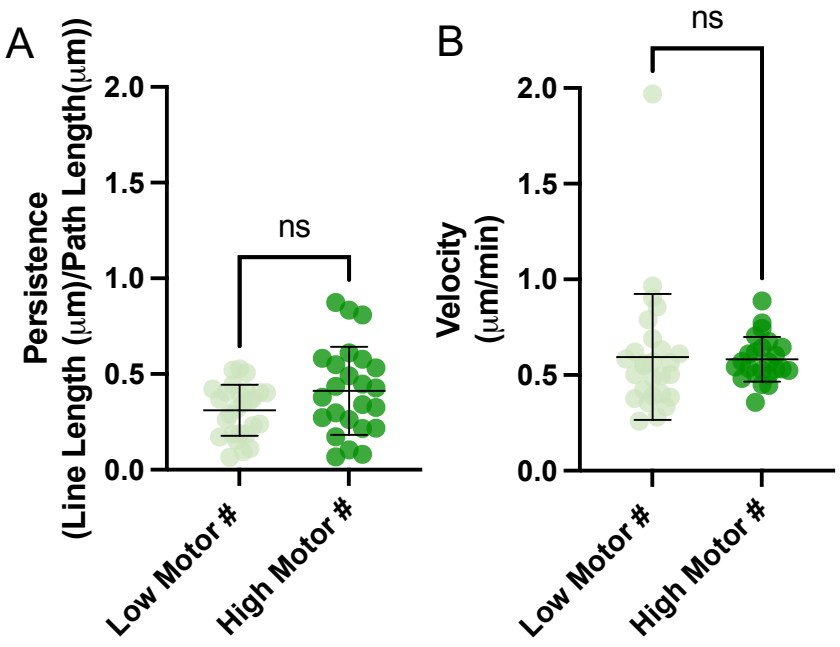

Supp Figure 4-4, related to Figure 4-4: Neither persistence nor velocity between elongated filopodia, containing either a high or low motor number, is altered. (A) Persistence of individual growing filopodia that contained either a high (more than 12) or low (less than 12) final number of motors. **(B)** Velocity of individual growing filopodia quantified by the path length divided by the sum time. Final lengths of filopodia elongated with either a high (more than 12; dark green) or low (less than 12; light green) number of motors. Error bars represent the mean ± SD; ns $p > 0.05$.

membrane forward. In this way, area between the membrane and the barbed ends of the core actin bundle becomes open for G-actin incorporation. Additionally, it was previously shown that the actin shaft of filopodia performs a rotational motion, which is reduced upon myosin-10 depletion(Leijnse et al., 2022). In this context, myosin-10 may be helping to maintain the rigidity of the core bundled to optimize the actin polymerization pushing force.

A recent study also estimated the number of myosin-10 molecules at filopodia tips, but through an analysis that combined the overexpression of a HALO tagged full length myosin-10 overexpression with SDS-PAGE. While this study estimates that 100s of myosin-10 motors accumulate at filopodial tips, the nature of their over-expression experiments provided no temporal control over the onset or lifetime of the filopodia that were measured. Even so, the authors go on to suggest that only ten or fewer myosin-10 molecules may be necessary for filopodia initiation (Shangguan and Rock, 2023), a value that is in agreement with our results.

GFP (238 AAs) resembles a cylinder with a diameter and length of roughly 2.4 and 4.2 nm, a relatively large fluorophore(Hink et al., 2000). To amplify the signal intensity of a protein of interest, the fusion of multiple copies of GFP has previously been used; however, greater than three copies of GFP is often problematic due to bacterial recombination that can occur when generating the plasmid. The SunTag system utilizes a scFV, which specifically binds a short GCN4 peptide sequence (19 AAs), allowing for proteins of interest to be fused with the multimerization of up to 24 GCN4 linker repeats to amplify a protein of interest to visualize individual molecules in live-cells. In applying the SunTag system to our previously published inducible filopodia system, we were able

to visualize individual myosin motors to quantify the number of motors at the tips of nascent filopodia. During these experiments, we learned that longer linker lengths (greater than eighteen) were unable to elongate filopodia. While longer linker lengths may be generating nonfunctional motor domains, it is also interesting to ponder whether these motors are physically too large to enter, or to allow for enough motors to enter, the space between the plasma membrane and actin. From this perspective, we can approximate the occupation in 3D space of myosin-10 motors from previous studies that have resolved its structure (Ropars et al., 2016). Assuming an elliptical (Myo10MD) and spherical (GCN4 and GFP) cylinder shape, the volume of a single motor domain, single GCN4 linker, or single GFP barrel is roughly 173, 0.09 and 1.45 μm^3, respectively. This would mean the approximate volumes of GFP-Myo10MD, 18xGCN4-Myo10MD and 20xGCN4-Myo10MD are, respectively, 174.45, 174.62, and 174.8 μm^3. Is an increase of ~180 nm^3 enough to exclude a construct from the base of filopodia? Due to previous electron microscopy (EM) fixing methods, high-resolution images of the actin-core of filopodia did not include the membrane (Svitkina et al., 2003). However, with the advance of cryogenic transmission EM, a study in *Dictyostelium* have shown that the space between the actin-core and encapsulating membrane is ~9.2 nm (Medalia et al., 2007). Future studies will need to use cryo-EM to image endogenous, mammalian filopodia in addition to filopodia generated using our system to better understand the 3D spacing of the actin, membrane, and motors in elongated filopodia. This will provide the framework to create an accurate model of how myosin, actin, and the membrane are orientated in space.

Our previous study showed that the motor domains of the tip-specific myosins of stereocilia, 3a and 15a, were also able to elongate filopodia using our inducible system

(Fitz et al., 2023). Interestingly, the final average length of filopodia were significantly shorter when elongated using the stereocilia motor domains. As the superfamily of myosins have a vastly large range of mechanochemical properties, understanding how their diverse properties effect the dynamics of individual protrusion growth and why some motors are better able to elongate filopodia than others, using this SunTag system will be a point of interest moving forward.

Why do some elongating filopodia have only 4 motor domains while others have up to 50 or more? If we consider the problem of protrusion formation we can imagine that the main physical barrier to growth is the barrier of the plasma membrane. Specifically, membrane tension will be one facet in determining how much force is needed to overcome the membrane tension to physical bend the membrane outward. Previous work has suggested that forces in the range of 5-30 pN are needed to extrude empty membrane tubes from the cell surface (Sheetz, 2001; Sheetz et al., 1992), and that membrane tension is heterogenous throughout a single cell, as no long-range propagation of membrane tension was seen after local perturbations(Shi et al., 2018). Further, membrane tension is also highly variable among cells types: macrophage (~69 pN), astrocyte and cardiomyocyte (~32-35 pN), neuron (~15 pN) (based on membrane tether measurements)(Hissa et al., 2017; Portera-Cailliau et al., 2003). This would suggest that individual cell surface protrusions are each unique, even if protruding from the same cell, and therefore will need various amount of force to emerge. From this perspective, it is reasonable to hypothesize that motors will need to overcome varying levels of membrane tension in the protrusions in which they reside. As each type of actin-based protrusion has a unique set of classes of myosins, these myosin classes and their

respective mechnoproperties may be optimized to allow them to contribute the necessary amount of force in each type of actin-based protrusion (stereocilia, microvilli and filopodia).

What do these studies imply about native filopodia elongation? Endogenous filopodia elongation is more complicated than our filopodia system, which at minimum requires actin and the docking of the myosin motor domain to the membrane. In addition to interacting with the membrane, myosin tails are also able to interact with other proteins and bind cargo, such as VASP and β-integrins, and other actin-based machinery have previously been implicated or shown to contribute forces for filopodial elongation (although most of these proteins are sufficient but not required for elongation) (Dobramysl et al., 2021a; Kovar and Pollard, 2004a). Further, unlike our system, native myosin does not bind to the membrane for as long of a duration as in our system as dissociation constants between the membrane and its cargo are in play. This implies that the estimated ~10 pN of force identified in this system contribution of myosin-generated force is likely an overestimation of the force it is contributing *in vivo*. In combination with previous studies, this work provides an additional component to add to physical models of protrusion growth.

CHAPTER V: CONCLUSIONS AND FUTURE DIRECTIONS

CONCLUSIONS

Overall, these two projects highlight the force-generating role of myosins in actin-based protrusions in addition to their ability to carry cargo. The first story generated an in-cell system to test the idea that myosin contributes to protrusion formation by remodeling the cell morphology through their interactions with the membrane. The idea that myosins contribute force to the biological contexts in which they reside has long been postulated in the field but not directly test. This is because this question has been technically challenging as it requires uncoupling the cargo carrying function of the myosin tail from its ability to bind the plasma membrane. Notably, while previous research suggested the involvement of myosins in delivering essential regulatory and structural cargoes for actin-based protrusion assembly, this thesis work represents the first direct evidence that myosin-generated forces can drive protrusion growth.

Currently in the field there are two models of filopodia elongation: the (1) convergent elongation model and (2) tip nucleation. In the convergent elongation model, filopodia are initiated from the free barbed ends of actin filaments at the cell periphery of Arp2/3-mediated lamellipodial networks. These barbed ends likely contain a tip complex that includes barbed end associated proteins, such as formins, Ena/Vasp and myosin-10, which help to cluster and elongate actin filaments to protrude from the cell surface (**Fig 5-1**) (Mattila and Lappalainen, 2008; Svitkina et al., 2003). In contrast, in the tip nucleation model, filopodia emerge from actin filaments that are directly nucleated from clusters of membrane associated formins, which produce a core actin bundle to protrude from the

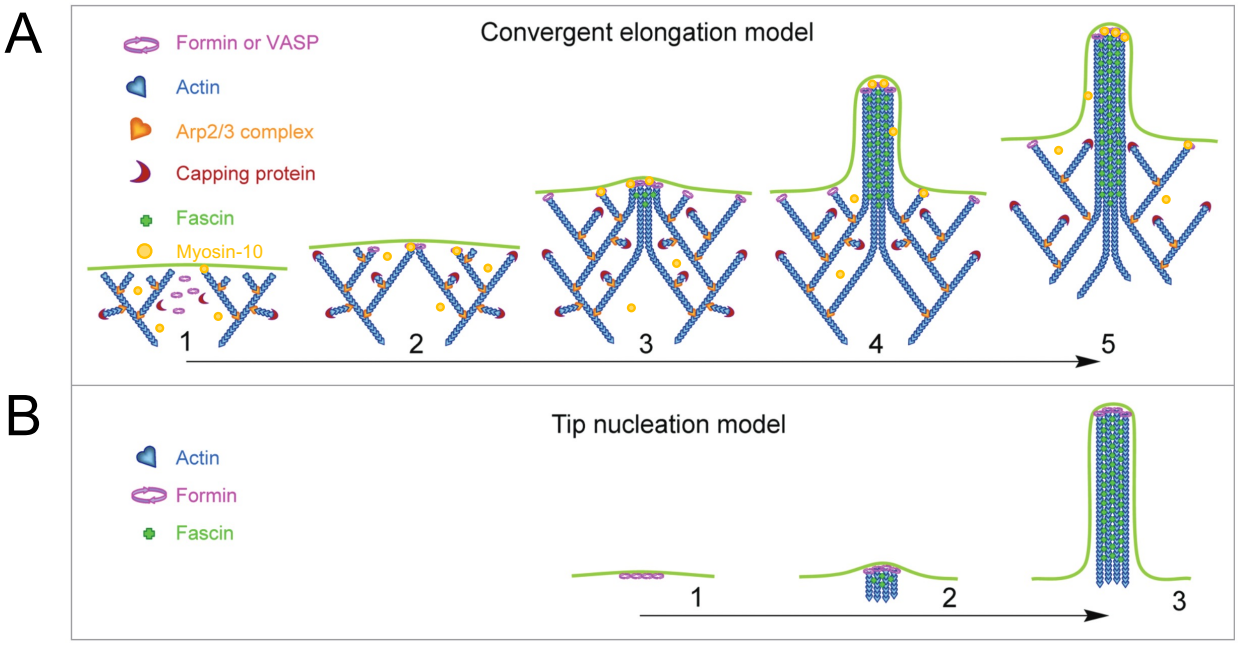

Figure 5-1: Two models of filopodia initiation. Adapted from (Yang and Svitkina, 2011). (A) Convergent elongation model, which includes the contribution of myosin-10 as first described by (Tokuo and Ikebe, 2004a). In the convergent elongation model, myosin-10 moves to barbed end actin filaments and assists in the convergence of filaments inducing the formation of microspikes that will continue to develop into filopodia. **(B)** Tip nucleation model.

cell surface (**Fig 5-1**). Formins, such as mDia1, are actin nucleators that mediate filament assembly (Courtemanche, 2018; Funk et al., 2019). The work in this study fits into the convergent elongation model, as filopodia formed from docking motor domains to the membrane were able to elongate filopodia independent of the formin, mDia1 (Fitz et al., 2023). Further, as our myosin constructs lacked the C-terminal tail, the interaction between myosin and the membrane is sufficient to elongate filopodia independent of myosin's ability to carry cargo. The ability of myosin to contribute growth promoting forces can be incorporated into future models for filopodia and other actin-based protrusion elongation models.

As our first study (***Chapter III***) established that, in addition to their cargo carrying function, myosins contribute growth-promoting forces to elongate protrusions, our second study aimed to understand how *many* motors were required to elongate filopodia through the docking of myosin to the membrane (***Chapter IV***). Cumulatively, this work identified that an average of 12 force-generating myosin motors can elongate filopodia. In addition to these findings, this works provides a temporally controlled in-cell assay to elongate filopodia, from which we can continue to understand actin-based protrusion elongation and initiation. Three main questions that arise from this work are (1) What is the ultrastructure of the actin cytoskeleton in filopodia generated via the myosin-membrane docking system? (2) Do biomechanical perturbations of the bilayer alter membrane tension or lipid species? (3) Can we apply the myosin-membrane docking system to elongate structures in other biological contexts?

Before diving deeper into these three questions, it is important to note that all the prior studies in this work were completed using over-expression experiments, which generated a heterogenous population of cells of interest. For those experiments, the heterogenous population was not an issue as we were able to monitor individual cells. However, for most of the experiments proposed for these open-ended questions, a homogenous population of cells will need to be generate due to the technicalities of the methods proposed. To do these experiments, we first need to generate a stable cell line, which expresses the myosin-membrane docking system, to obtain a homogenous population of cells. In preliminary data, we have successfully cloned and confirmed the functionality of a myosin-membrane docking system embedded in a single plasmid using the IRES element, which allows for the translation of two separate protein products from a one plasmid (Mountford and Smith, 1995). In this IRES construct, only the myosin-10 MD is tagged with a fluorescent protein, in this case StayGold, (Hirano et al., 2022) so that we can still monitor the movement of myosins in filopodia elongation while also leaving three (405, 568, 647 nm) fluorescent wavelengths open for imaging. Many of the experiments outlined below will utilize this tool, herein referred to as the “myosin-membrane docking system”.

FUTURE DIRECTIONS

What is the ultrastructure of the actin cytoskeleton in filopodia generated via the myosin-membrane docking system?

Determine the number of actin filaments in filopodia generated via the myosin-membrane docking system.

Our initial study determined that myosin-generated force contributes to actin polymerization force to elongate filopodia. While we also know from previous studies that a single actin filament can generate roughly ~1 pN of force, we do not know how many actin filaments are in the filopodia generated in our myosin-membrane docking system. Estimates in the literature give a range of filaments supporting filopodia (10-30), and preliminary data from our first study suggest that there may be less actin in the newly formed filopodia compared to filopodia generated from the overexpression of myosin-10 FL (**Fig 5-2**). It is also interesting to speculate that because the filopodia induced by over-expressing myosin-10FL have a larger range of F-actin intensities, that over time more F-actin accumulates into existing filopodia structures and, therefore, the F-actin intensity could correlate to the lifetime of the filopodia. Cryo-EM would allow us to determine the number of actin filaments in filopodia generated via the myosin-membrane docking system. Understanding the stoichiometry between the number of myosins and number of actin filaments would complement these initial findings to directly calculate the contribution of actin generated forces in our myosin-membrane docking system.

To take this one step further, it would also be of interest to determine the protein composition of filopodia generated either with our membrane-docking system, myosin-10FL or native filopodia to determine whether additional actin binding and actin associated proteins are involved in the myosin-membrane docking system or not. While our data support the elongation of filopodia independent of both VASP and mDia1, our data do not reveal, for example, if other formins have compensated for the loss of mDia1 (Fitz et al., 2023). To get a full picture of the underlying protein composition of these filopodia, we could utilize the stable myosin-membrane docking system cell line to induce

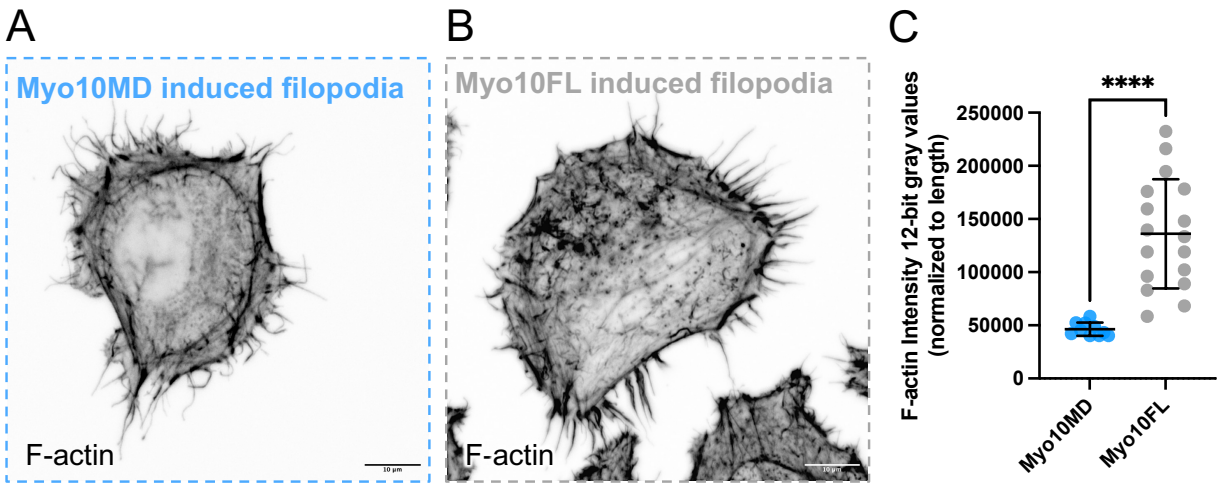

Figure 5-2: Filopodia generated through the myosin-membrane docking system have a lower F-actin intensity. (A) Max-IP of single HeLa cells overexpressing the myosin (Myo10MD-FRB; not shown)-membrane (CDHR2TM; not shown) docking system 25 minutes after rapalog addition to induce filopodial elongation stained with phalloidin to mark F-actin. **(B)** Max-IP of single HeLa cells overexpressing myosin-10FL (not shown) to induce filopodial elongation stained with phalloidin to mark F-actin. **(C)** Quantification in the F-actin intensity of individual filopodia. Intensity measurements were taken along the entire length of the filopodia and divided by length of the filopodia. Error bars represent the mean ± SD; ****$p \leq 0.0001$.

a large population of cells to elongate filopodia. We can physically remove filopodia from the fixed cells by centrifugation to then send the isolated filopodia from control and treated cells for mass spectrometry analysis. Not only could this open the door to incorporate additional proteins into the system generated in this work, but we can also understand if other proteins, in addition to the ones we have identified (myosin, actin, fascin), are contributing to filopodia elongation in the myosin-membrane docking system.

Defining the ultrastructure of the actin cytoskeleton at the leading edge before and after filopodial induction.

Our studies determined that when myosin-generated forces are physically docked to the membrane filopodia elongate but the number of filopodia does not change (**Fig 3-1 G, I**). This suggests that myosin-generated force is helping to elongate existing structures rather than creating new ones. To better understand where filopodia choose to elongate, cryo-EM can be utilized to resolve the ultrastructure of the actin cytoskeleton at the cell periphery in cells induced and not induced to elongate filopodia. I hypothesize that in uninduced cells, areas where actin filaments are linearly oriented into small microspikes serve as templates for filopodial elongation. If this is the case, the number of microspikes along the cell periphery will not be significantly different from the number of filopodia in induced cells.

Can we use the myosin-membrane docking system to remodel branched actin cytoskeletal networks?

These studies have focused on the ability of membrane-docked myosin motors to reshape the cell periphery into elongating, the linear actin-based protrusions, filopodia. In part this is because myosin-10 is optimized for processivity on linear bundled actin: the processivity of myosin-10 is nearly doubled on bundled actin than on single actin filaments (660 vs 310 nm/s) (Nagy et al., 2008; Ricca and Rock, 2010; Ropars et al., 2016; Takagi et al., 2014). In preliminary data, we also see the accumulation of myosin-10 motors along the leading edge of HeLa cells prior to filopodia elongation (**Fig 5-3**), likely at free barbed ends of lamellipodia structures. This localization was previously described in bovine arotic endothelial cells expressing full-length myosin-10, suggesting that this localization at the leading edge is in part due to the C-terminal tails ability to interact with the membrane (Kerber and Cheney, 2011). This raises the possibility that the motor domain of myosin-10 may assist in remodeling the branched actin network to converge actin filaments for filopodial elongation. *How* myosin-10 may be remodeling lamellipodial structures will be of interest in future studies. Additionally, in this work we utilized the sole pointed end directed myosin motor, myosin-6, as a control for barbed end myosin elongation. While, expectedly, we did not see any outward bending of the membrane when we docked the myosin-6 motor domain to the membrane, further studies may wish to optimize this motor to create an in-cell assay for cytoskeletal functions that require the inward bending of the membrane, such as endocytosis.

Do biomechanical perturbations of the bilayer alter membrane tension or lipid species?

Do filopodia elongate where membrane tension is low?

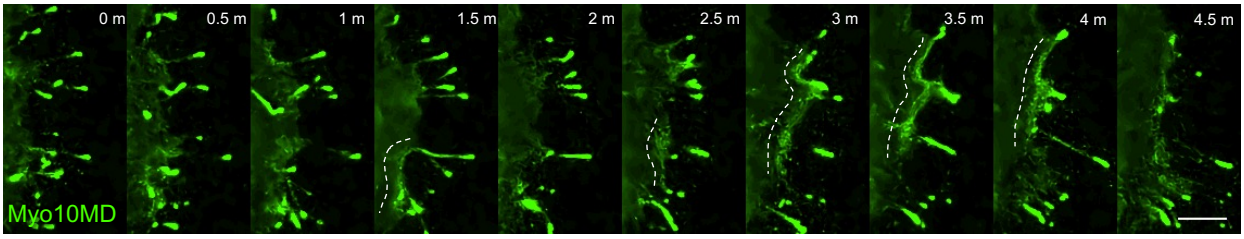

Figure 5-3: Montage of Myo10MDs along the edge of lamellipodia. Edge of a single HeLa cell expressing 18xGCN4-Myo10MD (green) and CDHR2TM (not shown) 7 minutes after the addition of rapalog to induce filopodia formation (0 m). White dashed lines highlight the flow of motors at the cell edge, likely at the edge of lamellipodia structures. Scale bar = 5 μm.

Previous research suggests that the membrane tension in a single cell is heterogenous, which could in-part explain the range of filopodial lengths of filopodia that elongated with the same number of myosin motors. From our first study, we also know that membrane availability limits filopodia elongation, as the addition of new membrane results in a further elongation of filopodia (**Fig 3-4**). However, whether filopodia prefer to form in areas with lower membrane tension or how the lipid bilayer flows or diffuses into elongating cell surface protrusions has not been experimentally shown. In preliminary experiments, we have attempted to answer these questions through immunofluorescent experiments (photobleaching or photoactivating membrane probes to visualize their movement; lipid probes that change their spectra depending on whether they are in order/disorder lipids (Colom et al., 2018)(MemGlow™); inducing cell shape changes via micropatterned coverslips (CYTOOchips™); depleting membrane cholesterol via methyl-β-cyclodextrin (Mahammad and Parmryd, 2015)), but each of these methods were inconclusive or inhibited the actin polymerization required for filopodia elongation. Until a tool to visualize local changes in membrane tension is developed, we may, instead, be able to visualize how the membrane diffuses into filopodia structures using the SunTag system. Overexpressing a membrane motif, such as CAAX (C-terminal membrane targeting domain of Ras (Wright and Philips, 2006)), tagged with a short GCN4 linker length in combination with the myosin-membrane docking system, is one way we could monitor the movement of individual lipids in cells expressing a low amount of the GCN4-linker CAAX motif during filopodia elongation. Alternatively, we could visualize the movement of lipids with quantum dots cross-linked to biotinylated lipids (Yu et al., 2019). Quantum dots are highly photostable and bright, easily allowing for visualization over long

periods of time (Pinaud et al., 2010) making them an optimal fluorescent source for imaging over the duration of filopodia elongation (~35 min). While there is currently not a direct way to measure local changes in membrane tension, understanding how the lipid bilayer moves to accommodate the robust influx of force will provide insight into how the cell membrane adapts to internal forces.

Does the application of a mechanical force alter the localization of lipid species?

The most abundant lipids in the plasma membrane are phospholipids, which contain two hydrophobic tails and a phosphate group attached to a hydrophilic head. A minor phospholipid species are a group of glycerophospholipids called phosphoinositides, which have a cyclic inositol group attached to the polar head phosphate (Falkenburger et al., 2010). This inositol head group contains three open hydroxyl groups which can be phosphorylated at the 3, 4, and 5 carbon positions, providing a total of seven distinct phosphoinositide species, a process regulated by distinct kinase and phosphatases. As a type of signaling lipid, phosphoinositides are involved in regulating membrane dynamics and membrane compartment identity. For example, phosphoinositol 4-phosphate (PI(4)P) is predominantly localized to the golgi, whereas phosphoinositol 3-phosphate (PI(3)P) is predominantly found on early endosomes (Antonietta De Matteis et al., 2005; Gillooly et al., 2003). The understanding of the sub-compartmentalization of various phosphoinositol species has largely been due to the development of fluorescently tagged lipid-binding protein domains, which act as phosphoinositide sensors (Balla et al., 2009; Balla and Varnai, 2009). Under live-cell analysis, these lipid sensors reveal the spaciotemporal organization of phosphoinositides.

In the context of actin-based protrusions, a recent study has shown that phosphoinositol species are enriched in various compartments of filopodia. By using phosphoinositol sensors, Jacquemet et al., showed enrichment of phophatidyinositol 3,4-biphosphate ($PI(3,4)P_2$) at filopodia tips, phosphatidylinositol 3,4,5-triphsphate ($PI(3,4,5)P_3$) along the entire filopodium, and little to no localization of either PI(3)P or PI(4)P (Jacquemet et al., 2019). This is the first study to predict roles for filopodial enriched phosphoinositol species in regulating filopodia structure and potentially formation.

As our myosin-membrane docking system provides temporal control over the onset of filopodia growth, we were curious if the tip localized $PI(3,4)P_2$ species could predict sites of elongation. We tried to answer this question by elongating filopodia in cells over-expressing the $PI(3,4)P_2$ sensor, TAPP-PH (Goulden et al., 2019). Based on preliminary data, we observed an enrichment of $PI(3,4)P_2$ after filopodia growth was initiated **(Fig 5-4)**. This suggests that the mechanical forces of myosin against the membrane initiate a signaling pathway to either recruit or generate more $PI(3,4)P_2$ species. Combining localization experiments with liquid chromatography-mass spectrometry analysis of filopodia (obtained in the same manner as described above for mass spectrometry) would provide a more detailed understanding of the types of phosphoinositol species localized in native, myosin-10FL-induced, or myosin-membrane docking system-induced filopodia.

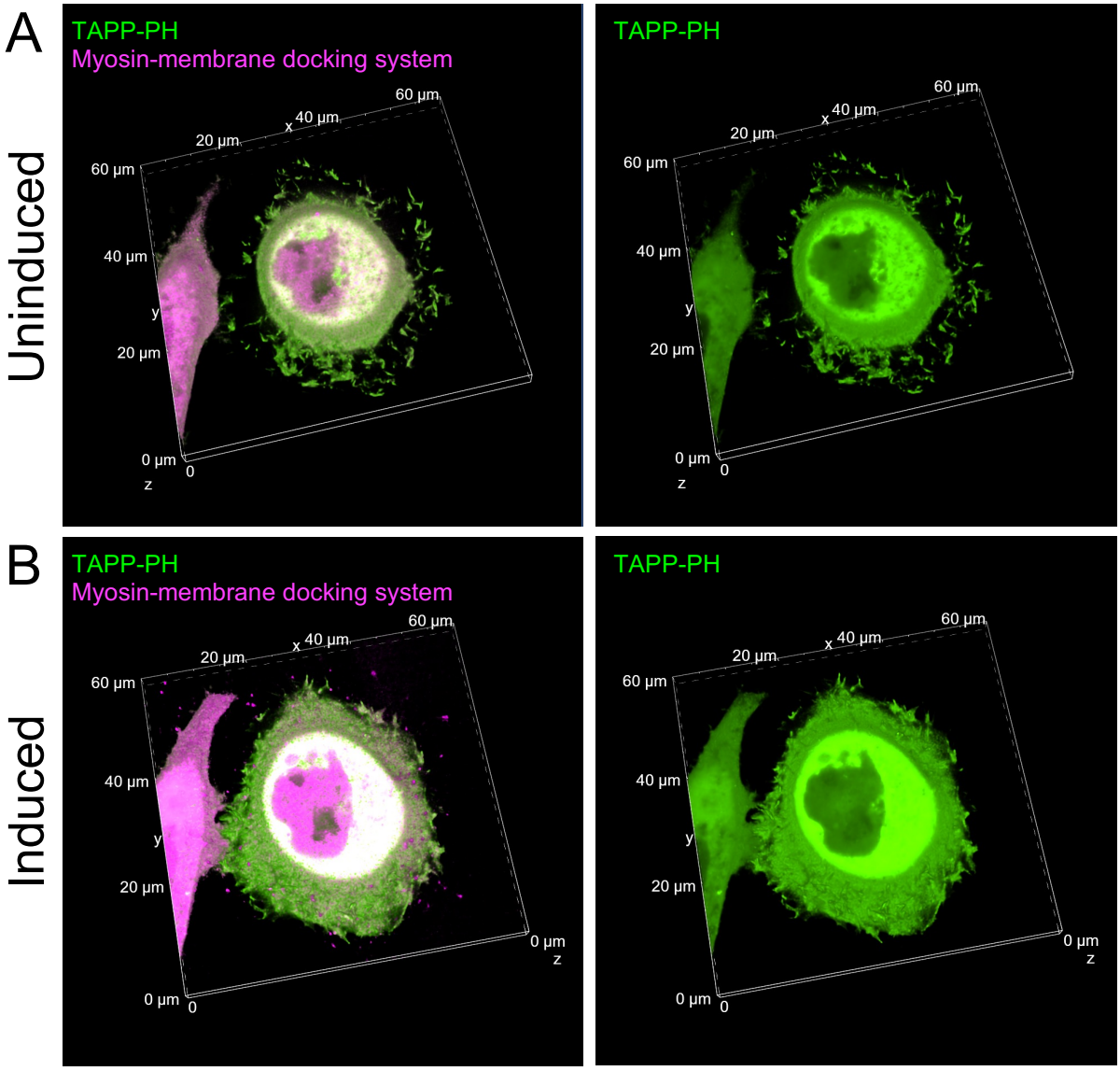

Figure 5-4: $PI(3,4)P_2$ localization and intensity increases upon activation of filopodial elongation. (A) 3D volume projection of a single HeLa cell transfected with TAPP-PH (green) and the myosin membrane docking system (myosin-10 motor domain in magenta) prior to filopodial growth induction. **(B)** 3D volume projection of a single HeLa cell transfected with TAPP-PH (green) and the myosin membrane docking system (myosin-10 motor domain in magenta) 15 minutes after the filopodial growth induction.

Can we apply the myosin-membrane docking system to elongate structures in other biological contexts?

The utilization of bioengineered tools to enhance or manipulate cell function is not a novel idea. In fact, recent work has engineered a suite of artificial myosin motors termed “Artificial Transport Vesicles”, ATVs, to directly manipulate long-range signal pathways through cargo transport for the larger goal of enhancing limb regeneration (Zhang et al., 2021) . When thinking about how the myosin-membrane docking system generated in this work could be applied to repair larger, (mm)-scale length defects, we searched for examples across the three domains of life where myosin localizes to the tips of protrusion-like structures. Interestingly, studies show that class 5 myosins are localized to the tips of both fungal hyphae and plant root hair cell tips, and deletion of these tip-localized myosin genes results in a decrease of both fungal radial growth and root hair length (Prokhnevsky et al., 2008; Renshaw et al., 2016) (**Fig 5-5**). Just as in our field, these studies contributed the defect in hyphae and root hair length to the loss of the cargo carrying function of the tip localized myosins. If myosin motors are also contributing force to help facilitate the elongation of hyphae and plant root hairs, it would be of high interest to determine whether we could apply our myosin-membrane docking system to control the elongation of these structures.

Specifically for plant root hairs, the ability to control their length could have greater impacts in the agricultural sector as climate change continues to wreak havoc on plant reproduction and crop output. As droughts continue to worsen, ensuring the elongation of root hairs to reach further into the ground for water will be critical to their livelihood. Future work will first need to first assess if actomyosin cytoskeleton proteins are decreased in

drought-stressed plants that display a short root hair phenotype. If actomyosin machinery is responsible for elongation, the tip localized myosins will be decreased. To understand if we can implement the myosin-membrane docking system in plant root hairs, we first need to resolve the proximity of the F-actin network at the distal tip of root hairs using super-resolution microscopy methods. Previous research shows that actin at plant root hairs is also oriented with the barbed end against tips, but whether this actin structure reaches to the cell periphery is unknown. With the ability to use CRISPR/Cas9 to edit the plant genome, we could then endogenously express the myosin-membrane system in plants under a root hair specific promoter (El-Mounadi et al., 2020). If myosin is contributing growth-promoting forces, introducing this system into the plants with short root hairs due to drought-stress should rescue root hair length.

While this last future direction expands beyond mammalian cells, biology continues to provide examples of conservation in both form and function. Applying our findings across disciplines is a creative way to contribute to larger societal outputs. In this case to improve crop performance and resilience under drought conditions, leading to more sustainable agricultural practices.

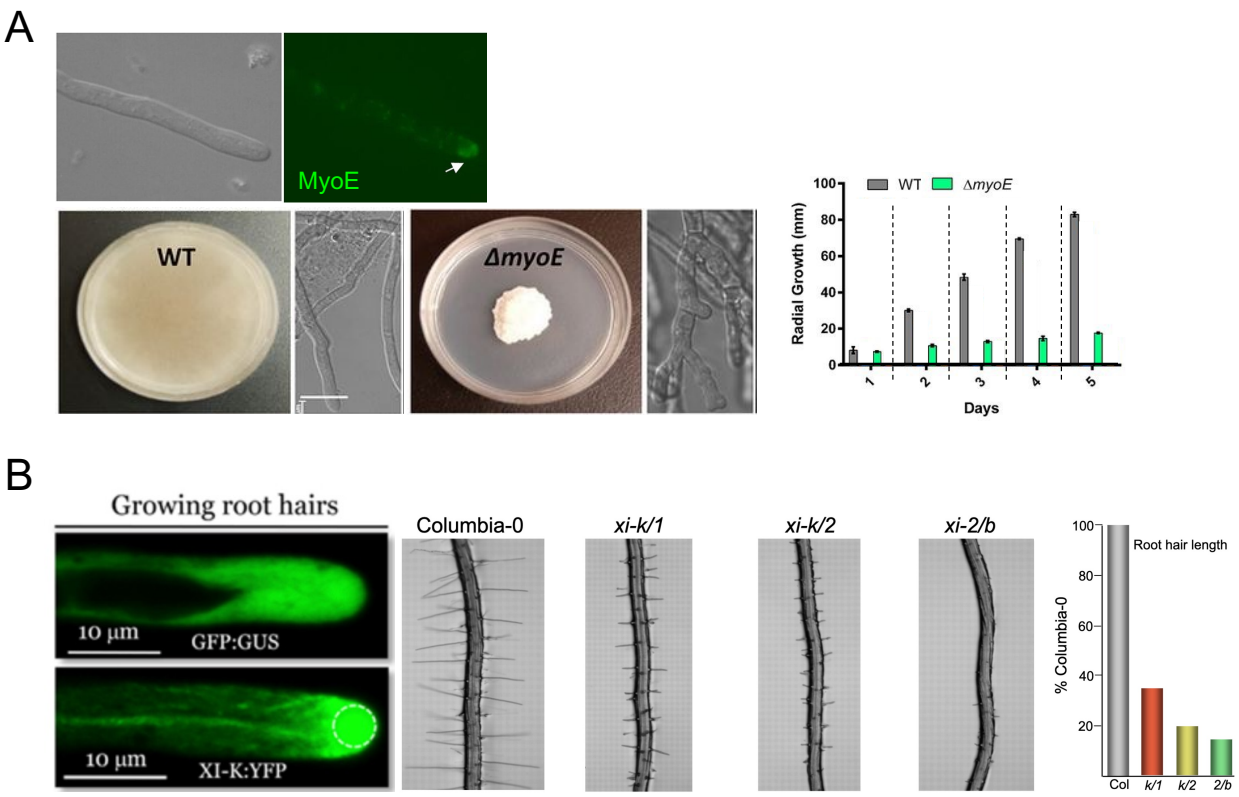

Figure 5-5: Myosin regulates length in the model fungi, *Aspergillus fumigatus* and plant, *Arabidopsis thaliana.* **(A)** Top: MyoE localizes to the hyphal tip; bottom: knock out of MyoE results in a decrease in radial growth (Renshaw et al., 2016). **(B)** Left: MyoXI localized to the tips of growing root hairs (Peremyslov et al., 2012); right: double knockouts of MyoXI with either Myo-K1, -K2 or -2b result in a decrease in average root hair length (Prokhnevsky et al., 2008). Scale bar = 10 μm.

REFERENCES

Alexandrova, A.Y., A.S. Chikina, and T.M. Svitkina. 2020. Actin cytoskeleton in mesenchymal-to-amoeboid transition of cancer cells. *Int Rev Cell Mol Biol*. 356:197-256.

Antonietta De Matteis, M., A. Di Campli, and A. Godi. 2005. The role of the phosphoinositides at the Golgi complex. *Biochimica et Biophysica Acta (BBA) - Molecular Cell Research*. 1744:396-405.

Arthur, A.L., A. Crawford, A. Houdusse, and M.A. Titus. 2021. VASP-mediated actin dynamics activate and recruit a filopodia myosin. *Elife*. 10.

Baglivi, G., and A. Pascoli. 1700. De fibra motrice et morbosa: nec non, De experimentis, ac morbis salivae, bilis, & sanguinis, ubi obiter de respiratione, & somno. De statice aeris, & liquidorum per observationes barometricas, & hydrostaticas ad usum respirationis explicata. De circulatione sanguinis in testudine, ejusdemque cordis anatome. Apud Costantinum.

Balla, T., Z. Szentpetery, and Y.J. Kim. 2009. Phosphoinositide signaling: new tools and insights. *Physiology (Bethesda)*. 24:231-244.

Balla, T., and P. Varnai. 2009. Visualization of cellular phosphoinositide pools with GFP-fused protein-domains. *Curr Protoc Cell Biol*. Chapter 24:Unit 24 24.

Banaszynski, L.A., C.W. Liu, and T.J. Wandless. 2005. Characterization of the FKBP.rapamycin.FRB ternary complex. *J Am Chem Soc*. 127:4715-4721.

Banga, I., and A. Szent-Györgyi. 1942. Preparation and properties of myosin A and B. *Stud. Inst. Med. Chem. Univ. Szeged*. 1:5-15.

Barger, S.R., N.C. Gauthier, and M. Krendel. 2020. Squeezing in a Meal: Myosin Functions in Phagocytosis. *Trends Cell Biol*. 30:157-167.

Bartles, J.R., L. Zheng, A. Li, A. Wierda, and B. Chen. 1998. Small espin: a third actin-bundling protein and potential forked protein ortholog in brush border microvilli. *J Cell Biol*. 143:107-119.

Bear, J.E., T.M. Svitkina, M. Krause, D.A. Schafer, J.J. Loureiro, G.A. Strasser, I.V. Maly, O.Y. Chaga, J.A. Cooper, G.G. Borisy, and F.B. Gertler. 2002. Antagonism between Ena/VASP proteins and actin filament capping regulates fibroblast motility. *Cell*. 109:509-521.

Belyantseva, I.A., E.T. Boger, and T.B. Friedman. 2003. Myosin XVa localizes to the tips of inner ear sensory cell stereocilia and is essential for staircase formation of the hair bundle. *Proc Natl Acad Sci U S A*. 100:13958-13963.

Benesh, A.E., R. Nambiar, R.E. McConnell, S. Mao, D.L. Tabb, and M.J. Tyska. 2010. Differential localization and dynamics of class I myosins in the enterocyte microvillus. *Mol Biol Cell*. 21:970-978.

Berg, J.S., and R.E. Cheney. 2002. Myosin-X is an unconventional myosin that undergoes intrafilopodial motility. *Nat Cell Biol*. 4:246-250.

Berg, J.S., B.H. Derfler, C.M. Pennisi, D.P. Corey, and R.E. Cheney. 2000. Myosin-X, a novel myosin with pleckstrin homology domains, associates with regions of dynamic actin. *J Cell Sci*. 113 Pt 19:3439-3451.

Bird, J.E., Y. Takagi, N. Billington, M.P. Strub, J.R. Sellers, and T.B. Friedman. 2014. Chaperone-enhanced purification of unconventional myosin 15, a molecular

motor specialized for stereocilia protein trafficking. *Proc Natl Acad Sci U S A*. 111:12390-12395.
Boeda, B., A. El-Amraoui, A. Bahloul, R. Goodyear, L. Daviet, S. Blanchard, I. Perfettini, K.R. Fath, S. Shorte, J. Reiners, A. Houdusse, P. Legrain, U. Wolfrum, G. Richardson, and C. Petit. 2002. Myosin VIIa, harmonin and cadherin 23, three Usher I gene products that cooperate to shape the sensory hair cell bundle. *EMBO J*. 21:6689-6699.
Bohil, A.B., B.W. Robertson, and R.E. Cheney. 2006. Myosin-X is a molecular motor that functions in filopodia formation. *Proc Natl Acad Sci U S A*. 103:12411-12416.
Bornschlogl, T., and P. Bassereau. 2013. The sense is in the fingertips: The distal end controls filopodial mechanics and dynamics in response to external stimuli. *Commun Integr Biol*. 6:e27341.
Bornschlogl, T., S. Romero, C.L. Vestergaard, J.F. Joanny, G.T. Van Nhieu, and P. Bassereau. 2013. Filopodial retraction force is generated by cortical actin dynamics and controlled by reversible tethering at the tip. *Proc Natl Acad Sci U S A*. 110:18928-18933.
Bretscher, A., and K. Weber. 1979. Villin: the major microfilament-associated protein of the intestinal microvillus. *Proc Natl Acad Sci U S A*. 76:2321-2325.
Bretscher, A., and K. Weber. 1980. Fimbrin, a new microfilament-associated protein present in microvilli and other cell surface structures. *J Cell Biol*. 86:335-340.
Bunnell, T.M., B.J. Burbach, Y. Shimizu, and J.M. Ervasti. 2011. beta-Actin specifically controls cell growth, migration, and the G-actin pool. *Mol Biol Cell*. 22:4047-4058.
Buss, F., J. Kendrick-Jones, C. Lionne, A.E. Knight, G.P. Cote, and J. Paul Luzio. 1998. The localization of myosin VI at the golgi complex and leading edge of fibroblasts and its phosphorylation and recruitment into membrane ruffles of A431 cells after growth factor stimulation. *J Cell Biol*. 143:1535-1545.
Cabukusta, B., and J. Neefjes. 2018. Mechanisms of lysosomal positioning and movement. *Traffic*. 19:761-769.
Cavalier-Smith, T., and E.E. Chao. 2003. Phylogeny and classification of phylum Cercozoa (Protozoa). *Protist*. 154:341-358.
Chen, Z.Y., T. Hasson, D.S. Zhang, B.J. Schwender, B.H. Derfler, M.S. Mooseker, and D.P. Corey. 2001. Myosin-VIIb, a novel unconventional myosin, is a constituent of microvilli in transporting epithelia. *Genomics*. 72:285-296.
Cheney, R.E., and M.S. Mooseker. 1992. Unconventional myosins. *Curr Opin Cell Biol*. 4:27-35.
Chinowsky, C.R., J.A. Pinette, L.M. Meenderink, K.S. Lau, and M.J. Tyska. 2020. Nonmuscle myosin-2 contractility-dependent actin turnover limits the length of epithelial microvilli. *Mol Biol Cell*. 31:2803-2815.
Cicuta, P., S.L. Keller, and S.L. Veatch. 2007. Diffusion of liquid domains in lipid bilayer membranes. *J Phys Chem B*. 111:3328-3331.
Cobb, M. 2002. Timeline: exorcizing the animal spirits: Jan Swammerdam on nerve function. *Nat Rev Neurosci*. 3:395-400.
Colom, A., E. Derivery, S. Soleimanpour, C. Tomba, M.D. Molin, N. Sakai, M. Gonzalez-Gaitan, S. Matile, and A. Roux. 2018. A fluorescent membrane tension probe. *Nat Chem*. 10:1118-1125.

Condeelis, J. 1993. Life at the leading edge: the formation of cell protrusions. *Annu Rev Cell Biol*. 9:411-444.
Conzelman, K.A., and M.S. Mooseker. 1987. The 110-kD protein-calmodulin complex of the intestinal microvillus is an actin-activated MgATPase. *J Cell Biol*. 105:313-324.
Courtemanche, N. 2018. Mechanisms of formin-mediated actin assembly and dynamics. *Biophys Rev*. 10:1553-1569.
Crawley, S.W., D.A. Shifrin, N.E. Grega-Larson, R.E. McConnell, A.E. Benesh, S. Mao, Y. Zheng, Q.Y. Zheng, K.T. Nam, B.A. Millis, B. Kachar, and M.J. Tyska. 2014. Intestinal brush border assembly driven by protocadherin-based intermicrovillar adhesion. *Cell*. 157:433-446.
Crawley, S.W., M.L. Weck, N.E. Grega-Larson, D.A. Shifrin, Jr., and M.J. Tyska. 2016. ANKS4B Is Essential for Intermicrovillar Adhesion Complex Formation. *Dev Cell*. 36:190-200.
Dai, J., and M.P. Sheetz. 1995. Mechanical properties of neuronal growth cone membranes studied by tether formation with laser optical tweezers. *Biophys J*. 68:988-996.
Das, S., P.J. Lituma, P.E. Castillo, and R.H. Singer. 2023. Maintenance of a short-lived protein required for long-term memory involves cycles of transcription and local translation. *Neuron*. 111:2051-2064 e2056.
Dobramysl, U., I.K. Jarsch, Y. Inoue, H. Shimo, B. Richier, J.R. Gadsby, J. Mason, A. Szalapak, P.S. Ioannou, G.P. Correia, A. Walrant, R. Butler, E. Hannezo, B.D. Simons, and J.L. Gallop. 2021a. Stochastic combinations of actin regulatory proteins are sufficient to drive filopodia formation. *J Cell Biol*. 220.
Dobramysl, U., I.K. Jarsch, Y. Inoue, H. Shimo, B. Richier, J.R. Gadsby, J. Mason, A. Szałapak, P.S. Ioannou, G.P. Correia, A. Walrant, R. Butler, E. Hannezo, B.D. Simons, and J.L. Gallop. 2021b. Stochastic combinations of actin regulatory proteins are sufficient to drive filopodia formation. *J Cell Biol*. 220.
Dominguez, R. 2004. Actin-binding proteins--a unifying hypothesis. *Trends Biochem Sci*. 29:572-578.
Dominguez, R. 2007. A Common Binding Site for Actin-Binding Proteins on the Actin Surface. *In* Actin-Monomer-Binding Proteins. Springer New York, New York, NY. 107-115.
Dose, A.C., S. Ananthanarayanan, J.E. Moore, B. Burnside, and C.M. Yengo. 2007. Kinetic mechanism of human myosin IIIA. *J Biol Chem*. 282:216-231.
Ebrahim, S., M.R. Avenarius, M. Grati, J.F. Krey, A.M. Windsor, A.D. Sousa, A. Ballesteros, R. Cui, B.A. Millis, F.T. Salles, M.A. Baird, M.W. Davidson, S.M. Jones, D. Choi, L. Dong, M.H. Raval, C.M. Yengo, P.G. Barr-Gillespie, and B. Kachar. 2016. Stereocilia-staircase spacing is influenced by myosin III motors and their cargos espin-1 and espin-like. *Nat Commun*. 7:10833.
El-Mounadi, K., M.L. Morales-Floriano, and H. Garcia-Ruiz. 2020. Principles, Applications, and Biosafety of Plant Genome Editing Using CRISPR-Cas9. *Front Plant Sci*. 11:56.
Ershov, D., M.S. Phan, J.W. Pylvanainen, S.U. Rigaud, L. Le Blanc, A. Charles-Orszag, J.R.W. Conway, R.F. Laine, N.H. Roy, D. Bonazzi, G. Dumenil, G. Jacquemet,

and J.Y. Tinevez. 2022. TrackMate 7: integrating state-of-the-art segmentation algorithms into tracking pipelines. *Nat Methods*. 19:829-832.
Falkenburger, B.H., J.B. Jensen, E.J. Dickson, B.C. Suh, and B. Hille. 2010. Phosphoinositides: lipid regulators of membrane proteins. *J Physiol*. 588:3179-3185.
Feeser, E.A., C.M. Ignacio, M. Krendel, and E.M. Ostap. 2010. Myo1e binds anionic phospholipids with high affinity. *Biochemistry*. 49:9353-9360.
Fierro-Gonzalez, J.C., M.D. White, J.C. Silva, and N. Plachta. 2013. Cadherin-dependent filopodia control preimplantation embryo compaction. *Nat Cell Biol*. 15:1424-1433.
Fitz, G.N., M.L. Weck, C. Bodnya, O.L. Perkins, and M.J. Tyska. 2023. Protrusion growth driven by myosin-generated force. *Dev Cell*. 58:18-33 e16.
Footer, M.J., J.W. Kerssemakers, J.A. Theriot, and M. Dogterom. 2007a. Direct measurement of force generation by actin filament polymerization using an optical trap. *Proc Natl Acad Sci U S A*. 104:2181-2186.
Footer, M.J., J.W.J. Kerssemakers, J.A. Theriot, and M. Dogterom. 2007b. Direct measurement of force generation by actin filament polymerization using an optical trap. *Proc Natl Acad Sci U S A*. 104:2181-2186.
Frixione, E. 2000. Recurring views on the structure and function of the cytoskeleton: a 300-year epic. *Cell Motil Cytoskeleton*. 46:73-94.
Fukuda, M., T. Kojima, H. Kabayama, and K. Mikoshiba. 1996. Mutation of the pleckstrin homology domain of Bruton's tyrosine kinase in immunodeficiency impaired inositol 1,3,4,5-tetrakisphosphate binding capacity. *J Biol Chem*. 271:30303-30306.
Funk, J., F. Merino, L. Venkova, L. Heydenreich, J. Kierfeld, P. Vargas, S. Raunser, M. Piel, and P. Bieling. 2019. Profilin and formin constitute a pacemaker system for robust actin filament growth. *eLife*. 8:e50963.
Galen. 1968. Galen on the usefulness of the parts of the body. De usu partium. M.T. May, editor, Ithaca, N. Y., Cornell University Press.
Gillooly, D.J., C. Raiborg, and H. Stenmark. 2003. Phosphatidylinositol 3-phosphate is found in microdomains of early endosomes. *Histochem Cell Biol*. 120:445-453.
Gong, R., F. Jiang, Z.G. Moreland, M.J. Reynolds, S.E. de Los Reyes, P. Gurel, A. Shams, J.B. Heidings, M.R. Bowl, J.E. Bird, and G.M. Alushin. 2022. Structural basis for tunable control of actin dynamics by myosin-15 in mechanosensory stereocilia. *Sci Adv*. 8:eabl4733.
Goulden, B.D., J. Pacheco, A. Dull, J.P. Zewe, A. Deiters, and G.R.V. Hammond. 2019. A high-avidity biosensor reveals plasma membrane PI(3,4)P(2) is predominantly a class I PI3K signaling product. *J Cell Biol*. 218:1066-1079.
Grati, M., and B. Kachar. 2011. Myosin VIIa and sans localization at stereocilia upper tip-link density implicates these Usher syndrome proteins in mechanotransduction. *Proc Natl Acad Sci U S A*. 108:11476-11481.
Grzybowski, A., and K. Pietrzak. 2013. Robert Remak (1815-1865). *J Neurol*. 260:1696-1697.
Guilford, W.H., D.E. Dupuis, G. Kennedy, J. Wu, J.B. Patlak, and D.M. Warshaw. 1997. Smooth muscle and skeletal muscle myosins produce similar unitary forces and displacements in the laser trap. *Biophys J*. 72:1006-1021.

Hartman, M.A., and J.A. Spudich. 2012. The myosin superfamily at a glance. *J Cell Sci*. 125:1627-1632.
Hasson, T., M.B. Heintzelman, J. Santos-Sacchi, D.P. Corey, and M.S. Mooseker. 1995. Expression in cochlea and retina of myosin VIIa, the gene product defective in Usher syndrome type 1B. *Proc Natl Acad Sci U S A*. 92:9815-9819.
Higashida, C., T. Miyoshi, A. Fujita, F. Oceguera-Yanez, J. Monypenny, Y. Andou, S. Narumiya, and N. Watanabe. 2004. Actin Polymerization-Driven Molecular Movement of mDia1 in Living Cells. *Science*. 303:2007 LP-2010.
Hill, T.L., and M.W. Kirschner. 1982a. Bioenergetics and kinetics of microtubule and actin filament assembly-disassembly. *Int Rev Cytol*. 78:1-125.
Hill, T.L., and M.W. Kirschner. 1982b. Subunit treadmilling of microtubules or actin in the presence of cellular barriers: possible conversion of chemical free energy into mechanical work. *Proc Natl Acad Sci U S A*. 79:490-494.
Hink, M.A., R.A. Griep, J.W. Borst, A. van Hoek, M.H. Eppink, A. Schots, and A.J. Visser. 2000. Structural dynamics of green fluorescent protein alone and fused with a single chain Fv protein. *J Biol Chem*. 275:17556-17560.
Hirano, M., R. Ando, S. Shimozono, M. Sugiyama, N. Takeda, H. Kurokawa, R. Deguchi, K. Endo, K. Haga, R. Takai-Todaka, S. Inaura, Y. Matsumura, H. Hama, Y. Okada, T. Fujiwara, T. Morimoto, K. Katayama, and A. Miyawaki. 2022. A highly photostable and bright green fluorescent protein. *Nat Biotechnol*. 40:1132-1142.
Hirokawa, N., and J.E. Heuser. 1981. Quick-freeze, deep-etch visualization of the cytoskeleton beneath surface differentiations of intestinal epithelial cells. *J Cell Biol*. 91:399-409.
Hirokawa, N., L.G. Tilney, K. Fujiwara, and J.E. Heuser. 1982. Organization of actin, myosin, and intermediate filaments in the brush border of intestinal epithelial cells. *J Cell Biol*. 94:425-443.
Hissa, B., P.W. Oakes, B. Pontes, G. Ramirez-San Juan, and M.L. Gardel. 2017. Cholesterol depletion impairs contractile machinery in neonatal rat cardiomyocytes. *Sci Rep*. 7:43764.
Hokanson, D.E., and E.M. Ostap. 2006. Myo1c binds tightly and specifically to phosphatidylinositol 4,5-bisphosphate and inositol 1,4,5-trisphosphate. *Proc Natl Acad Sci U S A*. 103:3118-3123.
Homma, K., and M. Ikebe. 2005. Myosin X is a high duty ratio motor. *J Biol Chem*. 280:29381-29391.
Homma, K., J. Saito, R. Ikebe, and M. Ikebe. 2001. Motor function and regulation of myosin X. *J Biol Chem*. 276:34348-34354.
Hooke, R. 1665. Micrographia, or, Some physiological descriptions of minute bodies made by magnifying glasses with observations and inquiries thereupon. Printed by J. Martyn and J. Allestry, London. 246 p., 238 leaves of plates (some folded) pp.
Houdusse, A., V.N. Kalabokis, D. Himmel, A.G. Szent-Gyorgyi, and C. Cohen. 1999. Atomic structure of scallop myosin subfragment S1 complexed with MgADP: a novel conformation of the myosin head. *Cell*. 97:459-470.
Houdusse, A., and H.L. Sweeney. 2016. How Myosin Generates Force on Actin Filaments. *Trends Biochem Sci*. 41:989-997.

Houdusse, A., and M.A. Titus. 2021. The many roles of myosins in filopodia, microvilli and stereocilia. *Curr Biol*. 31:R586-R602.
Hurst, J.W., W.B. Fye, and W.B. Fye. 2002. Giorgio Baglivi. *Clinical Cardiology*. 25:487-489.
Huxley, A.F. 1957. Muscle structure and theories of contraction. *Prog Biophys Biophys Chem*. 7:255-318.
Inobe, T., and N. Nukina. 2016. Rapamycin-induced oligomer formation system of FRB-FKBP fusion proteins. *J Biosc Bioeng*. 122:40-46.
Jacquemet, G., A. Stubb, R. Saup, M. Miihkinen, E. Kremneva, H. Hamidi, and J. Ivaska. 2019. Filopodome Mapping Identifies p130Cas as a Mechanosensitive Regulator of Filopodia Stability. *Curr Biol*. 29:202-216 e207.
Kardel, T. 1990. Niels Stensen's geometrical theory of muscle contraction (1667): a reappraisal. *J Biomech*. 23:953-965.
Kerber, M.L., and R.E. Cheney. 2011. Myosin-X: a MyTH-FERM myosin at the tips of filopodia. *J Cell Sci*. 124:3733-3741.
Kodera, N., and T. Ando. 2014. The path to visualization of walking myosin V by high-speed atomic force microscopy. *Biophysical Reviews*. 6.
Koltzoff, N. 1905. Studien über die Gestalt der Zelle: I. Untersuchungen über die Spermien der Decapoden, als Einleitung in das Problem der Zellengestalt. *Archiv für mikrosckopische Anatomie*. 67:364-571.
Koltzoff, N. 1924. Experimental Biology and the Work of the Moscow Institute. *Science*. 59:497-502.
Komaba, S., A. Inoue, S. Maruta, H. Hosoya, and M. Ikebe. 2003. Determination of human myosin III as a motor protein having a protein kinase activity. *J Biol Chem*. 278:21352-21360.
Korn, E.D., M.F. Carlier, and D. Pantaloni. 1987. Actin polymerization and ATP hydrolysis. *Science*. 238:638-644.
Kovar, D.R., and T.D. Pollard. 2004a. Insertional assembly of actin filament barbed ends in association with formins produces piconewton forces. *Proc Natl Acad Sci U S A*. 101:14725-14730.
Kovar, D.R., and T.D. Pollard. 2004b. Insertional assembly of actin filament barbed ends in association with formins produces piconewton forces. *Proc Natl Acad Sci U S A*. 101:14725 LP-14730.
Krause, W. 1869. Die motorischen Endplatten der quergestreiften Muskelfasern. Hahn.
Krey, J.F., E.S. Krystofiak, R.A. Dumont, S. Vijayakumar, D. Choi, F. Rivero, B. Kachar, S.M. Jones, and P.G. Barr-Gillespie. 2016. Plastin 1 widens stereocilia by transforming actin filament packing from hexagonal to liquid. *J Cell Biol*. 215:467-482.
Krey, J.F., P.A. Wilmarth, L.L. David, and P.G. Barr-Gillespie. 2017. Analysis of the Proteome of Hair-Cell Stereocilia by Mass Spectrometry. *Methods Enzymol*. 585:329-354.
Kühne, W. 1864. Untersuchungen über das Protoplasma und die Contractilität. W. Engelmann.
Leeuwenhoek, A.v. 1674. More microscopical observations made by the same M. Leewenhoeck, and promised in numb. 97. Of these tracts; communicated in his

letters of August 15. 1673 and of April 7. 1674. *Philosophical Transactions of the Royal Society of London*. 9:23-25.
Leijnse, N., Y.F. Barooji, M.R. Arastoo, S.L. Sonder, B. Verhagen, L. Wullkopf, J.T. Erler, S. Semsey, J. Nylandsted, L.B. Oddershede, A. Doostmohammadi, and P.M. Bendix. 2022. Filopodia rotate and coil by actively generating twist in their actin shaft. *Nat Commun*. 13:1636.
Li, J., Y. He, M.L. Weck, Q. Lu, M.J. Tyska, and M. Zhang. 2017. Structure of Myo7b/USH1C complex suggests a general PDZ domain binding mode by MyTH4-FERM myosins. *Proc Natl Acad Sci U S A*. 114:E3776-E3785.
Lohmann, K. 1929. Über die Pyrophosphatfraktion im Muskel. *Naturwissenschaften*. 17:624-625.
Lohmann, K. 1934. Über die enzymatische Aufspaltung der Kreatinphosphorsäure; zugleich ein Beitrag zum Chemismus der Muskelkontraktion. *Biochem. z*. 271:264-277.
Lord, S.J., K.B. Velle, R.D. Mullins, and L.K. Fritz-Laylin. 2020. SuperPlots: Communicating reproducibility and variability in cell biology. *J Cell Biol*. 219.
Lymn, R.W., and E.W. Taylor. 1971. Mechanism of adenosine triphosphate hydrolysis by actomyosin. *Biochemistry*. 10:4617-4624.
Mahammad, S., and I. Parmryd. 2015. Cholesterol depletion using methyl-beta-cyclodextrin. *Methods Mol Biol*. 1232:91-102.
Manor, U., A. Disanza, M. Grati, L. Andrade, H. Lin, P.P. Di Fiore, G. Scita, and B. Kachar. 2011. Regulation of stereocilia length by myosin XVa and whirlin depends on the actin-regulatory protein Eps8. *Curr Biol*. 21:167-172.
Mattila, P.K., and P. Lappalainen. 2008. Filopodia: molecular architecture and cellular functions. *Nat Rev Mol Cell Biol*. 9:446-454.
Mazerik, J.N., and M.J. Tyska. 2012. Myosin-1A targets to microvilli using multiple membrane binding motifs in the tail homology 1 (TH1) domain. *J Biol Chem*. 287:13104-13115.
McConnell, R.E., A.E. Benesh, S. Mao, D.L. Tabb, and M.J. Tyska. 2011. Proteomic analysis of the enterocyte brush border. *Am J Physiol - GLP*. 300:6914-6926.
Medalia, O., M. Beck, M. Ecke, I. Weber, R. Neujahr, W. Baumeister, and G. Gerisch. 2007. Organization of actin networks in intact filopodia. *Curr Biol*. 17:79-84.
Medeiros, N.A., D.T. Burnette, and P. Forscher. 2006. Myosin II functions in actin-bundle turnover in neuronal growth cones. *Nat Cell Biol*. 8:215-226.
Millard, T.H., and P. Martin. 2008. Dynamic analysis of filopodial interactions during the zippering phase of Drosophila dorsal closure. *Development*. 135:621-626.
Mogilner, A., and G. Oster. 1996a. Cell motility driven by actin polymerization. *Biophysical Journal*. 71:3030-3045.
Mogilner, A., and G. Oster. 1996b. Cell motility driven by actin polymerization. *Biophys J*. 71:3030-3045.
Mogilner, A., and B. Rubinstein. 2005. The physics of filopodial protrusion. *Biophys J*. 89:782-795.
Mooseker, M.S., and L.G. Tilney. 1975. Organization of an actin filament-membrane complex: Filament polarity and membrane attachment in the microvilli of intestinal epithelial cells. *J Cell Biol*. 67:725-743.

Morales, E.A., C. Arnaiz, E.S. Krystofiak, M. Zanic, and M.J. Tyska. 2022. Mitotic Spindle Positioning (MISP) is an actin bundler that selectively stabilizes the rootlets of epithelial microvilli. *Cell Rep*. 39:110692.
Moreland, Z.G., F. Jiang, C. Aguilar, M. Barzik, R. Gong, A. Shams, C. Faaborg-Andersen, J.C. Werth, R. Harley, D.C. Sutton, S.M. Cole, A. Parker, S. Morse, E. Wilson, Y. Takagi, J.R. Sellers, S.D.M. Brown, T.B. Friedman, G.M. Alushin, M.R. Bowl, and J.E. Bird. 2021. Myosin-driven Nucleation of Actin Filaments Drives Stereocilia Development Critical for Hearing. *bioRxiv*:2021.2007.2009.451618.
Mountford, P.S., and A.G. Smith. 1995. Internal ribosome entry sites and dicistronic RNAs in mammalian transgenesis. *Trends Genet*. 11:179-184.
Mullins, R.D., J.A. Heuser, and T.D. Pollard. 1998. The interaction of Arp2/3 complex with actin: nucleation, high affinity pointed end capping, and formation of branching networks of filaments. *Proc Natl Acad Sci U S A*. 95:6181-6186.
Nagy, S., B.L. Ricca, M.F. Norstrom, D.S. Courson, C.M. Brawley, P.A. Smithback, and R.S. Rock. 2008. A myosin motor that selects bundled actin for motility. *Proc Natl Acad Sci U S A*. 105:9616-9620.
O'Connell, C.B., M.J. Tyska, and M.S. Mooseker. 2007. Myosin at work: Motor adaptations for a variety of cellular functions. *Biochim Biophys Acta*. 11773:615-630.
Orly, G., M. Naoz, and N.S. Gov. 2014. Physical model for the geometry of actin-based cellular protrusions. *Biophys J*. 107:576-587.
Peremyslov, V.V., A.L. Klocko, J.E. Fowler, and V.V. Dolja. 2012. Arabidopsis Myosin XI-K Localizes to the Motile Endomembrane Vesicles Associated with F-actin. *Front Plant Sci*. 3:184.
Perrin, B.J., D.M. Strandjord, P. Narayanan, D.M. Henderson, K.R. Johnson, and J.M. Ervasti. 2013. beta-Actin and fascin-2 cooperate to maintain stereocilia length. *J Neurosci*. 33:8114-8121.
Peskin, C.S., G.M. Odell, and G.F. Oster. 1993. Cellular motions and thermal fluctuations: the Brownian ratchet. *Biophys J*. 65:316-324.
Petersen, K.J., H.V. Goodson, A.L. Arthur, G.W. Luxton, A. Houdusse, and M.A. Titus. 2016. MyTH4-FERM myosins have an ancient and conserved role in filopod formation. *Proc Natl Acad Sci U S A*. 113:E8059-E8068.
Pinaud, F., S. Clarke, A. Sittner, and M. Dahan. 2010. Probing cellular events, one quantum dot at a time. *Nat Methods*. 7:275-285.
Plantard, L., A. Arjonen, J.G. Lock, G. Nurani, J. Ivaska, and S. Strömblad. 2010. PtdIns(3,4,5)P3 is a regulator of myosin-X localization and filopodia formation. *J Cell Sci*. 123:3524-3534.
Pollard, T.D. 1986. Rate constants for the reactions of ATP- and ADP-actin with the ends of actin filaments. *J Cell Biol*. 103:2747-2754.
Pollard, T.D. 2016. Actin and Actin-Binding Proteins. *Cold Spring Harb Perspect Biol*. 8.
Pollard, T.D., and G.G. Borisy. 2003. Cellular motility driven by assembly and disassembly of actin filaments. *Cell*. 112:453-465.
Pollard, T.D., and J.A. Cooper. 1986. ACTIN AND ACTIN-BINDING PROTEINS. A CRITICAL EVALUATION OF MECHANISMS AND FUNCTIONS. *Annual Review of Biochemistry*. 55:987-1035.

Portera-Cailliau, C., D.T. Pan, and R. Yuste. 2003. Activity-regulated dynamic behavior of early dendritic protrusions: evidence for different types of dendritic filopodia. *J Neurosci*. 23:7129-7142.
Prokhnevsky, A.I., V.V. Peremyslov, and V.V. Dolja. 2008. Overlapping functions of the four class XI myosins in Arabidopsis growth, root hair elongation, and organelle motility. *Proc Natl Acad Sci U S A*. 105:19744-19749.
Prost, J., C. Barbetta, and J.F. Joanny. 2007. Dynamical control of the shape and size of stereocilia and microvilli. *Biophys J*. 93:1124-1133.
Purcell, T.J., C. Morris, J.A. Spudich, and H.L. Sweeney. 2002. Role of the lever arm in the processive stepping of myosin V. *Proc Natl Acad Sci U S A*. 99:14159-14164.
Quintero, O.A., M.M. DiVito, R.C. Adikes, M.B. Kortan, L.B. Case, A.J. Lier, N.S. Panaretos, S.Q. Slater, M. Rengarajan, M. Feliu, and R.E. Cheney. 2009. Human Myo19 is a novel myosin that associates with mitochondria. *Curr Biol*. 19:2008-2013.
Raposo, G., M.N. Cordonnier, D. Tenza, B. Menichi, A. Durrbach, D. Louvard, and E. Coudrier. 1999. Association of myosin I alpha with endosomes and lysosomes in mammalian cells. *Mol Biol Cell*. 10:1477-1494.
Raucher, D., and M.P. Sheetz. 1999a. Characteristics of a membrane reservoir buffering membrane tension. *Biophys J*. 77:1992-2002.
Raucher, D., and M.P. Sheetz. 1999b. Membrane expansion increases endocytosis rate during mitosis. *J Cell Biol*. 144:497-506.
Raucher, D., and M.P. Sheetz. 2000a. Cell spreading and lamellipodial extension rate is regulated by membrane tension. *Journal of Cell Biology*. 148.
Raucher, D., and M.P. Sheetz. 2000b. Cell spreading and lamellipodial extension rate is regulated by membrane tension. *J Cell Biol*. 148:127-136.
Rayment, I., W.R. Rypniewski, K. Schmidt-Bäse, R. Smith, D.R. Tomchick, M.M. Benning, D.A. Winkelmann, G. Wesenberg, and H.M. Holden. 1993. Three-dimensional structure of myosin subfragment-1: A molecular motor. *Science*. 261:50-58.
Remak, R. 1844. Neurologische Erläuterungen. *Arch Anat Physiol wiss Med*. 12:463-472.
Renshaw, H., J.M. Vargas-Muniz, A.D. Richards, Y.G. Asfaw, P.R. Juvvadi, and W.J. Steinbach. 2016. Distinct Roles of Myosins in Aspergillus fumigatus Hyphal Growth and Pathogenesis. *Infect Immun*. 84:1556-1564.
Revenu, C., R. Athman, S. Robine, and D. Louvard. 2004. The co-workers of actin filaments: from cell structures to signals. *Nat Rev Mol Cell Biol*. 5:635-646.
Reynolds, M.J., C. Hachicho, A.G. Carl, R. Gong, and G.M. Alushin. 2022. Bending forces and nucleotide state jointly regulate F-actin structure. *Nature*. 611:380-386.
Ricca, B.L., and R.S. Rock. 2010. The stepping pattern of myosin X is adapted for processive motility on bundled actin. *Biophys J*. 99:1818-1826.
Robert-Paganin, J., O. Pylypenko, C. Kikuti, H.L. Sweeney, and A. Houdusse. 2020. Force Generation by Myosin Motors: A Structural Perspective. *Chem Rev*. 120:5-35.

Rogers, M.S., and E.E. Strehler. 2001. The tumor-sensitive calmodulin-like protein is a specific light chain of human unconventional myosin X. *J Biol Chem*. 276:12182-12189.
Ropars, V., Z. Yang, T. Isabet, F. Blanc, K. Zhou, T. Lin, X. Liu, P. Hissier, F. Samazan, B. Amigues, E.D. Yang, H. Park, O. Pylypenko, M. Cecchini, C.V. Sindelar, H.L. Sweeney, and A. Houdusse. 2016. The myosin X motor is optimized for movement on actin bundles. *Nat Commun*. 7:12456.
Sakamoto, T., A. Yildez, P.R. Selvin, and J.R. Sellers. 2005. Step-size is determined by neck length in myosin V. *Biochemistry*. 44:16203-16210.
Salim, K., M.J. Bottomley, E. Querfurth, M.J. Zvelebil, I. Gout, R. Scaife, R.L. Margolis, R. Gigg, C.I. Smith, P.C. Driscoll, M.D. Waterfield, and G. Panayotou. 1996. Distinct specificity in the recognition of phosphoinositides by the pleckstrin homology domains of dynamin and Bruton's tyrosine kinase. *EMBO J*. 15:6241-6250.
Sanderson, J.M. 2012. Resolving the kinetics of lipid, protein and peptide diffusion in membranes. *Mol Membr Biol*. 29:118-143.
Sasaki, N., and K. Sutoh. 1998. Structure-mutation analysis of the ATPase site of Dictyostelium discoideum myosin II. *Adv Biophys*. 35:1-24.
Schäfer, C., U. Faust, N. Kirchgeßner, R. Merkel, and B. Hoffmann. 2011. The filopodium. *Cell Adh Migr*. 5:431-438.
Schneider, M.E., A.C. Dosé, F.T. Salles, W. Chang, F.L. Erickson, B. Burnside, and B. Kachar. 2006. A new compartment at stereocilia tips defined by spatial and temporal patterns of myosin IIIa expression. *J Neurosci*. 26:10243-10252.
Sebe-Pedros, A., P. Burkhardt, N. Sanchez-Pons, S.R. Fairclough, B.F. Lang, N. King, and I. Ruiz-Trillo. 2013. Insights into the origin of metazoan filopodia and microvilli. *Mol Biol Evol*. 30:2013-2023.
Sebe-Pedros, A., X. Grau-Bove, T.A. Richards, and I. Ruiz-Trillo. 2014. Evolution and classification of myosins, a paneukaryotic whole-genome approach. *Genome Biol Evol*. 6:290-305.
Sekerkova, G., L. Zheng, E. Mugnaini, and J.R. Bartles. 2006. Differential expression of espin isoforms during epithelial morphogenesis, stereociliogenesis and postnatal maturation in the developing inner ear. *Dev Biol*. 291:83-95.
Sekino, Y., N. Kojima, and T. Shirao. 2007. Role of actin cytoskeleton in dendritic spine morphogenesis. *Neurochem Int*. 51:92-104.
Sellers, J.R. 2000. Myosins: A diverse superfamily. *Biochim Biophys Acta*. 1496:3-22.
Shangguan, J., and R.S. Rock. 2023. Pushed to the edge: hundreds of Myosin 10s pack into filopodia and could cause traffic jams on actin. eLife Sciences Publications, Ltd.
Sheetz, M.P. 2001. Cell control by membrane-cytoskeleton adhesion. *Nat Rev Mol Cell Biol*. 2:392-396.
Sheetz, M.P., D.B. Wayne, and A.L. Pearlman. 1992. Extension of filopodia by motor-dependent actin assembly. *Cell Motil Cytoskeleton*. 22:160-169.
Shi, Z., Z.T. Graber, T. Baumgart, H.A. Stone, and A.E. Cohen. 2018. Cell Membranes Resist Flow. *Cell*. 175:1769-1779 e1713.
Small, J.V. 1988. The actin cytoskeleton. *Electron Microsc Rev*. 1:155-174.

Smoluchowski, M. 1927. Experimentell nachweisbare, der üblichen Thermodynamik widersprechende Molekularphänomene. *Pisma Mariana Smoluchowskiego*. 2.
Sousa, A.D., and R.E. Cheney. 2005. Myosin-X: a molecular motor at the cell's fingertips. *Trends Cell Biol*. 15:533-539.
Spector, I., N.R. Shochet, Y. Kashman, and A. Groweiss. 1983. Latrunculins: novel marine toxins that disrupt microfilament organization in cultured cells. *Science*. 219:493-495.
Squire, J.M. 2016. Muscle contraction: Sliding filament history, sarcomere dynamics and the two Huxleys. *Glob Cardiol Sci Pract*. 2016:e201611.
Stensen, N. 1667. Nicolai Stenonis Elementorum myologiæ specimen: seu Musculi descriptio geometrica. Cui accedunt Canis carchariæ dissectum caput, et Dissectus piscis ex canum genere. Ex typographia sub signo stellæ.
Sun, Y., and Y.E. Goldman. 2011. Lever-arm mechanics of processive myosins. *Biophys J*. 101:1-11.
Svitkina, T.M., E.A. Bulanova, O.Y. Chaga, D.M. Vignjevic, S. Kojima, J.M. Vasiliev, and G.G. Borisy. 2003. Mechanism of filopodia initiation by reorganization of a dendritic network. *J Cell Biol*. 160:409-421.
Svitkina, T.M., A.B. Verkhovsky, K.M. McQuade, and G.G. Borisy. 1997. Analysis of the actin-myosin II system in fish epidermal keratocytes: mechanism of cell body translocation. *J Cell Biol*. 139:397-415.
Swammerdam, J. 1679. Tractatus physico-anatomico-medicus de respiratione usuque pulmonum. Apud Joannem vander Linden.
Swammerdam, J. 1758. The Book of Nature II. *London (UK): Seyffert*:122-132.
Szent-Györgyi, A. 1942. Studies from the Institute of Medical Chemistry, University Szeged: vol. 2. S. Karger.
Szent-Györgyi, A. 1944. Studies on muscle. University of Szeged. Institute of Medical Chemistry.
Szent-Gyorgyi, A.G. 2004. The early history of the biochemistry of muscle contraction. *J Gen Physiol*. 123:631-641.
Takagi, Y., R.E. Farrow, N. Billington, A. Nagy, C. Batters, Y. Yang, J.R. Sellers, and J.E. Molloy. 2014. Myosin-10 produces its power-stroke in two phases and moves processively along a single actin filament under low load. *Proc Natl Acad Sci U S A*. 111:E1833-1842.
Tanenbaum, M.E., L.A. Gilbert, L.S. Qi, J.S. Weissman, and R.D. Vale. 2014. A protein-tagging system for signal amplification in gene expression and fluorescence imaging. *Cell*. 159:635-646.
Theriot, J.A. 2000. The polymerization motor. *Traffic*. 1:19-28.
Tilney, L.G., D.J. Derosier, and M.J. Mulroy. 1980. The organization of actin filaments in the stereocilia of cochlear hair cells. *J Cell Biol*. 86:244-259.
Tinevez, J.Y., N. Perry, J. Schindelin, G.M. Hoopes, G.D. Reynolds, E. Laplantine, S.Y. Bednarek, S.L. Shorte, and K.W. Eliceiri. 2017. TrackMate: An open and extensible platform for single-particle tracking. *Methods*. 115:80-90.
Titus, M.A. 2018. Myosin-Driven Intracellular Transport. *Cold Spring Harb Perspect Biol*. 10.
Tokuo, H., and M. Ikebe. 2004a. Myosin X transports Mena/VASP to the tip of filopodia. *Biochem and Biophys Res Comm*. 319:214-220.

Tokuo, H., and M. Ikebe. 2004b. Myosin X transports Mena/VASP to the tip of filopodia. *Biochem Biophys Res Commun*. 319:214-220.
Tsirkas, I., T. Zur, D. Dovrat, A. Cohen, L. Ravkaie, and A. Aharoni. 2022. Protein fluorescent labeling in live yeast cells using scFv-based probes. *Cell Rep Methods*. 2:100357.
Tyska, M.J., D.E. Dupuis, W.H. Guilford, J.B. Patlak, G.S. Waller, K.M. Trybus, D.M. Warshaw, and S. Lowey. 1999. Two heads of myosin are better than one for generating force and motion. *Proc Natl Acad Sci U S A*. 96:4402-4407.
Tyska, M.J., and M.S. Mooseker. 2002. MYO1A (brush border myosin I) dynamics in the brush border of LLC-PK1-CL4 cells. *Biophys J*. 82:1869-1883.
Uhlen, M., L. Fagerberg, B.M. Hallstrom, C. Lindskog, P. Oksvold, A. Mardinoglu, A. Sivertsson, C. Kampf, E. Sjostedt, A. Asplund, I. Olsson, K. Edlund, E. Lundberg, S. Navani, C.A. Szigyarto, J. Odeberg, D. Djureinovic, J.O. Takanen, S. Hober, T. Alm, P.H. Edqvist, H. Berling, H. Tegel, J. Mulder, J. Rockberg, P. Nilsson, J.M. Schwenk, M. Hamsten, K. von Feilitzen, M. Forsberg, L. Persson, F. Johansson, M. Zwahlen, G. von Heijne, J. Nielsen, and F. Ponten. 2015. Proteomics. Tissue-based map of the human proteome. *Science*. 347:1260419.
Uyeda, T.Q.P., P.D. Abramson, and J.A. Spudich. 1996. The neck region of the myosin motor domain acts as a lever arm to generate movement. *Proc Natl Acad Sci USA*. 93:4459-4464.
VanBuren, P., W.H. Guilford, G. Kennedy, J. Wu, and D.M. Warshaw. 1995. Smooth muscle myosin: a high force-generating molecular motor. *Biophys J*. 68:256S-258S; 258S-259S.
VanBuren, P., S.S. Work, and D.M. Warshaw. 1994. Enhanced force generation by smooth muscle myosin in vitro. *Proc Natl Acad Sci U S A*. 91:202-205.
Vandekerckhove, J., A. Deboben, M. Nassal, and T. Wieland. 1985. The phalloidin binding site of F-actin. *EMBO J*. 4:2815-2818.
Vignjevic, D., S. Kojima, Y. Aratyn, O. Danciu, T. Svitkina, and G.G. Borisy. 2006a. Role of fascin in filopodial protrusion. *J Cell Biol*. 174:863-875.
Vignjevic, D., S.I. Kojima, Y. Aratyn, O. Danciu, T. Svitkina, and G.G. Borisy. 2006b. Role of fascin in filopodial protrusion. *J Cell Biol*.
Vignjevic, D., M. Schoumacher, N. Gavert, K.P. Janssen, G. Jih, M. Lae, D. Louvard, A. Ben-Ze'ev, and S. Robine. 2007. Fascin, a novel target of beta-catenin-TCF signaling, is expressed at the invasive front of human colon cancer. *Cancer Res*. 67:6844-6853.
von Brücke, E.W. 1858. Untersuchungen über den Bau der Muskelfasern mit Hülfe des polarisirten Lichtes. Kaiserl.-königl. Hof- und Staatsdr.
von Haller, A. 1732. De partibus corporis humani sensilibus et irritabilibus.
Warshaw, D.M., W.H. Guilford, Y. Freyzon, E. Krementsova, K.A. Palmiter, M.J. Tyska, J.E. Baker, and K.M. Trybus. 2000. The light chain binding domain of expressed smooth muscle heavy meromyosin acts as a mechanical lever. *J Biol Chem*. 275:37167-37172.
Weck, M.L., S.W. Crawley, C.R. Stone, and M.J. Tyska. 2016. Myosin-7b Promotes Distal Tip Localization of the Intermicrovillar Adhesion Complex. *Curr Biol*. 26:2717-2728.

Wintrebert, P. 1931. La rotation immédiate de l'oeuf pondu et la rotation d'activation chez Discoglossus pictus Otth. *CR Soc. Biol*. 106:439-442.
Wood, W., A. Jacinto, R. Grose, S. Woolner, J. Gale, C. Wilson, and P. Martin. 2002. Wound healing recapitulates morphogenesis in Drosophila embryos. *Nat Cell Biol*. 4:907-912.
Woodrum, D.T., S.A. Rich, and T.D. Pollard. 1975. Evidence for biased bidirectional polymerization of actin filaments using heavy meromyosin prepared by an improved method. *J Cell Biol*. 67:231-237.
Woolner, S., and W.M. Bement. 2009. Unconventional myosins acting unconventionally. *Trends Cell Biol*. 19:245-252.
Wright, L.P., and M.R. Philips. 2006. Thematic review series: lipid posttranslational modifications. CAAX modification and membrane targeting of Ras. *J Lipid Res*. 47:883-891.
Yang, C., and T. Svitkina. 2011. Filopodia initiation: focus on the Arp2/3 complex and formins. *Cell Adh Migr*. 5:402-408.
Yu, I.M., V.J. Planelles-Herrero, Y. Sourigues, D. Moussaoui, H. Sirkia, C. Kikuti, D. Stroebel, M.A. Titus, and A. Houdusse. 2017. Myosin 7 and its adaptors link cadherins to actin. *Nat Commun*. 8:15864.
Yu, Y., M. Li, and Y. Yu. 2019. Tracking Single Molecules in Biomembranes: Is Seeing Always Believing? *ACS Nano*. 13:10860-10868.
Zhang, H., J.S. Berg, Z. Li, Y. Wang, P. Lang, A.D. Sousa, A. Bhaskar, R.E. Cheney, and S. Stromblad. 2004a. Myosin-X provides a motor-based link between integrins and the cytoskeleton. *Nat Cell Biol*. 6:523-531.
Zhang, H., J.S. Berg, Y. Wang, P. Lång, A.D. Sousa, A. Bhaskar, R.E. Cheney, and S. Strömblad. 2004b. Myosin-X provides a motor-based link between integrins and the cytoskeleton. *Nat Cell Biol*. 6:523-531.
Zhang, Z., N. Denans, Y. Liu, O. Zhulyn, H.D. Rosenblatt, M. Wernig, and M. Barna. 2021. Optogenetic manipulation of cellular communication using engineered myosin motors. *Nat Cell Biol*. 23:198-208.
Zheng, L., J. Zheng, D.S. Whitlon, J. Garcia-Anoveros, and J.R. Bartles. 2010. Targeting of the hair cell proteins cadherin 23, harmonin, myosin XVa, espin, and prestin in an epithelial cell model. *J Neurosci*. 30:7187-7201.